9-10-2010

Collisional Dynamics of the Cesium D1 and D2 Transitions

Greg A. Pitz

**Collisional Dynamics
of the
Cesium D_1 and D_2 Transitions**

DISSERTATION

Greg Anthony Pitz, Civilian

AFIT/DS/ENP/10-S05

**DEPARTMENT OF THE AIR FORCE
AIR UNIVERSITY**

AIR FORCE INSTITUTE OF TECHNOLOGY

Wright-Patterson Air Force Base, Ohio

APPROVED FOR PUBLIC RELEASE; DISTRIBUTION UNLIMITED

The views expressed in this document are those of the author and do not reflect the official policy or position of the United States Air Force, the United States Department of Defense or the United States Government.

COLLISIONAL DYNAMICS OF THE CESIUM D_1 AND D_2 TRANSITIONS

DISSERTATION

Presented to the Faculty

Graduate School of Engineering and Management

Air Force Institute of Technology

Air University

Air Education and Training Command

in Partial Fulfillment of the Requirements for the

Degree of Doctor of Philosophy

Greg Anthony Pitz, BA, MS

Civilian

September 2010

APPROVED FOR PUBLIC RELEASE; DISTRIBUTION UNLIMITED

AFIT/DS/ENP/10-S05

COLLISIONAL DYNAMICS OF THE CESIUM D_1 AND D_2 TRANSITIONS

Greg Anthony Pitz, BA, MS
Civilian

Approved:

_____

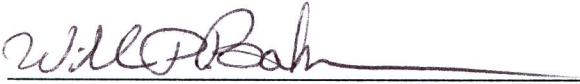Glen P. Perram, PhD (Chairman)

9 Sep 10

Date

_____

David E. Weeks, PhD (Member)

9 Sep 10

Date

_____
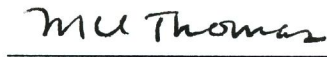
William P. Baker, PhD (Member)

18 Sep 2010

Date

Accepted:

_____

M. U. Thomas
Dean, Graduate School of Engineering
  and Management

14 Sep 2010

Date

Abstract

The collisional dynamics of the 6^2P levels in cesium have been studied utilizing steady state laser absorption and laser induced florescence techniques. In addition the production of a blue beam produced by two photon absorption has been observed in potassium. The collisional broadening rate for cesium, γ_L, for He, Ne, Ar, Kr, Xe, N_2, H_2, HD, D_2, CH_4, C_2H_6, CF_4, and ^{3}He are 24.13, 10.85, 18.31, 17.82, 19.74, 16.64, 20.81, 20.06, 18.04, 29.00, 26.70, 18.84, and 26.00 MHz/torr, respectively for the $6^2P_{1/2} \to 6^2S_{1/2}$ transition and 20.59, 9.81, 16.47, 15.54, 18.41, 19.18, 27.13, 28.24, 22.84, 25.84, 26.14, 17.81, and 22.35 MHz/torr for the $6^2P_{3/2} \to 6^2S_{1/2}$ transition. The corresponding pressure-induced shift rates, δ, are 4.24, -1.60, -6.47, -5.46, -6.43, -7.76, 1.11, 0.47, 0.00, -9.28, -8.54, -6.06, and 6.01 MHz/torr for the $6^2P_{1/2} \to 6^2S_{1/2}$ transition and 0.69, -2.58, -6.18, -6.09, -6.75, -6.20, -4.83, -4.49, -4.54, -8.86, -9.38, -6.47, and 0.60 MHz/Torr for the $6^2P_{3/2} \to 6^2S_{1/2}$ transition. These values have been compared with the values of other alkalis and the inter-atomic difference potentials have been determined using the impact approximation. The energy exchange rates between the two excited states of cesium by collisions with N_2, H_2, HD, D_2, CH_4, C_2H_6, CF_4, and C_2F_6 have been measured and shown to correlate with both the rotational energy defect and the vibrational energy defect. And finally, while pumping from the ground state 4^2S to the excited 5^2D and 6^2S states of potassium, a blue beam corresponding to the transition $5^2P \to 4^2S$ was observed. The effects of input power and buffer gas pressure where observed.

To My Wife and Children

Acknowledgements

First and foremost, I would like to thank God for giving me the ability to accomplish this work, and for giving me such a patient and understanding wife. I want to thank my wife for taking care of our children and putting up with my long work hours for the past 6 years. I also want to thank her for encouragement and support she gave me when things got tough. Without her I might not be where I am today.

Second, I would like to thank my parents for pushing me to the limits and encouraging me that I could do anything I want to do.

I would like to thank my advisor, Dr. Glen Perram, for giving me the support both financially and emotionally through my efforts and hard work. I will forever be in his debt for the help he gave which was beyond that of an advisor and that of a true mentor.

Additionally, I would also like to thank the DPAL research team, Lt Col. Monte Anderson, Maj. Cliff Sulham, Maj. Grady Phillips, Lt. Doug Thornton, Eric Guild, and Chris Rice whose support and friendship I consider to be priceless.

Finally, I would like to thank the two students, Charles Fox and Doug Wertepny, who worked with me side-by-side in the lab, doing the tedious and mundane tasks that I asked of them.

Greg Anthony Pitz

Table of Contents

List of Figures

List of Tables

COLLISIONAL DYNAMICS OF THE CESIUM D_1 AND D_2 TRANSITIONS

I. Introduction

Interest in Alkali Lasers

Through the ages Alkali atoms have been of interest for numerous reasons. Lithium, in the form of lithium carbonate, can be used to treat depression. Sodium, while in the form of sodium chloride is table salt and sodium nitrate is a primary ingredient in gunpowder. Potassium is used heavily in fertilizer but in the form of potassium chlorate it is used in explosives. Rubidium and cesium are more rare and are commonly used in chemical research. But these two heavier alkalis are also used in atomic clocks for global positioning satellites. In fact, the cesium ground state fine splitting is the frequency and time standard used in the United States.[60]

The lighter alkalis, sodium and potassium, were discovered using electrolysis in 1807. It was not until the mid 19th century, 1861, when cesium and rubidium was discovered. These two alkalis were some of the first elements discovered using spectrum analysis.[30] The spectral profile of sodium was first seen by Fraunhoffer in his studies of the solar spectrum, but not labeled as such until Kirchhoff and Bunsen started to assign spectrum to the elements. It is important to note that because of the designation of the solar absorption lines the transition between the ground state and the first excited state of sodium was called the D-Line, naming the major absorption lines sequentially, A through K. As time passed and technology increased the D-line was resolved into two separate and distinct lines. This revelation introduced subscripts (D_1 and D_2) into their designations. These separate lines still refer to

1

sodium but the fine splitting of the ^2P state has been resolved. These designations have held and now all the transitions between $^2P_{1/2}$ and $^2P_{3/2}$ to the ground state, $^2S_{1/2}$, for the alkali are called the D_1 and D_2 lines, respectively.

These two transitions have become of great interest recently for use in a three level laser system. Beach and Krupke have proposed the use of diodes to pump an alkali along its D_2 transition and utilized spin-orbit energy transfer to a buffer gas to transfer the energy from the $^2P_{3/2}$ state to the $^2P_{1/2}$ state. This will then lase along the D_1 transition. This process is shown in Fig. 1. While the use of alkalis as laser is not a novel concept, the idea of using the lowest transitions is. Schawlow and Townes proposed a potassium-based laser in 1958, but instead of pumping with red light along the D lines to the 4^2P state they suggested pumping with blue light to the 5^2P state. This excited state will naturally decay down to the 3^2D and the 5^2S states in 0.2 μs. From these states the energy can be funneled into the 4^2P state, the upper state of the lasing transition. This process is shown in Fig. 1 for comparison to Beach and Krupke's 3 Level Laser system. In 1962, Rabinowitz used this concept to produce an IR laser. He used a UV source to pump from the 6^2S to the 8^2P of cesium. This immediately created a population inversion between this excited state and the lower states 8^2S and 6^2D, which produced lasing at 7.18 μm. All of these lasers are possible because of the extremely large cross-sections for absorption in the alkalis.

The Diode Pumped Alkali Laser (DPAL) is of high appeal for the United States Air Force. This system has the possibility of providing the power of a chemical laser, without the logistics trail and the infinite magazine depth. It also provides the benefits of a solid state laser, without the thermal management issues. The USAF currently is building the prototype Airborne Laser (ABL) which will utilize a chemical oxygen iodine laser (COIL). The COIL utilizes the chemical reaction of basic hydrogen
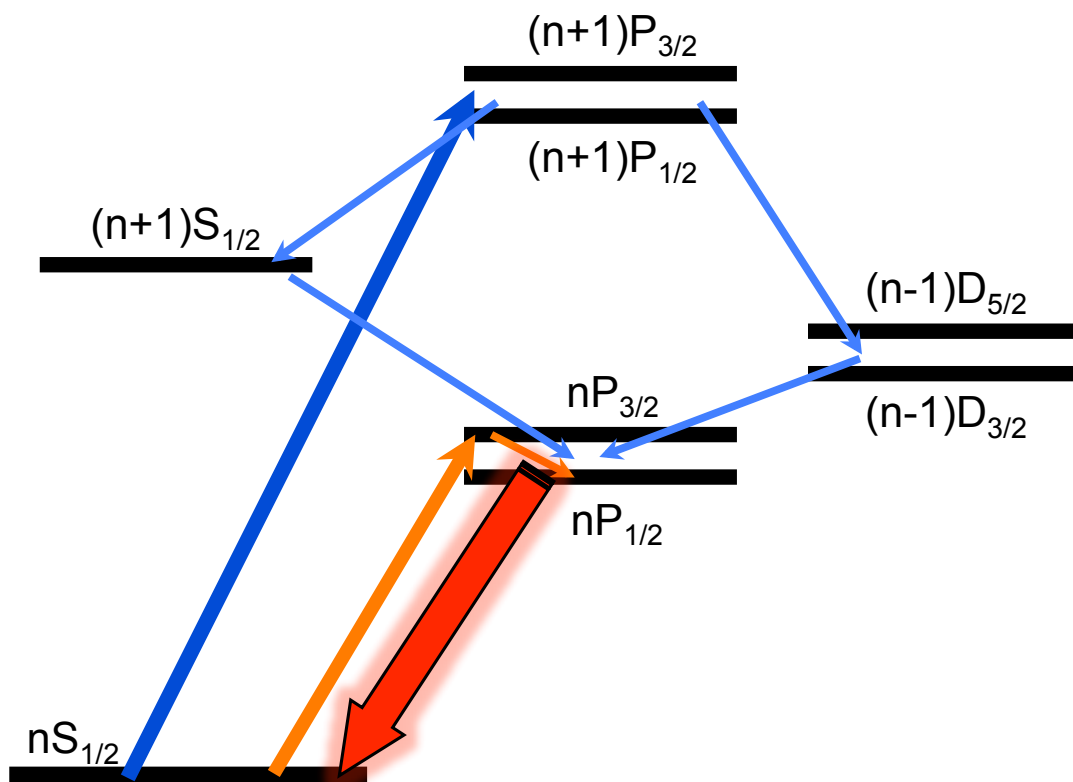
Figure 1. A general diagram of the transitions used for the laser proposed by Beach (Orange) and Schawlow (Blue).

peroxide and chlorine gas to produce an excited state of oxygen, $O_2(a,^1\Delta)$. This is shown in the following reaction:

$$Cl_2(g) + H_2O_2 \rightarrow O_2(a^1\Delta) + 2KCl + 2H_2O. \tag{1}$$
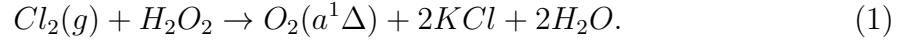
Due to the similarities in the energy differences, this excited oxygen is used to then pump atomic iodine to its first excited state. This chemical process is highly efficient and has produced the high powers needed for a weapon grade system, but this system requires a long logistics trail to get the basic hydrogen peroxide and chlorine gas to the battle field. The magazine of such a weapon is limited to the payload of the airframe. These drawbacks weigh heavily on the practicality of such a system. On the other hand, a solid-state laser could be powered by the jet engines on an aircraft. This would make the magazine depth limited to only fuel capacity of the airframe. But current solid-state laser systems have not achieved the high powers needed to be deployed in most tactical weapon systems. The inherent problem in solid state lasers (SSL) is thermal management. Temperature adversely affects the medium and its capability to lase, being that the medium is solid. This hinders the transport of this heat away from the medium quickly.

The DPAL system will have the benefit of high powers and efficiencies much like the COIL. These characteristics have been theoretically determined from the high slope efficiency and have been demonstrated via intensity scaling with the use of short-pulsed pumps.[63] Also, because it is currently expected to be pumped with diodes the infinite magazine depth of SSLs can be expected. The diode pump can be arranged as needed to deal with the thermal management and the alkali gas will simply be utilized as a filter to phase up the photons to produce a coherent beam. The alkali itself will not produce very much heat because of the small energy defect between the $^2P_{1/2}$ and $^2P_{3/2}$ states, shown in Table 1. The heat can simply flow out

4

of the system because this will all be accomplished in gas phase.

Table 1. The lasing transitions, pump transitions, and spin-orbit splitting between the $^2P_{3/2}$ and $^2P_{1/2}$ states for each alkali atom, ordered from smallest to largest mass.

Alkali	D_1(Laser) (nm)	D_2(Pump) (nm)	ΔE (cm^{-1})
Li	670.98	670.96	0.34
Na	589.76	589.16	17.2
K	770.11	766.70	57.7
Rb	794.98	780.25	237
Cs	894.59	852.35	554

Theoretically, the DPAL system is an ideal weapon system for the Department of Defense, but as the laser is scaled up it will face some challenges. One of these issues is matching the wide spectral profile of the pump diodes with the narrow absorption profile of the alkali. Two solutions have been suggested. One solution is to broaden the absorption profile via collisions with a buffer gas. This solution would require pressures up to 15 atmospheres to match the bandwidth of typical diodes as well as extremely well known values for the broadening rates which this work provides for cesium. The second solution would be to spectrally narrow the diodes with the use of volume Bragg gratings (VBG). The University of Central Florida, has demonstrated the use of VBGs with the diodes and have achieved linewidths of 10 GHz at the rubidium D_2 wavelength.[65] This still implies the use of pressure broadening but reduces the pressures needed to less than an atmosphere.

Another hurdle faced by this laser system is the bottleneck of the spin orbit energy exchange. As in typical 3-level lasers the rate at which the lasing state is populated is the limiting factor in the performance of the system. Currently, ethane is the most popular collisional partner used to collisionally relax the alkali from its $^2P_{3/2}$ state to its $^2P_{1/2}$ state. But this buffer gas has produced the degrading side effect of laser snow and soot. The carbon is then deposited on the windows affecting

5

the laser performance. Fortunately with the less massive alkalis and their smaller energy defect, rare gases can be utilized as an effective energy transfer partener. Recently a potassium laser using helium was demonstrated by the General Atomics with collaboration with AFIT.[74] In order for He in a potassium system to produce the same rate as 300 Torr of ethane in a cesium system, the potassium cell would have to have a pressure of approximately 2 atm of He. The pressure can be further lowered by a factor of 0.87, by using ^{3}He with its smaller mass and larger velocities. The measurement of these rates with cesium has been performed by this work.

The alkalis can not only be a laser medium for an intense red laser light source, but it can also be a source for blue and infrared light. Recently, it has been shown that by pumping with two red photons the highly excited S and D states can be populated.[64] Once these states are populated, an inversion between theses states and the second P state is created and an IR beam is produced. If pumped hard enough, it is possible to create a population inversion between the second P state and the ground state of the alkali. A blue beam was observed in cesium, rubidium, and potassium. [64, 44] A blue and IR laser would also be of interest to the DoD for underwater communication and as a countermeasure against heat seeking missiles.

Pressure Broadening

This body of work has measured the broadening and shift rates of cesium with various buffer gases and has calculated the potential energy differences between cesium and the buffer gas. These rates and potential energy curves were published in *Physical Review A* in 2009 and 2010 and are stated in chapters II, III, and IV. While these rates contribute directly to the DPAL community for the use of modeling the alkali laser system, the understanding of potential energy surfaces play a deeper role in the perception the complexity of the alkali-buffer gas interactions.

Spin Orbit

This work has also measured the spin orbit energy transfer rates between cesium and various molecular partners. These cross-sections for atom molecule interactions are essential for the DPAL 3-level laser models. The ability to recycle each cesium atom is dependent on the rate the spin orbit energy difference can be transfered to a buffer gas. If the rate is too slow this will create a bottleneck in the 3 level laser that may inhibit the creation of a population inversion. It has been shown that ethane has a large spin orbit energy transfer rate for Rb and Cs, but it has the disadvantage of creating laser snow and depositing carbon on the windows of the alkali cell. It would be ideal to find a buffer gas with a high spin orbit energy transfer rate but does not contain carbon. The values measured have been submitted to *Physical Review A* and are shown in chapter V.

Other Possible Alkali Lasers

This work has demonstrated two photon absorption in potassium to produce a blue beam at the wavelength of the $5^2P_{3/2} \rightarrow 4^2S_{1/2}$ transition. This is made possible by amplified spontaneous emission (ASE) from the excited state $6^2S_{1/2}$. IR ASE was confirmed in cesium as part of a collaboration with Sulham.[64] The potassium blue beam was observed up to 240 Torr and had a threshold of 260 kW/cm^2, which decreased as number density of potassium increased. Similar to the other alkalis, the relative slope efficiency increased as the number density increased.

An alkali blue laser can provide a means for underwater communication for the U.S. Navy. In addition, the IR alkali laser could be used to blind missiles that are heat seeking missiles. The results of this portion of work have been presented and published with American Institute of Aeronautics and Astronautics (AIAA) and are discussed in chapter VI.[44]

II. Pressure Broadening and Shift of the Cesium D_1 and D_2 lines in Diode Pumped Alkali Lasers

Introduction

The quest for a high power, electrically driven laser with excellent thermal management, lightweight packaging, and high brightness for tactical military applications may be realized with the advent of the Diode Pumped Alkali Laser (DPAL). The concept of using a gas phase medium for the phasing of large diode arrays via a highly efficient, cyclical photon engine combines the best features of electrically driven lasers with the inherent thermal management advantages of a gas lasers. There are several technical and scientific advances required to assess and realize the full potential of these hybrid lasers. Matching the spectral bandwidth of the diode pump source with the atomic absorption profile is paramount and requires both the narrow banding of high power diode laser arrays and novel approaches to broadening the gas lineshape. In the present work, the rates for pressure broadening and line shifts are reported for both atomic and molecular collision partners using laser absorption and induced fluorescence techniques.

Hyperfine Structure

The DPAL pump line, D_2 $5^2S_{1/2} \rightarrow 5^2P_{3/2}$, and lasing line, D_2 $5^2P_{1/2} \rightarrow 5^2S_{1/2}$, are the two components of the fine structure doublet, coupling the orbital angular momentum of the valence electron, L=1 or 0, to the spin angular momentum, S=1/2, to yield $\mathbf{J} = \mathbf{L} + \mathbf{S}$ and J= 1/2 or 3/2. The fine structure splitting in rubidium is large, E_{fs} = E($^2P_{3/2}$) - E($^2P_{1/2}$) = 237.595 cm^{-1}, and the spectroscopic data for each line of the doublet is reported separately. The splitting of the fine structure is called the hyperfine structure, which is the product of the coupling the resulting J with the

8

nuclear spin, I (I=3/2 for ^{8}7Rb and I=5/2 for ^{8}5Rb) with

$$| J - I | \leq F \leq | J + I | \quad (2)$$

Based on the quantum selections rules for F, the D_2 and D_1 lines are composed of six and four hyperfine components, respectively, for each of the two natural isotopes, as shown in energy level diagram of Figure 2. The hyperfine structure is described by the magnetic dipole and electric quadrupole interactions, yielding an energy splitting of:

$$E_{hfs}(F) = E_{fs} + A\frac{C}{2} + B\frac{\frac{3}{4}C(C+1) - I(I+1)J(J+1)}{2I(2I-1)J(2J-1)} \quad (3)$$

where

$$C \equiv F(F+1) - I(I+1) - J(J+1) \quad (4)$$

$$A = \text{magnetic dipole constant} \quad (5)$$

$$B = \text{electric quadrupole constant} \quad (6)$$

The corresponding hyperfine spectroscopic constants for Rb are provided in Table 2.

Stimulated Emission and Absorption Cross Sections

The hyperfine splitting is large enough that individual $F \to F$ transitions from the ground $^2S_{1/2}F$ state to the excited $^2P_{1/2}F$ state are resolved in the absorption spectrum for the Rb D_1 line of Figure 2. This spectrum was recorded using a narrow

9
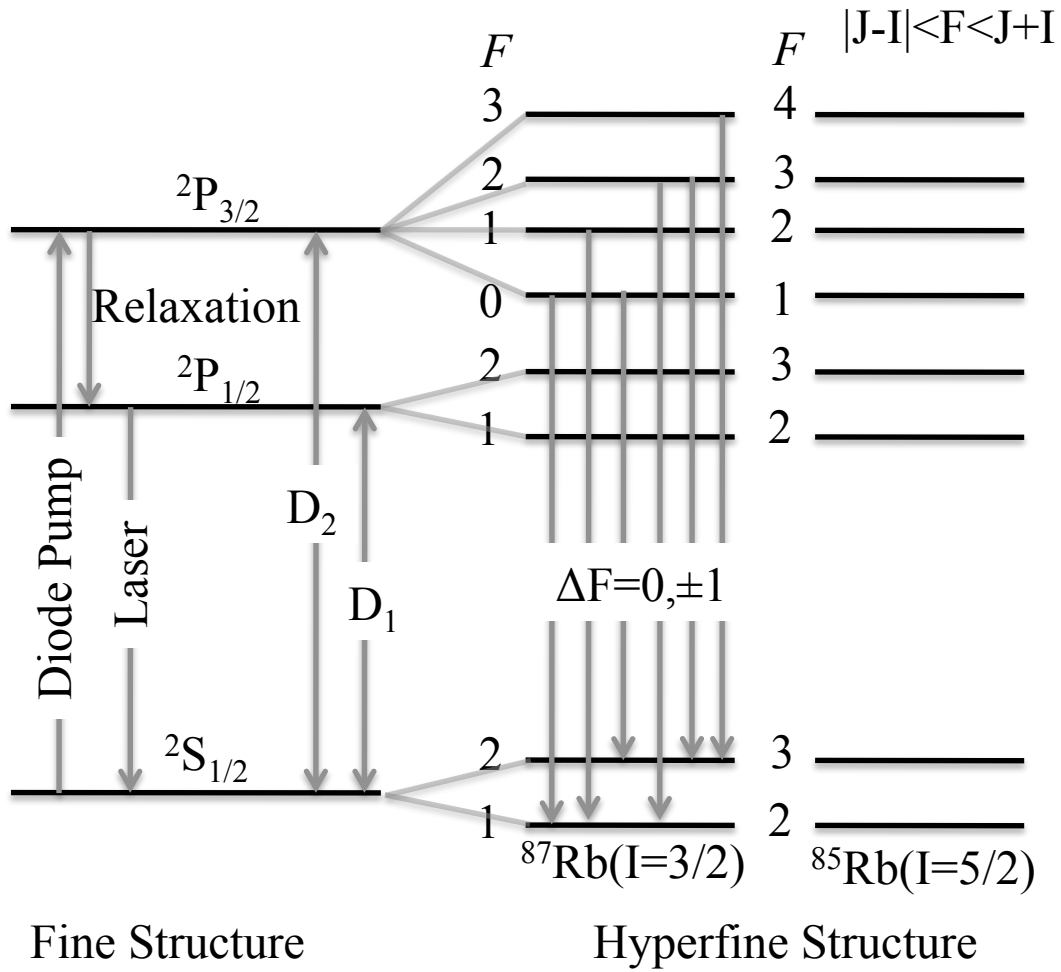
Figure 2. Hyperfine structure of the Rb D_1 and D_2 lines.

Table 2. Rubidium Hyperfine Spectroscopic Constants.[42, 7, 6, 14, 57, 10]

	^{87}Rb			^{85}Rb		
I	3/2			5/2		
f_{iso}	0.2783			0.7217		
	$^2S_{1/2}$	$^2P_{1/2}$	$^2P_{3/2}$	$^2P_{3/2}$	$^2P_{1/2}$	$^2P_{3/2}$
A (MHz)	3417.34120642	406.2	84.852	1011.910813	120.72	24.99
B(MHz)	———	——	12.611	———	——	25.88
g_j	2.00233113	0.6667	1.3362	2.0023313	0.6667	1.3362

band ($<$ 1 MHz) ring Ti-Sapphire laser for a rubidium cell at T $=$ 310 K with 50 Torr of helium[50]. The total optical cross-sections for absorption includes the contributions from each hyperfine transition in both isotopes, weighted by the fraction of the sample in the absorbing state:

$$
\begin{aligned}
\sigma\left(\nu\right) &= \sum_{F'',iso} \sigma\left(\nu; \nu_{F'\leftarrow F''}\right) f_{F''} f_{iso} \\
&= \sum_{F'',iso} \left(\frac{g_{J'}}{g_{J''}}\right) \left(\frac{\lambda^2}{8\pi}\right) \left(A_{21} S_{F'F''}\right) g_V\left(\nu, \nu_{F'\rightarrow F''}\right) f_{F''} f_{iso} \quad (7)
\end{aligned}
$$

where

$g_J = 2J + 1$

$\nu_{F'\leftarrow F''} =$ line center for the $F' \leftarrow F''$ hyperfine component

$\lambda = \frac{c}{\nu}$

$A_{21} = 1/\tau_R =$ spontaneous emission rate

$S_{F'F''} =$ hyperfine line strength for the $F' \leftarrow F''$ component

$g_V\left(\nu, \nu_{F'\leftarrow F''}\right) =$ Voigt lineshape centered at $\nu_{F'\leftarrow F''}$

$f_{iso} =$ relative natural abundance

$f_{F''} =$ statistical distribution of population among F'' states

$= \frac{(2F''+1)e^{-E(F'')/kT}}{\sum_{F''}(2F''+1)e^{-E(F'')/kT}}$

Table 3 provides the key spectroscopic data for the D_1 and D_2 transitions. There is small isotopic shift, δ_{iso}, for both the D_1 and D_2 lines.

The relative intensities of the four $F \rightarrow F$ transitions for each of the two isotopes

11

Table 3. Lineshape Data for Rubidium D_1 and D_2 Transitions[61]

Property	$D_1(^2S_{1/2} \rightarrow\ ^2P_{1/2})$	$D_2(^2S_{1/2} \rightarrow\ ^2P_{3/2})$
λ (nm)	794.9788501[50]	780.2412097 [50]
δ_{iso}	87.8 ± 1.9 [50]	87.4 ± 1.0 [50]
τ_R (ns)	27.7 [66]	26.24 [66]
$\lambda^2/(8\pi\tau_R)$	9.08×10^{-3}	9.23×10^{-3}
γ_{He} (MHz/Torr)	18.9 ± 0.2[51]	20.0 ± 0.14[51]
δ_{He} (MHz/Torr)	4.71 ± 0.04[51]	0.37 ± 0.06 [51]
γ_{CH4} (MHz/Torr)	29.1 ± 0.8[51]	26.2 ± 0.6[51]
δ_{CH4} (MHz/Torr)	-7.92 ± 0.10 [51]	-7.00 ± 0.20 [51]
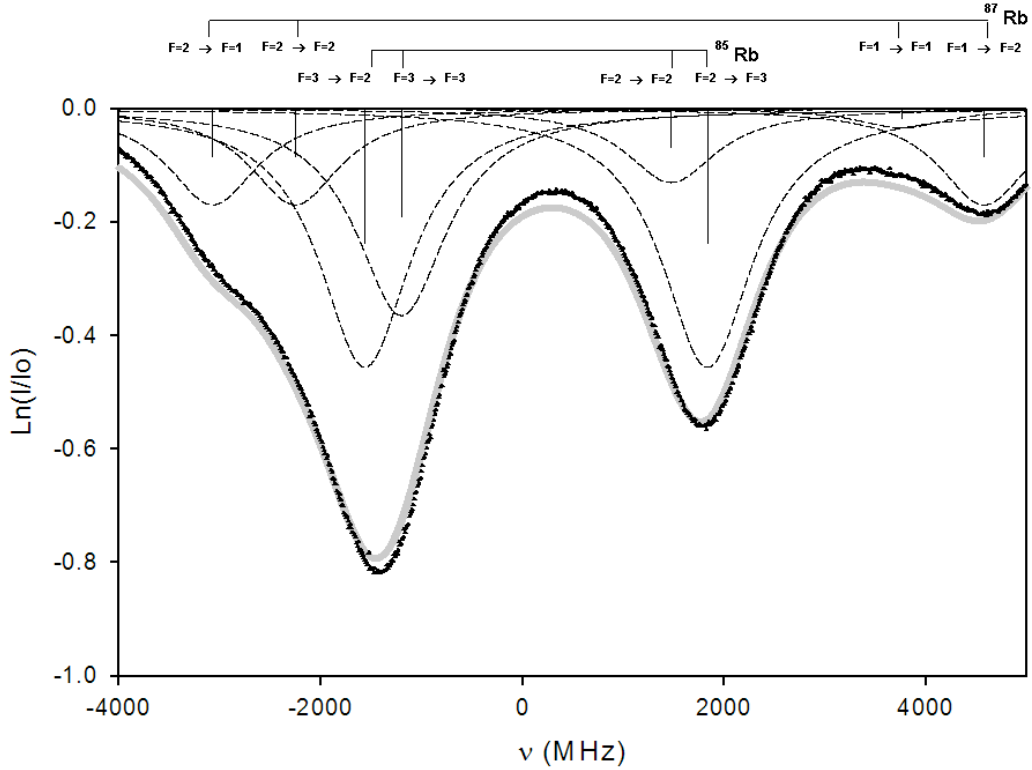
Figure 3. Absorption spectrum of Rb D_1 line: (•) Observed by tunable dye laser at T=311K and 50 Torr of helium, (———) simulation of equation (7), ($- - -$) Voigt profile for each hyperfine component. The stick spectrum indicates the relative amplitudes of each hyperfine component. Frequency is reported relative to low pressure reference cell.

Table 4. Ruibidium line strengths between hyperfine transistions.

$S_{F',F''}$		^{87}Rb			^{85}Rb	
	F	**1**	**2**	**F**	**2**	**3**
D_1 $^2S_{1/2} \rightarrow {}^2P_{1/2}$	**1**	1/6	1/2	**2**	2/9	5/9
	2	5/6	1/2	**3**	7/9	4/9
	0	1/6	—	**1**	3/10	—
D_2 $^2S_{1/2} \rightarrow {}^2P_{3/2}$	**1**	5/12	1/20	**2**	7/18	5/63
	2	5/12	1/20	**3**	14/45	5/18
	3	—	7/10	**4**	—	9/14

is specified by the hyperfine line strengths:

$$S_{F',F''} = (2F''+1)(2J'+1) \left\{ \begin{array}{ccc} J' & J'' & 1 \\ F'' & F' & I \end{array} \right\}^2 \tag{8}$$

where the final array is a Wigner 6-J symbol. Table III provides the line strengths for the D_1 and D_2 lines for each isotope. Note the line strengths represent the fraction of absorption partitioned to various final states so that the following sum rule is obeyed:

$$\sum_{F'} S_{F',F''} = 1 \tag{9}$$

Figure 3 includes an indication of each of the hyperfine line strengths, $S_{F',F''}$, weighted by the isotopic abundances, f_{iso}, and Boltzmann distribution factors, f_F, in the stick spectrum. The more abundant ^{85}Rb isotope exhibits a smaller $^2S_{1/2}$ hyperfine splitting so that the four stronger components lie toward the center of the spectral feature.

13

Linshapes

The Voigt lineshape is specified by the sample temperature, T, and the pressure broadening associated with each collision partner:

$$g_V(\nu, \nu_{F''\leftarrow F'}) = \frac{M}{2\pi k_B T} \int_{-\infty}^{\infty} g_L(\nu + \nu_0 \frac{v_z}{c}) exp\left(\frac{-Mv_z^2}{2k_B T}\right) dv_z \qquad (10)$$

with

$$g_l(\nu) = \frac{\Delta\nu_l}{2\pi \left[(\nu - \nu_0 + \sum_i \delta_i P_i)^2 + \left(\frac{\Delta\nu_l}{2}\right)^2\right]} = \text{Lorentzian lineshape} \qquad (11)$$

where:

M = mass of Rb atom

k_B = Boltzmann constant

T = gas temperature

$\nu_L = \frac{1}{2\pi}\left(\frac{1}{\tau_R} + \sum_i \gamma_i P_i\right)$ = Lorentzian (homogeneous) linewidth (FWHM)

T_L = temperature at which the broadening rate, γ, is measured

P_i = partial pressure of buffer gas i

v_z = atom velocity in the direction of light propagation

c = speed of light

The rates for pressure broadening, γ_i, and collision induced shifts, δ_i, for both helium and methane are included in Table 3. Note that these rates are temperature dependent, due to the dependence of collision frequency on density of the collision

14

partner. For example, the rate for pressure broadening by the ith buffer gas is:

$$R_i = \sigma_i g N_i = \sigma_i \left(\frac{8k_B T}{\pi \mu_i}\right)^{1/2} \left(\frac{P_i}{k_B T}\right) = \gamma_i(T_1) P_i \left(\frac{T}{T_1}\right)^{1/2} \tag{12}$$

where

$$\sigma_i = \text{collision cross-section for Rb with buffer gas i}$$

$$\mu_i = \text{reduce mass for Rb - i}^{th} \text{ specie pair} = \frac{m_{Rb} m_i}{m_{Rb} + m_i}$$

$$\tag{13}$$

The Maxwellian speed distribution within the integrand of equation (2.5) is characterized by the corresponding Doppler width (FWHM):

$$\Delta \nu_D = \nu_0 \sqrt{\frac{8k_b T ln(2)}{Mc^2}} \tag{14}$$

which is $\Delta \nu_D = 514$ MHz for Rb D_1 line at T=311 K. By summing over each of the hyperfine components as described in eqn. 3, the total absorption profile is simulated and compared to the experimental result in Figure 3. The Voigt profile for each hyperfine component, weighted by the relative amplitude, is also shown in Figure 3. The resulting predicted cross-section agrees quite favorably with the observed spectrum. There is a small variation in incident laser power across the spectral scan, leading to the small systematic difference. The absolute comparison depends on the Rb concentration, according to Beers law:

$$\left(\frac{I}{I_0}\right) = e^{\sigma N l} \tag{15}$$

where the absorption path length is $l = 1$ cm and the rubidium concentration, N,

has been computed from the vapor pressure at T = 318 K to be 1.10519×10^{-6} Torr, corresponding closely to the apparatus exterior wall temperature of T = 311 K. At the
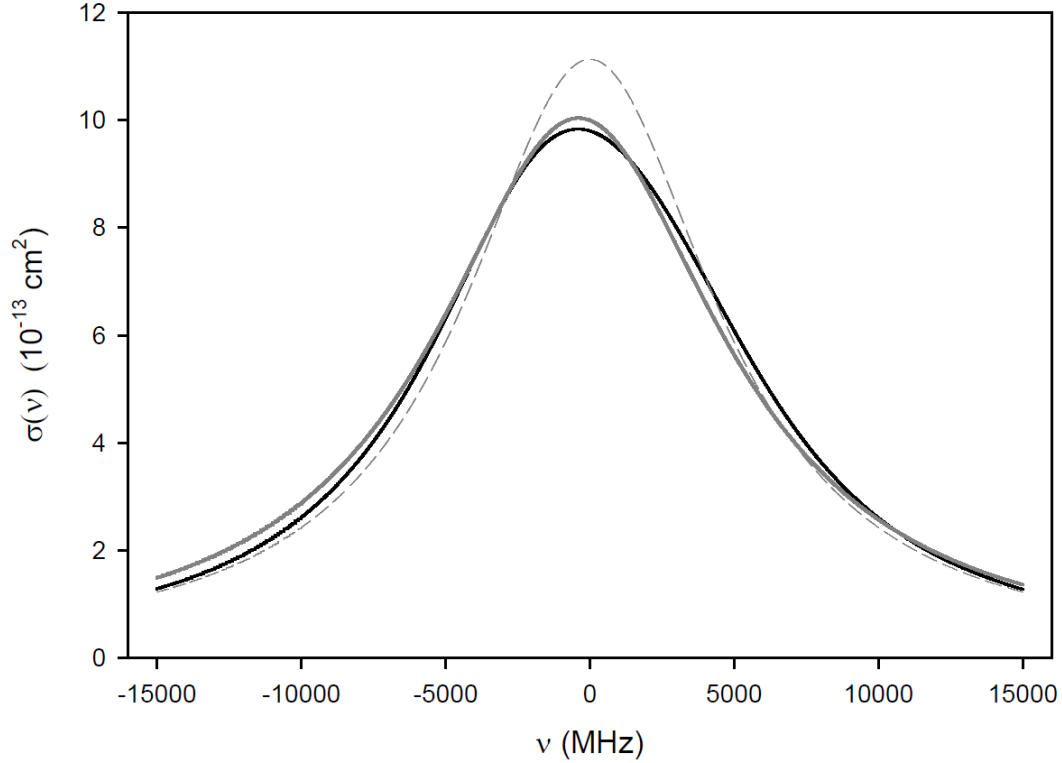
Figure 4. (——) **Absorption cross-section for D_1 line with 400 Torr of He and 100 Torr of methane from simulation of equation (7). Also shown:** ($- - -$) **a single lorentzian profile with the same broadening and shifting rates, and** (——) **least square fit of the simulation to a single Lorentzian profile.**

higher pressure typically employed in the Diode Pumped Alkali Laser (DPAL) system, the distinct features associated with the hyperfine structure blend into a single, but somewhat asymmetric line, as shown in Figure 4. Also shown in Figure 4 is a single Lorentzian without hyperfine splitting with the same broadening rates. Neglecting the additional effective broadening due to hyperfine structure overestimates the peak cross-section by 13.2 % for the He: Ethane = 400:100 Torr case. This difference is accentuated at lower pressures and Figure 5 presents the ratio of the peak cross-section
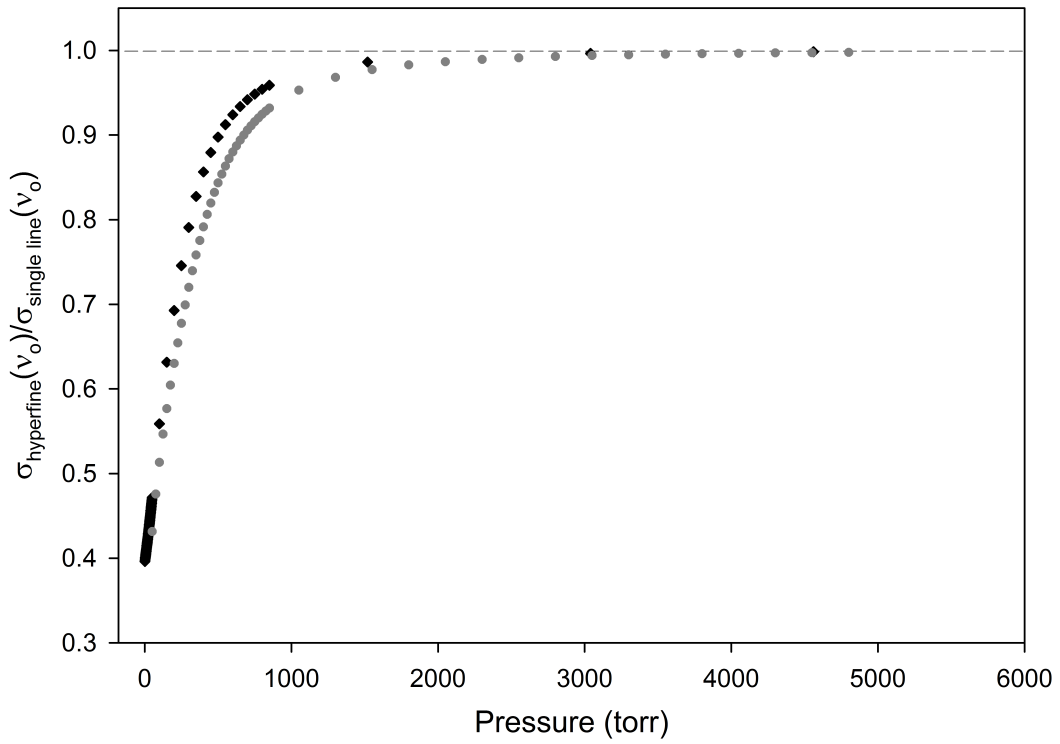
Figure 5. Ratio of the peak cross-section for the hyperfine simulation to the peak cross-section using a single Lorentzian profile with the same broadening rate for the (♦)D_1 and (•)D_2 lines.

for the hyperfine split transition to the same cross-section, neglecting the hyperfine splitting. Only for total pressures of several atmospheres is the Lorentzian profile without hyperfine splitting adequate. It is possible to fit a single Lorentzian profile to the hyperfine split lineshape, as shown in Figure 4. Such a fit yields a linewidth of $\Delta\nu_h = 12{,}205 \pm 20$ MHz which is larger than that predicted without hyperfine splitting, but less than the effective width predicted by the hyperfine structure. As a result, the peak cross-section is somewhat larger than would be observed.

III. Pressure Broadening and Shift of the Cesium D_1 Lines

Introduction

The lineshape, broadening, and shift of the atomic hyperfine profiles due to collisions with other atoms or molecules have been studied thoroughly and numerous reviews are available [2, 23]. The alkali's have been of recent interest as a lasing medium for diode pumped gas lasers. These alkali lasers were proposed by Krupke in 2003 and demonstrated by Beach in 2004, but this system may be considered an adaptation of a system first proposed by Schawlow and Townes in 1958 and built by Rabinowitz in 1962 [32, 8, 55, 47]. This current effort will utilize large diode bars to pump the D_2 transition of the alkali and lase along the D_1 transition. This Diode Pumped Alkali Laser, DPAL, is a three level laser system that depends heavily on saturation of the pumped state, therefore the linewidth matching of the D_2 transition with the diode bar or stack is crucial. Diode bars and stacks typically have a linewidth of 30 GHz which would force the cesium to be exposed to pressures up to 10 atm. The DPAL models are then dependent on the accuracy of the information on the collisional effects on the alkali. As part of a study to measure the spin-orbit energy transfer between the $6^2P_{1/2}$ and $6^2P_{3/2}$ states, the broadening and shift rates for the $6^2P_{1/2} \leftarrow 6^2S_{1/2}$ transition have been measured.

With the exception of two recent studies, the collisional effects on the cesium D_1 transition have not been updated since 1990 [4, 15, 25]. Andalkar utilized laser absorption spectroscopy in 2001 to study the effects of N_2 and He on Cs up to 160 Torr. Andalakar was able to achieve errors less then 1.2% [4, 3]. In 2008, Couture utilized a flash lamp and spectrometer to measure the shift and broadening rates of He, N_2, and ^{129}Xe with errors less than 3% [15]. One study in 1990, by Inoue, produced results with errors less than 1.6% [25]. The Inoue study utilized laser

absorption spectroscopy and was limited not by the measurement of the widths of the spectrum but the measurements of the pressure, which had an error of 10%. The studies prior to 1990 produced results with errors around 20%, and most of these studies were performed at pressures less than 160 Torr [21, 11, 12, 59, 26]. In addition to these experimental values for the collisional effects on cesium, Jacobson theoretically determined the values for broadening and shift rates for cesium with Argon, Krypton, and Xenon from the interatomic potentials [27].

The rates that are currently available from these works vary greatly between each other. In the case of helium there is a discrepancy of 10 MHz/Torr for the broadening rate and for nitrogen there is a 11 MHz/Torr difference. Andalakar pointed this out in his study in 2001, but his study only included nitrogen and helium. This study provides updated rates for all the noble gases and H_2, HD, D_2, N_2, CH_4, C_2H_6, CF_4, and ^{3}He. Of which, HD, D_2, CH_4, C_2H_6, CF_4, and ^{3}He have never been measured. The lighter isotope of helium has been predicted from theory by Couture using the ratio of reduced masses and the rate for ^{4}He. Also, no previous study witnessed any non-voigt lineshapes at low pressures and therefore did not determine if it has an effect on the collisional broadening and shift rates.

Experiment

This experiment utilized a Coherent MBR-110 Ti:Sapphire ring laser tuned to 894 nm and scanned over 35 GHz. The ring laser, which was pumped by a Coherent Verdi V-18 diode laser, has a linewidth less than 100kHz with a power less than 3.5 Watts. This beam was greatly attenuate ($< 1\mu Watts$) before reaching the test cell to avoid any saturation broadening and to stay within the Beer's law regime of absorption. The scan time was converted to the frequency utilizing an etalon with a free spectral range of 299.45 MHz, which was calibrated using the extremely well known hyperfine

spacing of the D_1 line. The output of the ring laser was amplitude modulated, at a frequency of 1505 Hz, and coupled into a trifurcated fiber bundle. Each branch of the bundle was focused onto a different Hamamatsu silicon photodiode (model S2281-04). The photodiodes were employed to record the incident intensity on the cesium cells, a reference spectrum for an absolute frequency measurement via a low pressure cell, and the transmitting intensity of the test cell while observing the changing absorption profile.

Each cell was constructed from a one inch cylinder made of pyrex glass with an ampoule of cesium attached underneath. The cells were affixed to the gas handling system with UltraTorr seals. This allowed for pressure measurements at the time of the scan while previously used prefilled cells only allowed for pressure measurement at the time it was filled, which created systematic error in addition to the pressure measurement error. The gas handling system also reduced the possibility of exposure to air and moisture, which would result in contamination of the cesium sample and could result in fire and creation of the very strong base, CsOH.

The cell was placed in a temperature controlled aluminum block, with the ampoule exposed underneath. This configuration of the cesium ampoule and the oven was designed such that they could be controlled at two different temperatures, allowing for better control of the number density of the cesium in the upper cell. The temperature controller maintained the temperature within 1°C. The vapor pressure at the highest temperature (333 K) was 47.25±3.86 μTorr [61]. The control of the temperature and number density was import to control the Doppler width and to avoid self-absorption issues at higher temperatures. Early on in the experimental process higher temperatures were used and this effect was seen in the relative amplitudes of the hyperfine spectrum at temperatures over 100°C.

Cell pressure was monitored by MKS model 690A capacitance manometers with

heads for 1000, 100, 10, and 1 Torr for cell pressures ranging from under 1 mTorr to 300 Torr. The cesium was 99.98% pure and all gases had a purity greater than 99.9 % purity, with the one exception of HD which had a purity of 97.3 %.
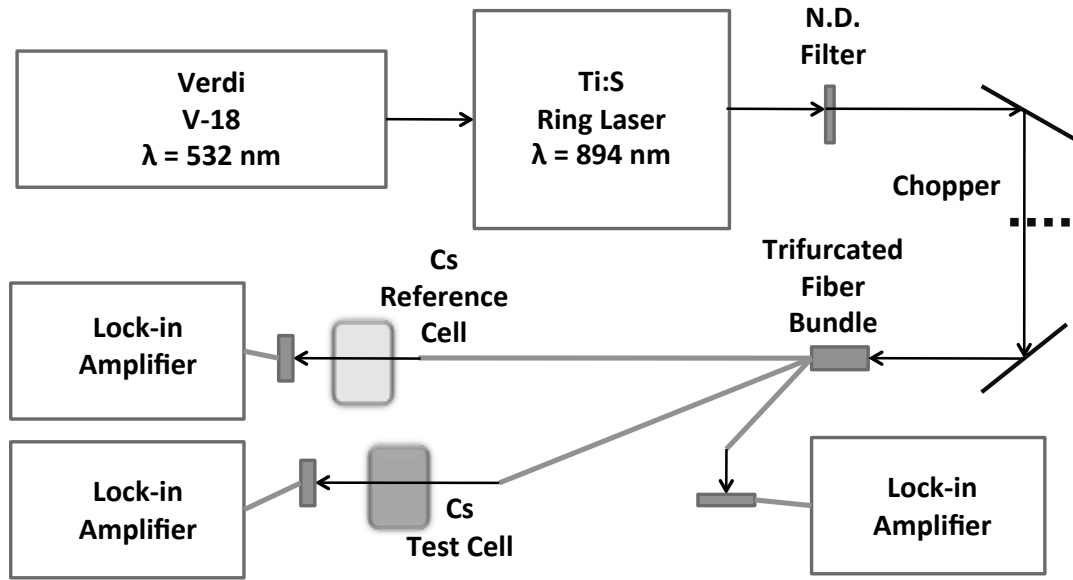
Figure 6. Experimental apparatus for laser absorption spectroscopy.

As shown in Figure 6, phase sensitive detection was employed to monitor the transimitted laser intensities utilizing Stanford Research Systems lock-in amplifiers, model SR850. The recorded transmitted intensities, I, were ratioed with the incident intensity, I_0, which removed the low frequency power fluctuation from the laser. A small linear background was observed over the 35 GHz scan of the ring laser, which had a relatively small slope in comparison to its offset, 1.4×10^{-3} %. This was mathematically removed from the known absorption profile during the numerical fitting of the spectrum.

Results

The hyperfine spectrum of the cesium D_1 transition is shown in Figure 7, where the larger ground state splitting (9.192631770 GHz) and the smaller $^2P_{1/2}$ state splitting

22

(1.167680 GHz) is observed [61]. In Figure 7, the lineshape profile is shown at multiple pressures for ^{3}He and is a typical demonstration of all buffer gases and spectrums. Each spectrum, which has an average signal to noise ratio of 700, was collected over 3 minutes and consist of over 100,000 data points. Each individual hyperfine component is observed at 0-100 Torr and, as expected, becomes more convoluted as pressure increases but the larger ground state hyperfine splitting is still evident at 300 Torr. The hyperfine profile plays a significant role in the total lineshape of the transition spectrum even at 1 atmosphere [43]. In the sample spectra shown in Figure 7, the ^{3}He spectra is slowly blue shifted, which is only observed for the lighter species studied which also includes, He, H_2, HD, and D_2.
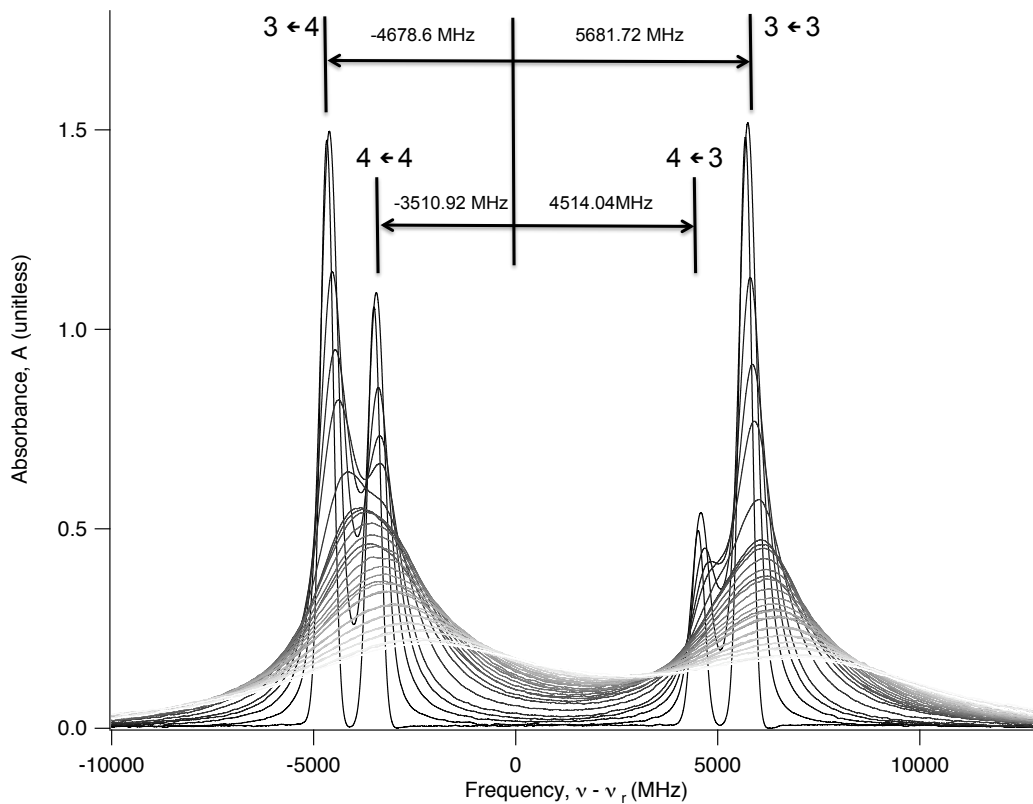
Figure 7. The cesium D_1 hyperfine lineshape pressure broadened by ^{3}He from 10-300 Torr (in steps of 10 Torr) with the assigned (F'←F") hyperfine transitions.

23

The Lorentzian width and line center were determined from the absorption profile, by a numerical fit of the spectrum to a set of four Voigt lineshapes:

$$A = -Ln \left(\frac{I}{I_0} \right) = c_0 + c_1 \nu + c_2 \sum_{i=1}^{4} a_i V (\nu_i + \delta \nu, \Delta \nu_L; \gamma_D), \tag{16}$$

where $c_{0,1}$ are the coefficients for the linear background and c_2 is the absolute absorbance constant. The absorbance, A, is defined as $\sigma l n$, where σ is the cross-section, l is the path length of the cell, and n is the number density. Each of the four hyperfine lines have been assumed to share the same Doppler, γ_D, and Lorentzian width, $\Delta \nu_L$. Initially, the Lorentzian widths were allowed to vary but at low pressures they were alway within the error bounds of the other hyperfine lines. Both widths were measured as full width half max, FWHM, values. The Doppler width was calculated via the formula:

$$\gamma_D = 2 \cdot \nu \sqrt{2 \cdot ln(2) \frac{k_b T}{mc^2}}, \tag{17}$$

where ν is the frequency, k_b is the boltzmann constant, T is the temperature, m is the mass, and c is the speed of light. At the maximum temperature, 338 K, for this experiment the Doppler width is 384 MHz and the hyperfine lineshape was constrained to have this calculated value of the Doppler width for its corresponding temperature. The hyperfine spectrum was also assumed to share a single spectral shift, $\delta \nu$, and each hyperfine line position, ν_i, is well known. A normalized Voigt profile, V, which utilized each of the known hyperfine linestrengths, a_i, was employed. The linestrengths are calculated from product of the fractional Boltzmann population of the ground state and the transition strength, which are shown in Table 5. The Voigt shape term was found to have a value of unity ($\Delta \nu_L = \gamma_D$) at a pressure of 20 Torr with an average broadening rate of 20 MHz/Torr.

Several fits to equation (16) to the observed spectra, with corresponding fit resid-

Table 5. Cesium hyperfine transition strengths for the D_1 transistion.

Transition $S_{F\ F'}$	Strength (unitless)
$S_{4\ 4}$	5/12
$S_{4\ 3}$	7/12
$S_{3\ 4}$	3/4
$S_{3\ 3}$	1/4

uals, are provided in Figure 8. The signal-to-noise is about 1500, allowing for an observation of the lineshape well in to the wings, with scan range of more than 130 Doppler widths. At pressures about 80 Torr, the average fit residuals are unstructured and about 10^{-5} %. For the lowest pressures (P < 80 Torr) a small systematic deviation from the Voigt profiles is observed. Allowing greater flexibility in the fitting equation (16) by varying the Doppler width, relative Lorentzian widths of the hyperfine components, or the hyperfine line strengths does not significantly reduce the structured residuals. Line narrowing due to velocity changing collisions was examined using several forms of the Gallatry profile [18, 19]. While the qualitative features of the residuals are indeed matched, further analysis is required to fully characterize the rates for the velocity changing collisions. The effects of the small residuals at low pressures on the pressure broadening and the shift rates is negligible as discussed below. Prior studies of the O_2 A band exhibited line narrowing also demonstrate the minor effects on the reported Lorentzian fit parameters [49].

The extracted shifts, $\delta\nu$, and Lorentzian width, $\Delta\nu_L$, are displayed as a function of pressure with various non-reactive collisional partners in Figs. 9 and 10. A linear fit of the data was performed and the extracted slopes are the shift and broadening
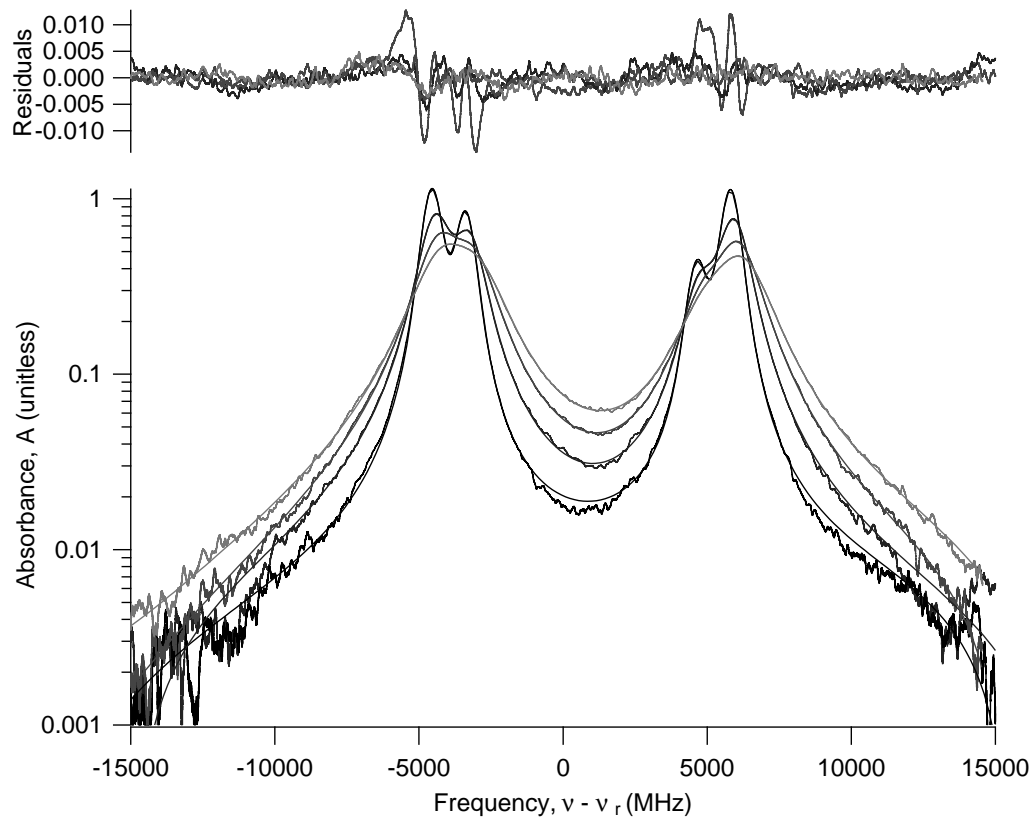
25

Figure 8. A sample of the resultant fits with residuals to equation (25) for the D_1 transition under the influence of ^{3}He at 20, 40 , 60, and 80 Torr.

rates. This corresponds to the following formula for the Lorentzian width:

$$\Delta\nu_L = \gamma P + \gamma_N, \tag{18}$$

where γ is the broadening rate for the buffer gas, and γ_N is the natural width. The natural width is 4.575 MHz, which was calculate from the known lifetime of 34.791 ns. The natural line width was used for the y-intercept and was fixed for the weighted linear fits that were performed on the data. Similarly, the shifts were fit to a line but with an intercept of 0 and the slope is the shift rate, δ.

The resultant broadening and shift rates with their corresponding slope fit errors are shown in Tables 6 and 7. The rates listed were determined from the fit of a line with a fixed y-intercept. In other fits, the y-intercepts was allowed to vary and on average varied 0.06 MHz/Torr which is less than the average standard deviation. Also, the average y-intercept parameter was 2.25 MHz with an error of 9.89 MHz. The natural linewidth lies within the error bounds of the y-intercept parameter. Secondly, to determine the effect of the systematic residuals on the width and shift rates the points extracted from spectrum with this effect in the residuals were removed from the fit of equation (18). This produced on average no overall change of the slope of the line and all values for the broadening and shift rates were still well within the error bounds reported in Tables 6 and 7.
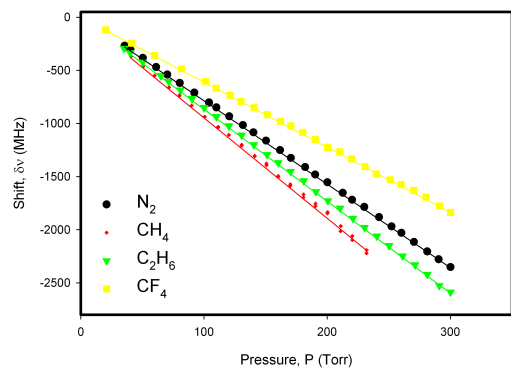
The only other major contributing factor to the total error was from the pressure measurements, each of which had an error of 0.08%. The slope error was determined from a weighted fit of the data, where the weights were determined from the reciprocal of the Lorentzian width error. The error in the width and shifts was less than 0.34% on average.
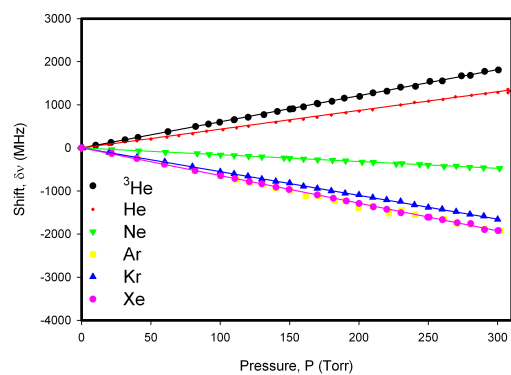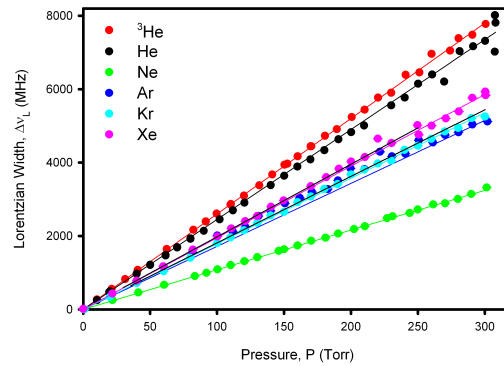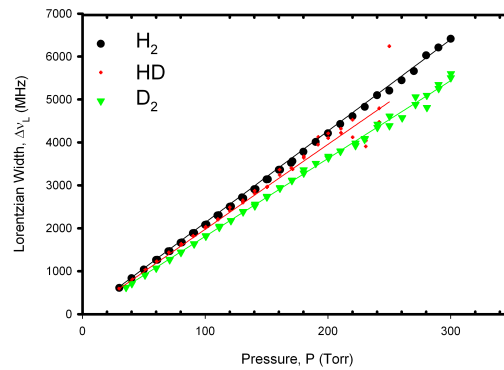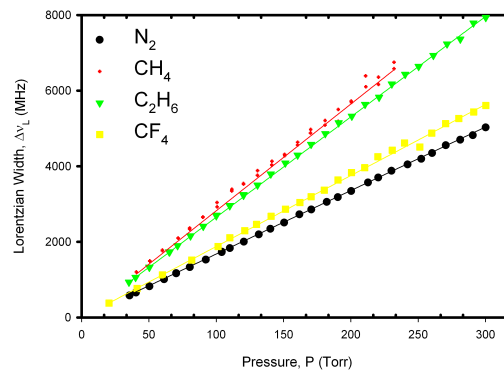
(a)
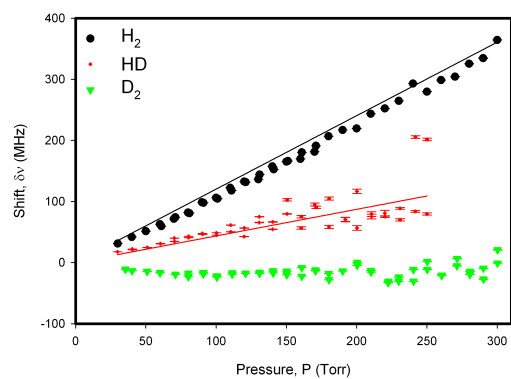
(b)

(c)

Figure 9. D_1 hyperfine profile shift as a function of pressure of (a) the noble gases, (b) various hydrogen isotopes, and (c) several molecules.

28

Figure 10. D_1 hyperfine profile broadening as a function of pressure of (a) the noble gases, (b) various hydrogen isotopes, and (c) several molecules.

29

Table 6. Measured values for the broadening rate for the D_1 transition compared to the previous results.

	Current Work			**Previous Work**		
		γ_1[a]		γ_2	γ_{adj}[b]	**Ref.**
Gas	$T_1(K)$	**MHz/Torr**	$T_2(K)$	**MHz/Torr**	**MHz/Torr**	
He	323	24.13±0.07	294	26.21±0.31	25.42	[4]
			295	19.49±1.35	18.62	[12]
			393	28.42±1.03	31.34	[15]
^{3}He	323	26.00±0.05	393	21.71±0.70[c]	23.94	[15]
Ne	313	10.85±0.02	295	10.13±0.86	9.75	[12]
Ar	313	18.31±0.16	295	19.64±0.23	19.06	[12]
			295	14.99[d]	14.55	[27]
Kr	313	17.82±0.05	295	19.84±2.5	19.26	[11]
			295	15.29[d]	14.84	[27]
Xe	313	19.74±0.08	295	21.49±2.60	20.86	[11]
			295	17.09[d]	16.59	[27]
H_2	328	20.81±0.09	295	40.42±6.20	39.24	[11]
HD	318	20.06±0.12	—	—	—	—
D_2	318	18.04±0.04	—	—	—	—
N_2	318	15.82±0.05	294	19.51±0.06	19.07	[4]
	323	16.36±0.02	295	30.93±5.71	29.33	[12]
	333	15.66±0.08	393	14.73±0.69	16.00	[15]
CH_4	333	29.00±0.10	—	—	—	—
C_2H_6	331	26.70±0.03	—	—	—	—
CF_4	318	18.84±0.05	—	—	—	—

[a] Error from a weighted linear fit only.   [b] See Eqn. (21)   [c] Calculated value from ^{4}He.
[d] Calculated from theoretical interatomic potentials.

Table 7. Measured values for the shift rates for the D_1 transition compared to the previous results.

	Current Work		Previous Work		
Buffer Gas	**Temp. (K)**	δ^{a} **(MHz/Torr)**	**Temp. (K)**	δ **(MHz/Torr)**	**Ref.**
He	323	4.24±0.02	294	4.46±0.03	[4]
			295	6.61±1.00	[12]
			393	4.45±.69	[15]
^{3}He	323	6.01±0.01	393	5.82±1.03$^{\text{b}}$	[15]
Ne	313	-1.60±0.01	295	-2.88±0.09	[12]
Ar	313	-6.47±0.03	295	-8.73±0.4	[12]
			295	-5.4$^{\text{c}}$	[27]
Kr	313	-5.46±0.01	295	-2.65±0.10	[12]
			295	-5.4$^{\text{c}}$	[27]
Xe	313	-6.43±0.01	295	-8.09±1.2	[12]
			295	-6.3$^{\text{c}}$	[27]
H_2	328	1.11±0.01	295	2.25±0.19	[12]
HD	318	0.47±0.03	—	—	—
D_2	318	0.0009±0.00004	—	—	—
N_2	318	-7.69±0.01	294	-8.23±0.02	[4]
	323	-7.71±0.01	295	-7.38±0.11	[12]
	333	-7.41±0.01	393	-8.90±0.69	[15]
CH_4	333	-9.28±0.02	—	—	—
C_2H_6	331	-8.54±0.01	—	—	—
CF_4	318	-6.06±0.01	—	—	—

$^{\text{a}}$ Error from a weighted linear fit only. $^{\text{b}}$ Calculated value from ^{4}He.
$^{\text{c}}$ Calculated from theoretical interatomic potentials.

Discussion

In general, the present broadening rates are in approximate agreement with all but the earliest of the prior work. However, a detailed comparison requires an assessment of the temperature dependence. These rates are certainly influenced by differences in the average relative speed, g, of the collision pairs, and may be further modified by an energy dependence to the cross-section, σ: [62]

$$\gamma = \frac{N}{P} \int_0^\infty \sigma(g) g f(g; T) \, dg, \tag{19}$$

where N is the number density and P is the pressure. The temperature dependence of the Maxwellian speed distribution, $f(g; T)$, and the relative speed,

$$g = \sqrt{8 k_b T / \pi \mu}, \tag{20}$$

where μ is the reduced mass of the collision pair, leads to a temperature dependence of the broadening rate often described as [28]:

$$\gamma_2 (T_2) = \gamma_1 (T_1) \left(\frac{T_1}{T_2} \right)^n. \tag{21}$$

Note that the collision rates are dependent on concentration and the pressure is related to the concentration via another temperature factor, $P = n k_B T$. If the cross-section is independent of speed, $\gamma \approx g\sigma$ and $n = 1/2$. Table 6 provides the broadening rates scaled to the current temperatures for comparison. A test of the energy independence of the cross-section is best afforded by the current temperature dependence of the nitrogen data provided in Figure 11, which shows no change in the cross-section of nitrogen as temperature is increased over a small range.

The shift rates are also in agreement with the previous studies, but a direct com-
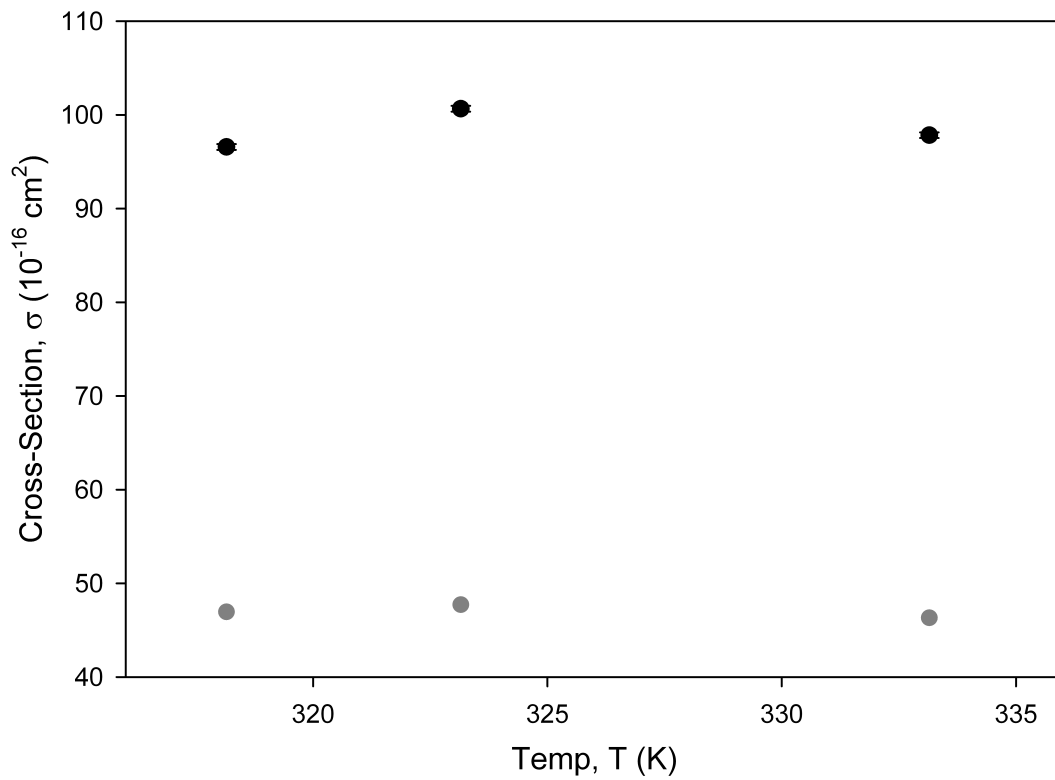
32

Figure 11. The cross-section for broadening (●) and shift (●) of Cs-N$_2$ interaction at three different temperatures.

parison is difficult with current data. These rates can be calculated from the cross-section and the velocity distribution, but in the case of the shifts, the cross-section may have a more significant energy dependence. So, the assumption used for the broadening rate comparison cannot be made and thus the value of n≠1/2. Couture attempted to determine the value of n for his rates utilizing both his and Andalakar's data [15]. Couture calculated the value for He to be 1.6±.5, while this current study has shown the value for n in the Cs-N$_2$ interactions is approximately 1/2. With such limit amount of data and large error bounds, further study is needed.

Equations (19 & 20) have been utilized by Couture to show a means for calculating the rates for similar atoms with slight differences in mass, as is the case for ^{4}He and ^{3}He. This mass dependence arises from the relative speeds in equation (20) and can be expressed:

$$\gamma_2\left(T_2\right) = \gamma_1\left(T_1\right)\left(\frac{\mu_2}{\mu_1}\right)^{1/2}. \tag{22}$$

Employing this expression Couture calculated the value within 1.7 MHz/Torr of the value obtained in the laboratory. This difference may again be explained by an energy dependence within the cross-section which may depend on the individual atomic potentials.

From the rates themselves the inter-atomic potentials can be calculated. These potentials can be determined by using the ratio of the broadening and shift rates and the impact approximation[54]. Assuming the potentials have a Leonard-Jones form:

$$V(R) = C_{12}R^{-12} - C_6 R^{-6}, \tag{23}$$

where R is the interatomic separation and C_6 and C_{12} are the coefficients for the R^{-6} and R^{-12} parts of the potential respectively. The broadening and shift rates have been analyzed before utilizing this approach [23]. The potentials derived from this

work are shown in Figure 12. These curves compare closely to those of Rotondaro's work with rubidium [51]. This comparison is shown in Figure 13, with slightly smaller interatomic distances (1.4-2.6 Angstroms) and binding energies down to 0.16 meV of N_2 up to the repulsive potential of ^{3}He. Yet, this model has ignored the effects of rotational degrees of freedom, non-spherically symmetric potentials, spin-orbit energy transfers, and any curved trajectories.

The impact approximation and the Leonard-Jones potential suggests a linear correlation between the probability per collision for phase changing collisions and polarizability. The present result are consistent with this prediction and is illustrated in Figure 14. The ratio for the gas kinetic cross-section:

$$\sigma_g = \pi \cdot (r_{Cs} + r_{buffergas})^2, \tag{24}$$

were evaluated from reference [24]. The polarizability for the buffer gases was found in reference [5]

Conclusions

The reported rates for collision induced line broadening and shifts for the cesium D_1 line with errors of about 0.3% enable enhanced accuracy in modeling the performance of Diode Pumped Alkali Lasers. Conversion of the observed rates to the interatomic potential unifies the results for a wide range of buffer gases and enables the comparison to another heavy alkali; Rb. The effects of the line narrowing are observed at low pressures, further analysis is needed to discern the role of velocity changing collisions.
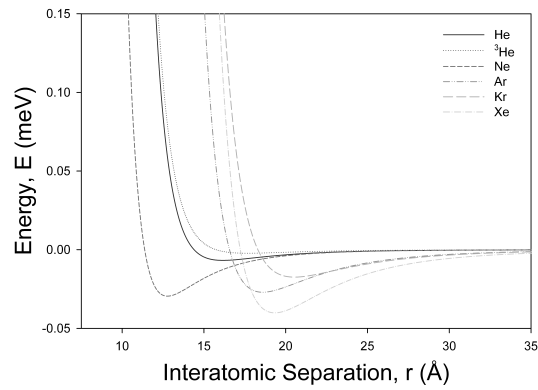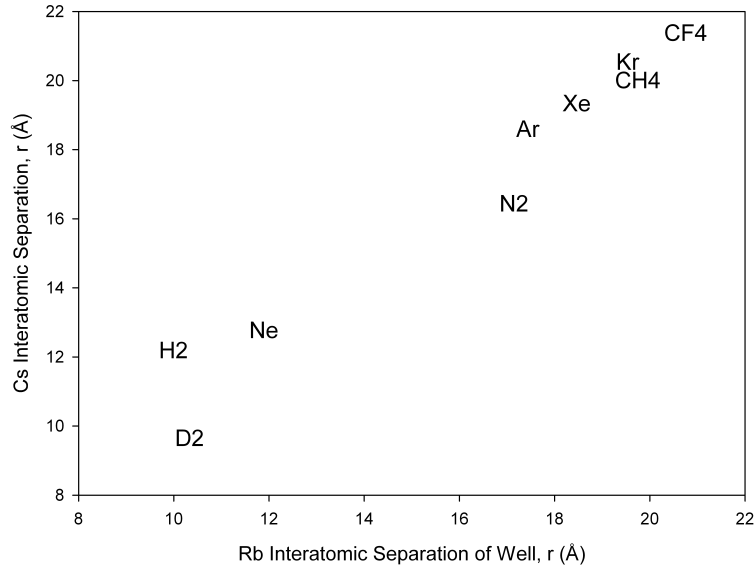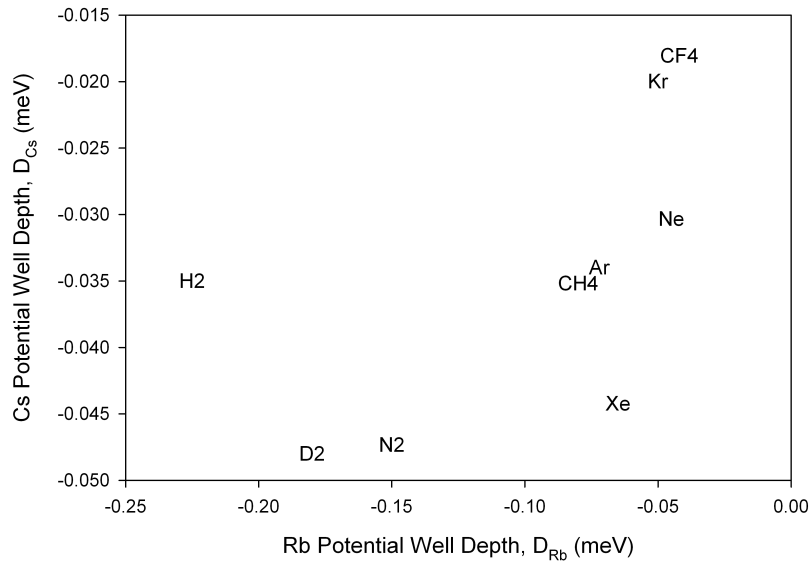
(a)
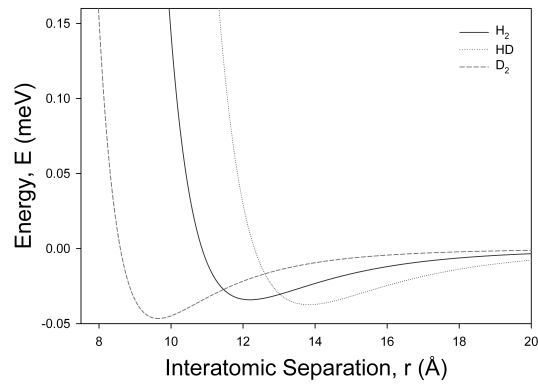
(b)
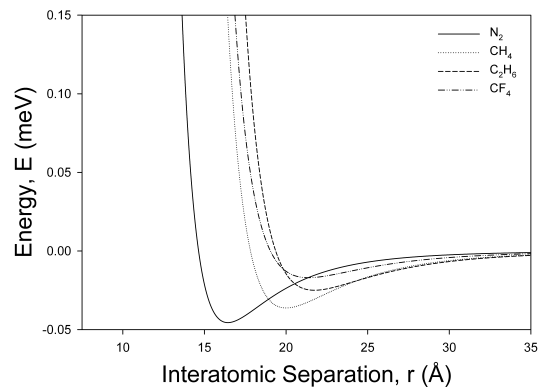
(c)

Figure 12. The Leonard Jones potentials for the Cesium D_1 transition with (a) the noble gases, (b) various forms of hydrogen, and (c) an assortment of molecules.

(a)

(b)

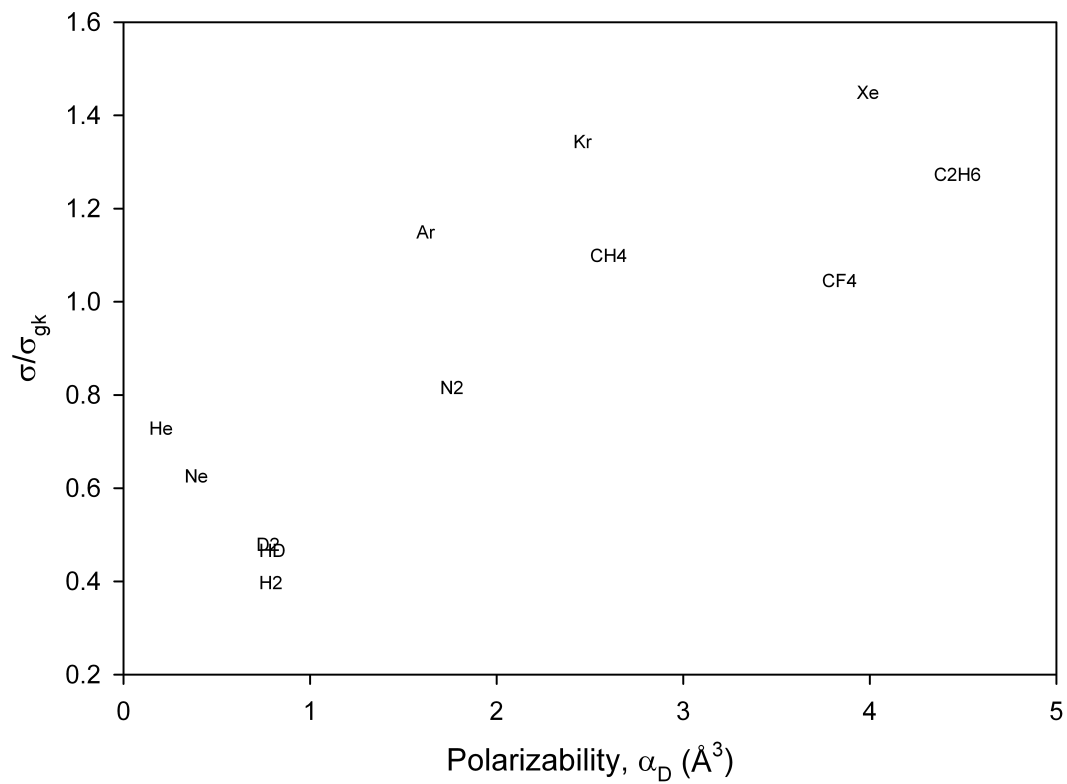**Figure 13.** Comparison between the well depths (a) and the interatomic separation (b) of cesium and rubidium.

Figure 14. Correlation of the probability for phase changing collisions in the D_1 transition with dipole polarizability of the collision partner.

IV. Pressure Broadening and Shift of the Cesium D_2 Transition

Introduction

The efficiency and power scaling of solid state lasers has been dramatically improved by replacing flash lamp excitation with high power diode bars and stacks [33]. Extending the application of diode pumping to high power gas phase lasers offers improved thermal control of the gain medium and enhanced beam quality, but requires matching of the relatively broad spectral width of the diode pumps to the very narrow gas phase absorption features. A prominent approach to such a system, the Diode Pumped Alkali Laser (DPAL), was demonstrated by Krupke et al in 2003 and by Beach et al in 2004 [32, 8]. Indeed, the remarkable optical properties of the alkalis allows for efficient phasing of many diodes via: (1) optical excitation of the first $^2P_{3/2}$ state on the D_2 transition, (2) collisional relaxation to the spin-orbit split $^2P_{1/2}$ state, and (3) lasing back to the ground state along the D_1 transition. A single alkali atom can be cycled in this system at rates exceeding 10^{10} s^{-1} [40].

Typical diode bars have a linewidth of $\approx$30 GHz requiring gas pressures of up to 10 atmospheres for efficient absorption. Recent success in narrow banding diode bars using external volume Bragg gratings appear to enable sub-atmosphere pressures for the DPAL system [65]. Alternatively, optically pumping transient alkali-rare gas molecules to dissociative state which populates the upper laser level has also been recently demonstrated [48]. In all cases, the collision induced broadening and shift of the alkali D_1 and D_2 lines are key to laser performance. The ideal buffer gas in these laser systems should offer rapid spin-orbit relaxation rates, no quenching, and minimal reactivity, in addition to the effective lineshape broadening. As part of a program to develop the spectroscopic and kinetic database for these lasers, we

39

recently reported the collisional broadening and shifting of the D_1 line in Cs [46]. This paper reports on a continuation of this study for the pump transition on the Cs D_2 line.

The lineshapes for the Cs D_2 transition have been studied in some detail from 1966 through 2008 [21, 12, 4, 15]. The most accurate report using laser absorption spectroscopy is limited to helium and nitrogen collision partners [4]. The variations in reported broadening and shifting rates are significant. For example, the reported broadening by Xe differs by more than 30 MHz/Torr [12, 15]. Both blue and red shifts have been reported for He [21, 15]. The reported rates for molecular collision partners is rather limited and the rates for methane, ethane, and tetrafluoromethane, key DPAL collision partners, are not available. The rates for ^{3}He have been predicted, but not observed [15].

A summary of experimental observations regarding the broadening and shift rates for all the alkali atoms offers several trends: (1) the broadening rates for D_2 lines are normally slightly greater than D_1 line and (2) for blue shifts, the effect on the D_1 line is greater than the D_2 line [23]. The present work seeks to explore these trends for Cs by comparing the current results to our recent study of the D_1 lineshapes [46].

Experiment

The apparatus for this experiment is similar to our recent report on the Cs D_1 line [46]. The Coherent MBR-110 Ti:Sapphire ring laser was tuned to the wavelength of the D_2 transition, 852 nm, and scanned 32 GHz. A Fabry-Perot etalon, with a 300 MHz free spectral range and held at room temperature, monitored the frequency of the scanning ring laser. The free spectral range of the etalon was calibrated for every scan by employing a cesium reference cell. The ring laser provided up to 3 Watts with a linewidth less than 0.1 MHz and to avoid saturation broadening the

40

beam was heavily attenuated to $< 1\mu$W. A trifurcated fiber bundle was employed to transport the beam, and to randomize the polarization. One end of the fiber was focused through a 1 inch long low pressure cell that was temperature contolled to 313 K as a frequency reference. A second branch of the fiber transmitted the light through another identical cell at the same temperaure, where the pressure of the buffer gas was varied between 10 and 330 Torr. The final branch of the trifurcated fiber bundle monitored the incident laser power. The beam was amplitude modulated, at $\approx$1kHz, and detected with Hamamatsu PhotoDiodes coupled to Stanford Research SRS850 lock-in amplifiers. Pressure was monitored with MKS capacitance manometers with an accuracy of 0.08%.

Results

The hyperfine spectrum of the cesium D_2 transition is shown in Figure15 a, where the larger ground state splitting ($\approx$9.1926 GHz) is readily resolved. The Doppler width at T = 313K is 386 MHz and the hyperfine splitting of the $^2P_{\frac{3}{2}}$ ranges from 151 to 251 MHz and is not resolved [61]. Figure 15 b provides a simulation of the individual hyperfine structure of the F" = 3 components with a comparison to a low pressure data set. The lineshape profiles are broadened up to 6.32 GHz and shifted by as much as -2.08 GHz as the nitrogen is increased by 330 Torr. Each spectrum, which has an average signal to noise ratio of 700, was collected over 3 minutes and was sampled at over 100,000 spectral frequencies. The ground state splitting of the D_2 transition is evident at all pressures observed in this study. The ground state splitting therefore plays a significant role in the total lineshape of both the D_2 and D_1 transitions even for pressures of an atmosphere [43]. Similar spectra were recorded for each of the buffer gases in this study. A blue shift was observed for only the lightest collisional partners, He and ^{3}He. The lightest molecular collisional partners H_2, HD,

41

and D_2 induced a slight red shift, in contrast to the blue shifts observed previously for the D_1 transistion [46].

The full D_2 line is composed of six hyperfine components. The absorbance, A, is represented by a summation of Voigt profiles, V, for each component:

$$A = -ln\left(\frac{I}{I_0}\right) = c_0 + c_1\nu + c_2 \sum_{i=1}^{6} a_i V\left(\nu_i + \delta\nu, \Delta\nu_L; \Delta\nu_D\right), \qquad (25)$$

where

$\nu_i = $ line center frequency at zero pressure for the ith hyperfine component

$\delta\nu = $ collision induced shift common for all hyperfine components

$\Delta\nu_D = 386$ MHz = Doppler width (FWHM) contrained at T = 313K

$\Delta\nu_L = $ Lorentzian width (FWHM)

The absorbance measured from the ratio of the transmitted intensities, I, and the incident intensities, I_0. The absorbance is also defined as $A = \sigma l N$ where σ is the absorption cross-section, $l = 2.5cm$ is the cell path length, and n $\approx 2 \times 10^{11} cm^{-3}$ is the Cs number density. Due to the extremely small vapor pressure of cesium, the self-broadening and shifts are assumed to be negligible. A small baseline, associated with a slight linear background, is accounted for with the fit constants $c_o < 3.8 \times 10^{-3}$ and $c_1 < 1.44 \times 10^{-6} GHz^{-1}$. The values for the background are similar to those found for the D_1 spectrum [46]. The relative line strengths of the hyperfine components, a_i, are constrained to the lineshapes reported in Table 8. The parameters for numeric fit are limited to the collsion induced shift, the broadening rate, the absolute absorbance, c_2, and the small baseline.

Examples of the non-linear least-squares fit of equation (25) to three of the N_2
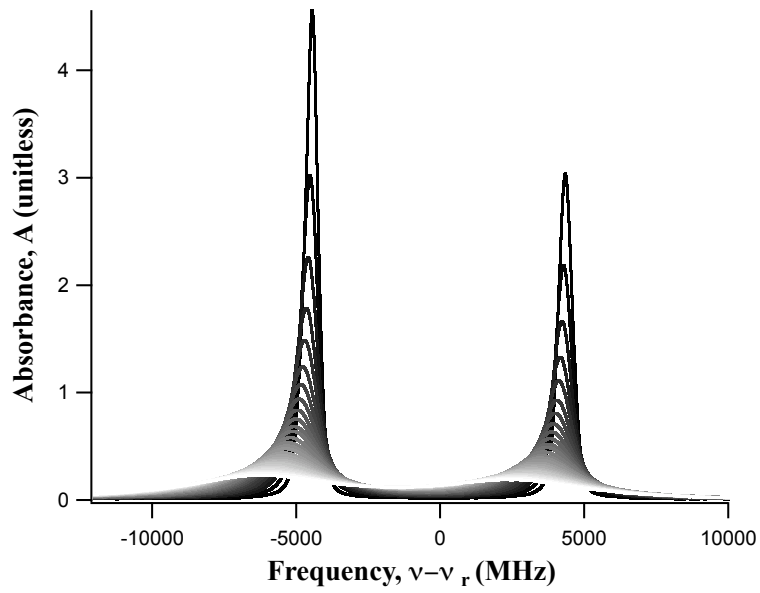
(a)
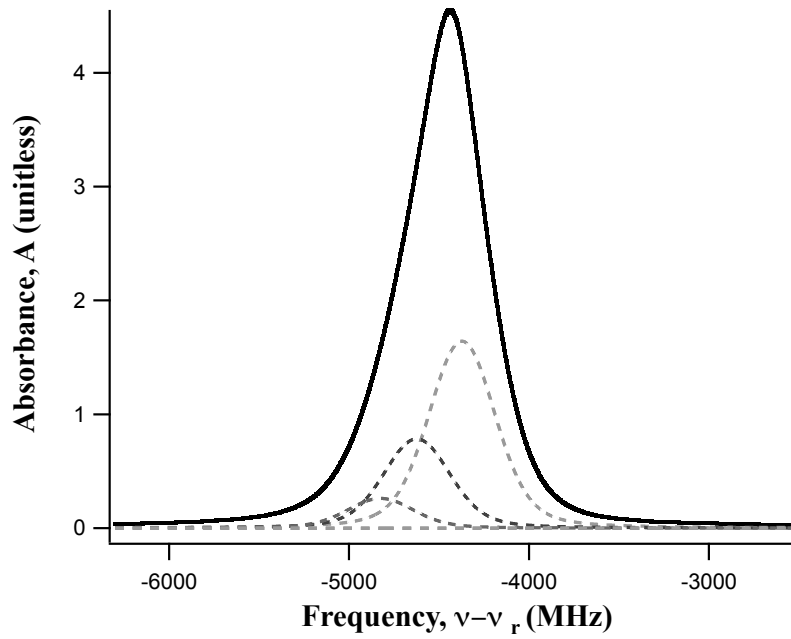
(b)

Figure 15. (a)The observed cesium D_2 lineshape pressure broadened by N_2 from 10-300 Torr and (b) simulation of components $F'' = 4$ to $F' = 3, 4, 5$ components with a set of data at low pressure.

43

Table 8. Cesium hyperfine transition strengths for the D_2 transition.

Transition $S_{F\ F'}$	Relative Line Strengths , a_i (unitless)
$S_{4\ 5}$	11/18
$S_{4\ 4}$	7/24
$S_{4\ 3}$	7/72
$S_{3\ 4}$	15/56
$S_{3\ 3}$	3/8
$S_{3\ 2}$	5/14

broadened spectra are shown in Figure 16. The fit residuals are $< 8.1\%$ across 55 Doppler widths, except in the core of the lineshape at low pressures. The structured residuals at low pressure fade as pressure was increased beyond 80 Torr. Similar results were observed in our recent report of the Cs D_1 line and attributed to line narrowing by velocity changing collisions[46]. This effect was first observed by Dicke in 1953 and was numerically characterized by Galatry [18, 19]. Neglecting this structure has a negligible effect on the Lorentzian widths and broadening rates[46, 49].

The Lorentzian width and shift for each spectrum are plotted against their corresponding pressure of buffer gas in Figs. 17 and 18. The widths and shifts depend linearly on pressure:

$$\Delta\nu_L = \gamma P + \gamma_N, \tag{26}$$

$$\delta\nu = \delta\ P, \tag{27}$$

where γ is the broadening rate for the buffer gas, and γ_N is the known natural width for the D_2 transition, 5.2 MHz [61]. The y-intercept of eqn. 26 and ?? were allowed to vary to account for minor variation of the manometer. The resultant broadening, γ, and shift rates, δ with their corresponding slope fit errors are shown in Table 9 and 10. The uncertainties were determined from the weighted least square
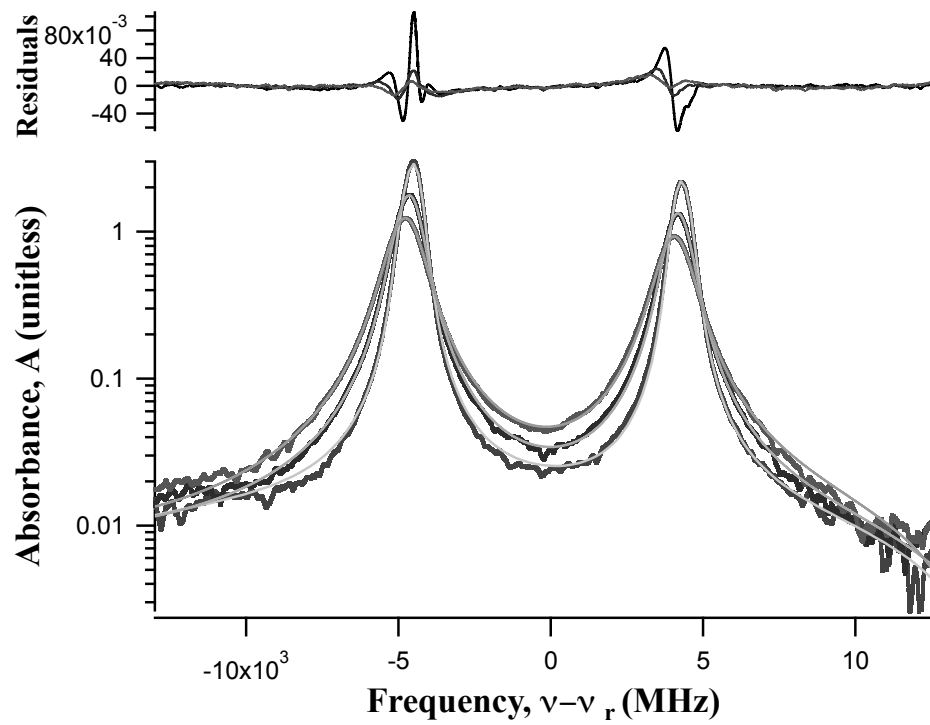
44

Figure 16. A sample of the resultant fits with residuals to equation (25) for the D_2 transition under the influence of N_2 at 20, 40 , 60, and 80 Torr.

fit and reported as one standard deviation in the slope parameter. In addition the pressure measurement of the capacitance manometer contributed an uncertainty of about 0.08%. This resulted in the total error of $\approx 0.30\%$.
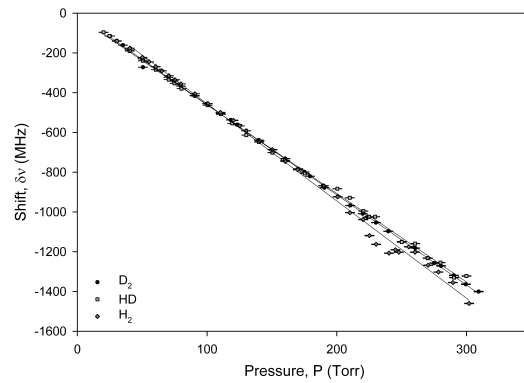
Table 9. Measured values for the broadening rate for the D_2 transition compared to the previous results.

| Current Work			Previous Work			
Buffer	γ_1[a,b]	$\frac{\gamma_{D_2}}{\gamma_{D_1}}$	$\mathbf{T_2}$	γ_2	γ_{adj}[c]	**Ref.**
Gas	**MHz/Torr**		**(K)**	**MHz/Torr**	**MHz/Torr**	
He	20.59±0.06	0.84	294	23.50±0.21	22.77	[4]
			293	24.65±0.26	23.84	[25]
			295	26.76±1.69	25.97	[12]
			393	17.73±0.75	19.87	[15]
^{3}He	22.35±0.05	0.84	393	23.37±1.132[d]	26.20	[15]
Ne	9.81±0.06	0.90	293	12.39±0.21	11.98	[25]
			295	10.34±1.05	10.04	[12]
Ar	16.47±0.18	0.90	293	19.91±0.54	19.26	[25]
			295	22.78±0.74	22.11	[12]
Kr	15.54±0.05	0.87	295	16.83±0.30	16.28	[25]
			295	10.94±0.90	10.62	[12]
Xe	18.41±0.07	0.93	295	17.22±0.14	16.66	[25]
			295	57.56±6.0	55.87	[12]
H_2	27.13±0.2	1.27	295	59.66±7.94	57.91	[12]
HD	28.24±0.17	1.39	—	—	—	—
D_2	22.84±0.16	1.26	—	—	—	—
N_2	19.18±0.06	1.20	294	22.68±0.20	21.98	[4]
			295	38.75±9.57	37.61	[12]
			393	23.39±1.51	26.21	[15]
CH_4	25.84±0.09	0.86	—	—	—	—
C_2H_6	26.14±0.08	0.95	—	—	—	—
CF_4	17.81±0.05	0.94	—	—	—	—

[a] Error from a weighted linear fit only. [b] T_1=313K [c] See Eqn. (28) [d] Calculated value from ^{4}He.
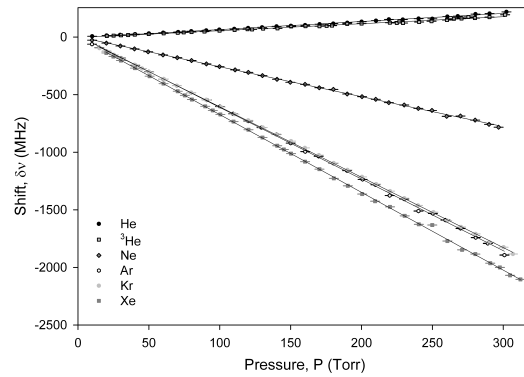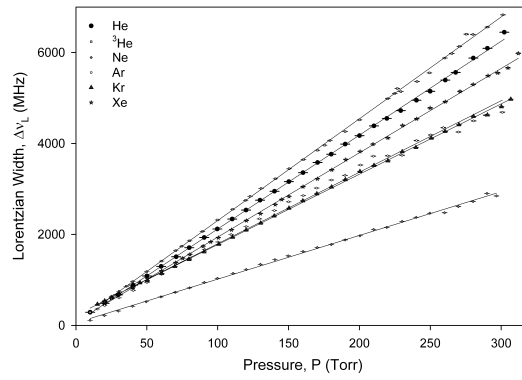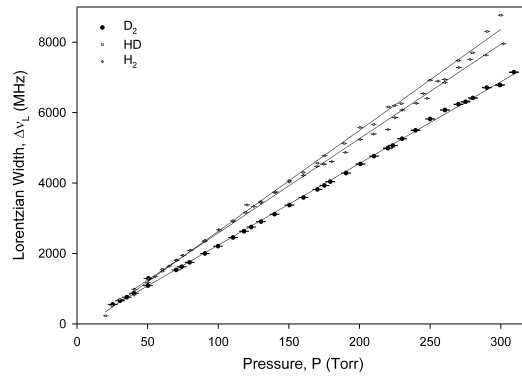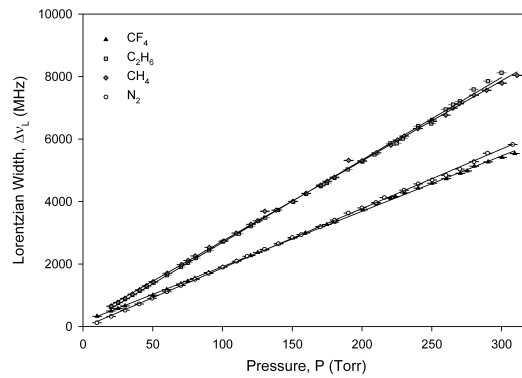
(a)

(b)
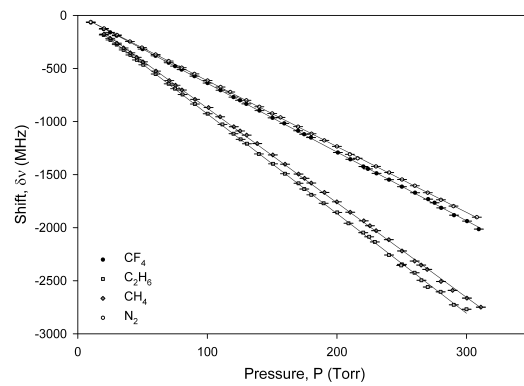
(c)

Figure 17. Cesium D_2 hyperfine profile shift as a function of pressure of (a) the noble gases, (b) various hydrogen isotopes, and (c) several molecules.

(a)

(b)

(c)

Figure 18. Cesium D_2 hyperfine profile broadening as a function of pressure of (a) the noble gases, (b) various hydrogen isotopes, and (c) several molecules.

48

Table 10. Measured values for the shift rates for the D_2 transition compared to the previous results.

	Current Work		Previous Work		
Buffer	$\delta^{\text{a,b}}$	$\frac{\delta_{D_2}}{\delta_{D_1}}$	$\mathbf{T}_2$	δ	**Ref.**
Gas	**(MHz/Torr)**		**(K)**	**(MHz/Torr)**	
He	0.69±0.01	0.16	294	0.75±0.01	[4]
			293	0.68±0.03	[25]
			295	3.88±1.68	[12]
			393	-1.40±.08	[15]
^{3}He	0.60±0.01	0.10	393	-1.85±0.11$^{\text{c}}$	[15]
Ne	-2.58±0.01	1.61	293	-2.59±0.07	[25]
			295	-4.65±0.30	[12]
Ar	-6.18±0.02	0.96	293	-6.53±0.16	[25]
			295	-7.65±0.75	[12]
Kr	-6.09±0.01	1.12	293	-6.44±0.10	[25]
			295	-7.79±1.05	[12]
Xe	-6.75±0.01	1.05	293	-6.44±0.1	[25]
			293	-13.34±0.75	[12]
H_2	-4.83±0.04	-4.25	295	1.65±0.30	[12]
HD	-4.49±0.03	-9.48	—	—	—
D_2	-4.54±0.03	-5004	—	—	—
N_2	-6.2±0.01	0.80	294	-6.73±0.04	[4]
			295	-7.13±0.24	[12]
			393	-6.79±0.38	[15]
CH_4	-8.86±0.02	0.93	—	—	—
C_2H_6	-9.38±0.02	1.07	—	—	—
CF_4	-6.47±0.01	1.06	—	—	—

$^{\text{a}}$ Error from a weighted linear fit only. $^{\text{b}}$ T_1=313K $^{\text{c}}$ Calculated value from ^{4}He.

49

Discussion

The present results are compared with previous measurement in Tables 9 and 10. Prior studies were conducted at temperatures of $T_2 = 293$-393 K and the rates must be scaled to $T_1 = 313$ K for the present results. The temperature dependence of broadening rates are usually described as [29]:

$$\gamma(T_2) = \gamma(T_1) \left(\frac{T_1}{T_2} \right)^n . \tag{28}$$

If the cross-section, σ, is independent of relative speed:

$$\gamma(T) = \sigma \left(\frac{8 k_b T}{\pi \mu} \right)^{1/2} , \tag{29}$$

then n $= \frac{1}{2}$ [46]. The relative speed, $g = \left(\frac{8 k_b T}{\pi \mu} \right)^{1/2}$, depends on the reduced mass of the collision pair, μ. The temperature dependence of the cross-section was very weak for Cs D_1 and is assumed independent for the comparisons presented in Tables 9 and 10 [46]. For He, the present broadening results compare most favorably with the most recent result using broadband illumination and a grating spectrometer and not as closely with the similar laser absorption spectroscopy work [15, 4]. The discrepancies between this work and that of Andalkar et al, could lie in the differences in the experimental procedures [4]. First, the prior work was limited to pressures under 160 Torr and only acquired under 16 data points for the calculation of the broadening rate. On the other hand, this work acquired data out to 300 Torr and had twice the number of data points. Secondly, in the calculation of the slope Andalkar et al adjusted the widths by their laser linewidth and the natural width of the D_2 line in order to fit a line with a y-intercept of zero. In contrast, due to small variations in the zeroing of the capacitance manometer between buffer gases this work allowed the

50

y-intercept to vary allowing the slope to be fit more precisely. Finally, the fitting of the line by Andalkar et al was a general least squared fit but this work utilized the error of the Lorentzian width determined from the fitting of eqn. 25 to provide a relative wieghting of the data and perform weighted least squared fit.

For the remainder of the rare gases, our results tend to favor the recent results using laser absorption techniques [25]. For Xe, N_2, and H_2 our results are 2-3 times smaller than the older work using scanning Fabry-Perot spectrometers [12]. Similar comparisons are observed for the shifting rates, with the notable exception of He. Our results agree with the small blue shift observed by Andalkar et al and Inoue et al and disagree with the larger blue shift of Bernabeu and Alvarez and the anomalous red shift of Couture et al [4, 25, 12, 15]. In the case of the red shift of Couture et al, this may be due to the extremely high temperatures of their study and the energy dependence of the shift cross-sections. We also observe a blue shift of H_2 in disagreement with the Fabry-Perot results [12].

A comparison of the broadening and shifting of the D_1 and D_2 lines for Na, K, Rb, and Cs by a variety of collision partners is summarized in Figure 19 [29, 34, 51, 46]. In general, the rates are similar for the two spin-orbit split states. For Cs collisions with rare gases and large molecules the D_2 broadening rate is 5-16% less than the D_1 rate. In contrast, Hindmarsh and Farr observed a slightly higher value for the D_1 lines when reviewing the full alkali database in 1972 [23]. This conclusion is not supported when reviewing the more recent alkali results.

Hindmarsh and Farr offer several additional observations regarding the shifting rates. First, the difference in the shift is dependent on the perturber and not on the nature of the alkali. This trend is supported by the data in Figure 19. For example, the noble gases show that as the mass of the perturber is increased the shift switches direction and increases in magnitude. For the small number of molecules shown, no

51

observable correlation is shown. Second, where there is a blue shift of the transition, the $^2P_{\frac{1}{2}}$ rate is greater than the $^2P_{\frac{3}{2}}$ rate. This is observed in Cs and Rb when mixed with He and ^{3}He. The collisional partner H_2, HD, and D_2 switch the direction they shift from blue to red when comparing $^2P_{\frac{1}{2}}$ to $^2P_{\frac{3}{2}}$. Third, the red shifts are typically small and there is no way to predict which transition will have the greater shift from any observable trend within the data. This statement is observed in Figure 19 b. While there are more rates that are greater for $^2P_{\frac{3}{2}}$ there are still some that are greater for $^2P_{\frac{1}{2}}$.

A comparison of the effect of the alkali on the broadening cross-section for the D_2 line is shown Figure 20. Each alkali shows a linear relationship between itself and that of cesium, but each has a different slope. The cross-sections for Cs and Rb are similar. However, the cross-sections for K are about 70% larger and for Na is about 30% less. Further study of the potential surfaces is required to explain the observed trends.

To further compare these rates, the Leonard-Jones interatomic potentials were calculated using the the approach demonstrated by Hindmarsh and Farr and utilized by Rotondaro and Perram.[23, 51] This approach assumes a 6-12 difference potential:

$$V(R) = C_{12}r^{-12} - C_6 r^{-6}, \tag{30}$$

where r is the interatomic separation and C_6 and C_{12} are the coefficients for the r^{-6} and r^{-12} terms respectively. These coefficients were determined from the broadening and shift rates using the impact approximation [54]. The impact approximation, while sufficient within the core of the Lorentzian profile, is inadequate in the far wings. In addition, these potentials average over all angles of impact and assume a single point of interaction between the alkali and the molecule. These interatomic difference potentials are shown in Figure 21.
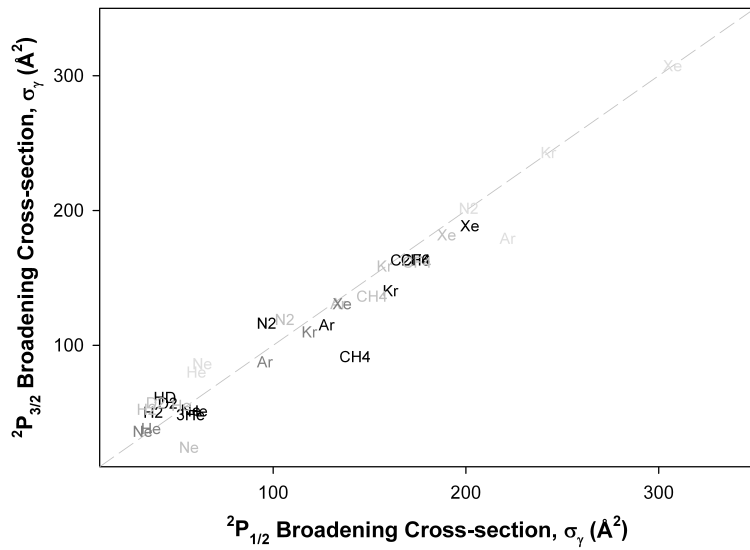
(a)
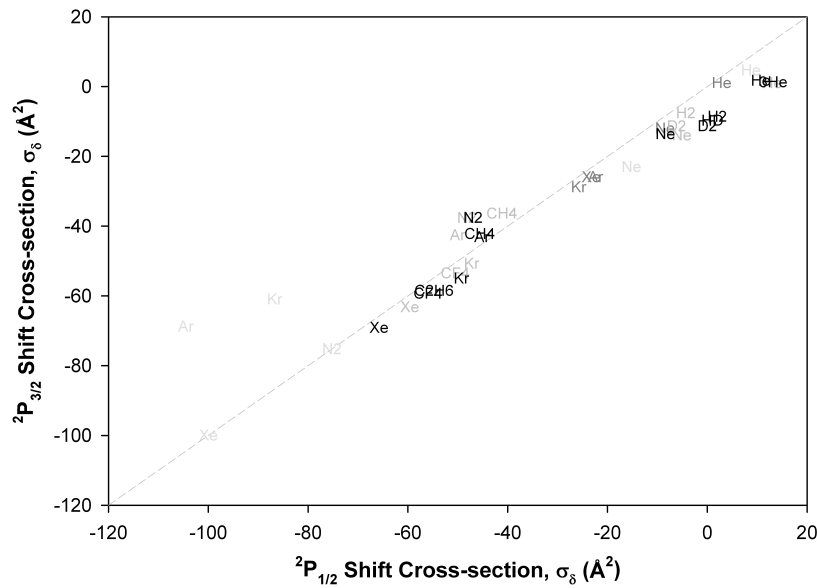
(b)

Figure 19. The collisional broadening (a) and shift (b) cross-section for the alkalis Cs (■), Rb (■), K (■), and Na (■) with various collisional partners for D_2 transition compared to the D_1. The rates were measured for sodium by Kielkopf, for potassium by Lwin and McCartan, for rubidium by Rotondaro and Perram, and cesium by Pitz et al. [29, 34, 51, 46]
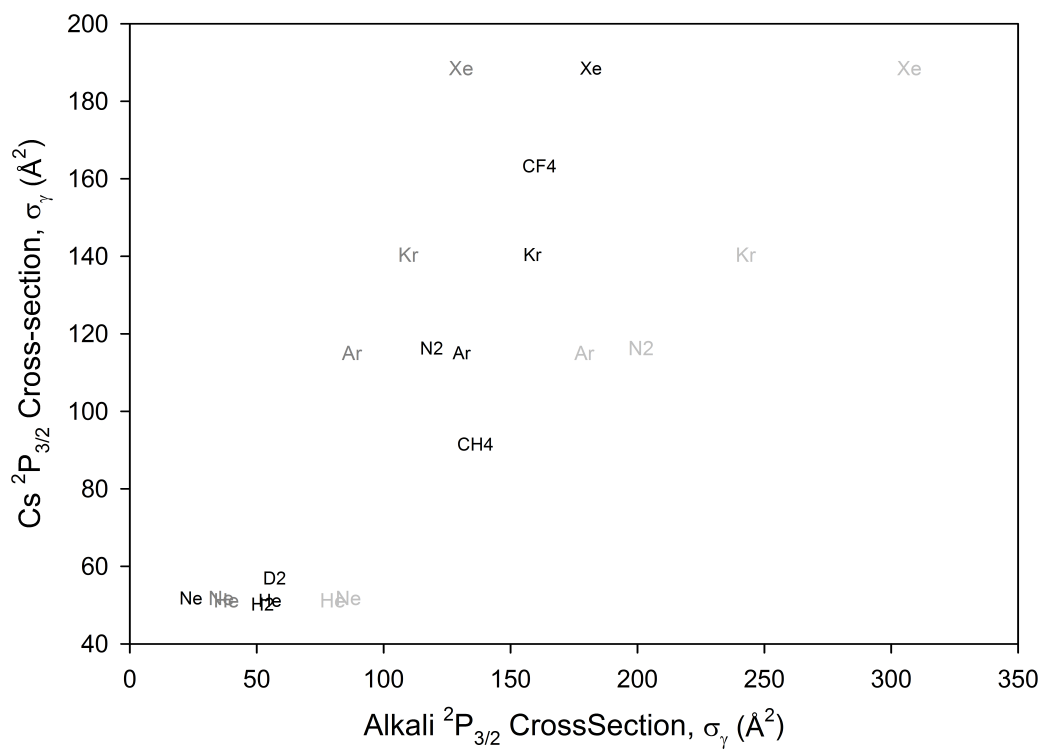
53

Figure 20. Comparison between the $^2P_{\frac{3}{2}}$ broadening cross-sections of Na, K, and Rb with that of Cs.

Theoretical calculations of the ground state potential energy surface for alkali-rare gas collision pairs, $X^2\Sigma$, and the excited states, $A^2\Pi_{1/2}$ correlating to the separate $^2P_{1/2}$ atom and the $A^2\Pi_{3/2}$, $B^2\Sigma$ states correlating to the $^2P_{3/2}$, have been performed at various levels [13, 39]. A comparison of these theoretical results to the interatomic difference potentials produced by the Hindmarsh and Farr techniques may show some striking differences. First, the excited state $^2P_{3/2}$ has been shown, by theoretical means, to split into two potential surfaces, $A^2\Pi_{3/2}$ and $B^2\Sigma$. This is not possible to produce both a repulsive and bound surface with the Hindmarsh and Farr technique. Second, the quantitative values for the well depth and equilibrium interatomic separation distance are not similar between the two sets of potential surfaces. In the case of cesium-argon potential surfaces the theoretical values for the well depth are on the order of 60 meV, while the Hindmarsh and Farr surfaces are less than 0.1 meV [39]. In addition, the equilibrium interatomic separation for the theoretical surfaces is three times smaller than those obtained for this work [39]. While these surfaces do not compare directly, if the Hindmarsh and Farr techniques is applied to other alkalis the interatomic difference potentials that are obtained can be used to form additional correlations between alkalis.

The equilibrium interatomic separation distance, R_e and the well depth, D_e if they are bound surfaces, for the Cs D_1 and D_2 data are shown in Figure 22. Well depth and equilibrium separation generally increase as the polarizability of the rare gas increase. Molecular hydrogen exhibits the strongest binding. The larger molecules behave similar to the heavier rare gases. Nitrogen has a similar spin orbit relaxation rate compared to the other diatomic molecules studied here, but the quenching rate is eleven times greater than H_2, HD, and D_2 [37]. This quenching rate for nitrogen is of the same order of magnitude for both the D_2 and D_1 transitions [37]. The values R_e and D_e for the cesium $^2P_{\frac{3}{2}}$ are also compared to the rubidium values calculated
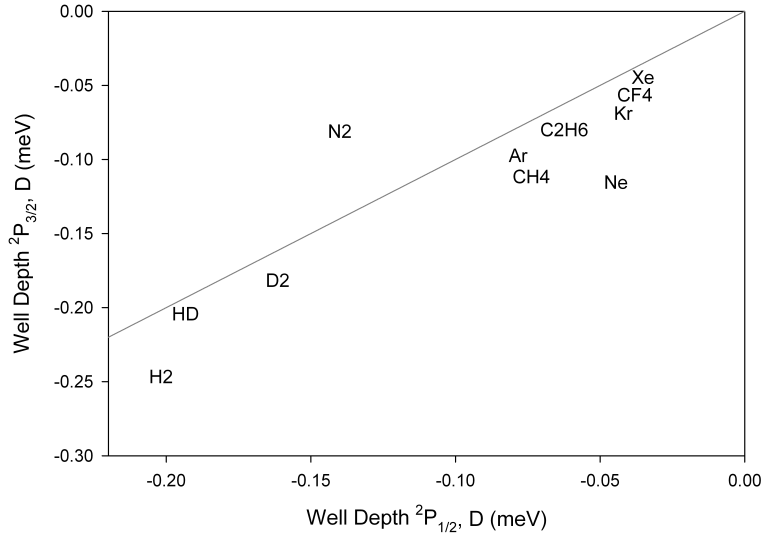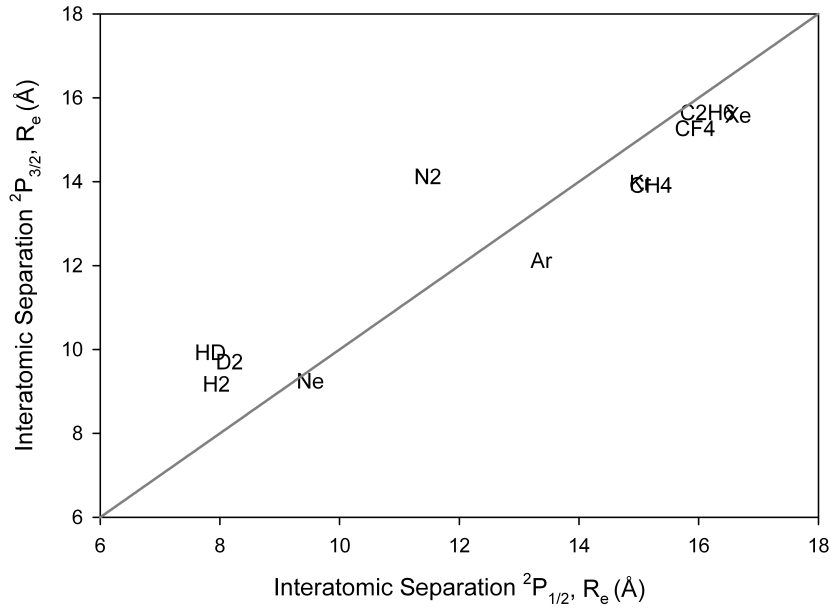
55
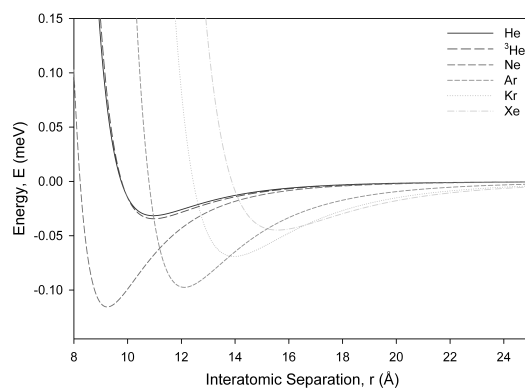
(a)
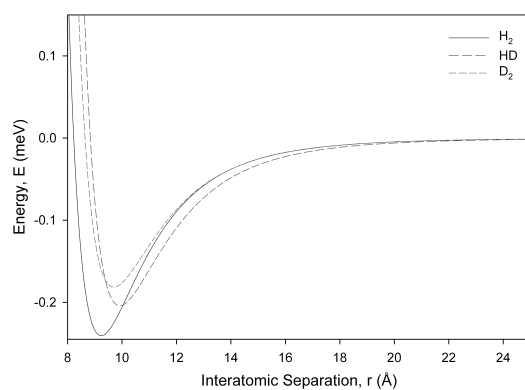
(b)
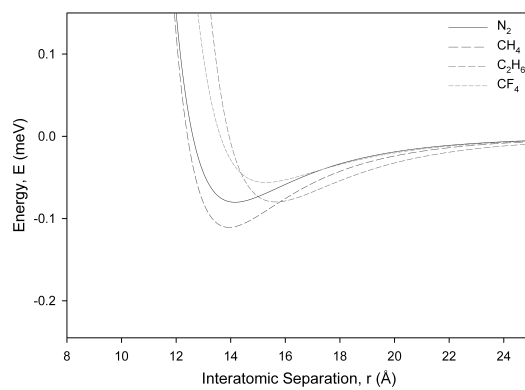
(c)

Figure 21. The interatomic potential surfaces between cesium and (a) the noble gases, (b) various forms of hydrogen, and (c) an assortment of molecules.

(a)

(b)

Figure 22. Comparison between the well depths (a) and the interatomic separation (b) of cesium D_1 and D_2 transitions.

by Rotondaro and Perram, shown in Figure 23 [51]. The values for D_e and R_e are strongly correlated between the two atoms with nitogen being the largest outlier for both the well depth plot and the equilibrium separation.

The impact approximation and the Leonard-Jones potential suggests a correlation between the probability per collision for phase changing collisions and polarizability. This present result is consistent with this prediction, as illustrated in Figure 24. The ratio for the gas kinetic cross-section:

$$\sigma_g = \pi \cdot \left(r_{Cs} + r_{\text{buffer gas}}\right)^2, \tag{31}$$

were evaluated from reference [24]. The polarizability for the buffer gases was found in reference [5].

Conclusions

The rates for collision induced broadening and shifting in the core of the Lorentzian profile for the Cs D_2 line with a broad range of collision partners at modest pressures has been determined with uncertainties of $\approx 0.3\%$. A number of trends in the broader alkali database have been evaluated, but require further theoretical support for further interpretation. Sub-atmospheric pressures are sufficient to broaden the pump transition for the Cs Diode Pumped Alkali Laser if diode bars and stacks can be narrowed to ≈ 30 GHz, as recent reports suggest [65]. The current addition of lineshape data for ^{3}He, methane, and ethane allow detailed modeling of the bleached wave in recent laser demonstrations [8].
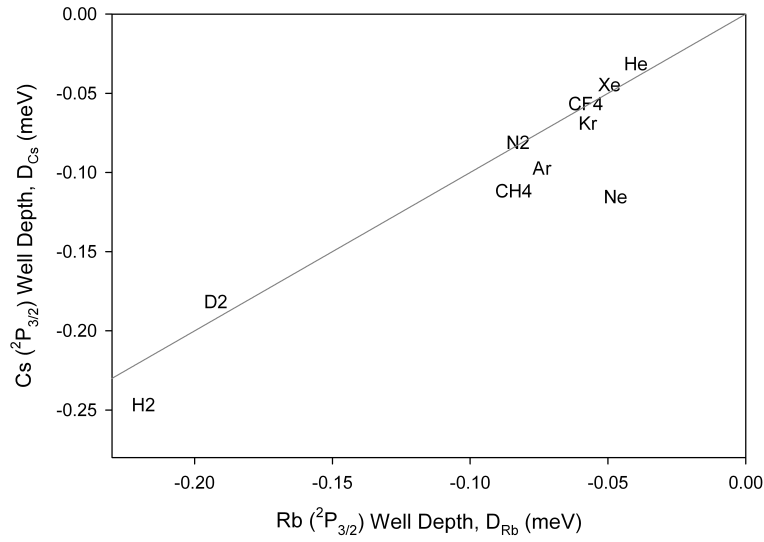
(a)
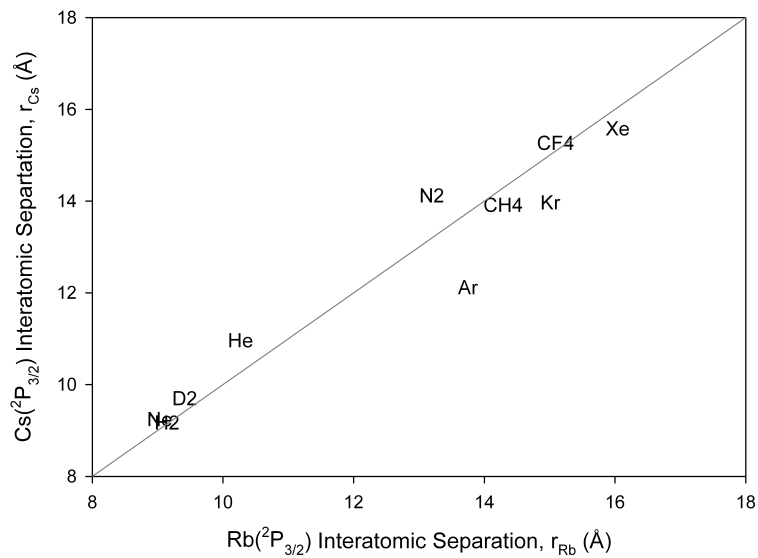
(b)

Figure 23. Comparison between the well depths (a) and the interatomic separation (b) of cesium and rubidium.
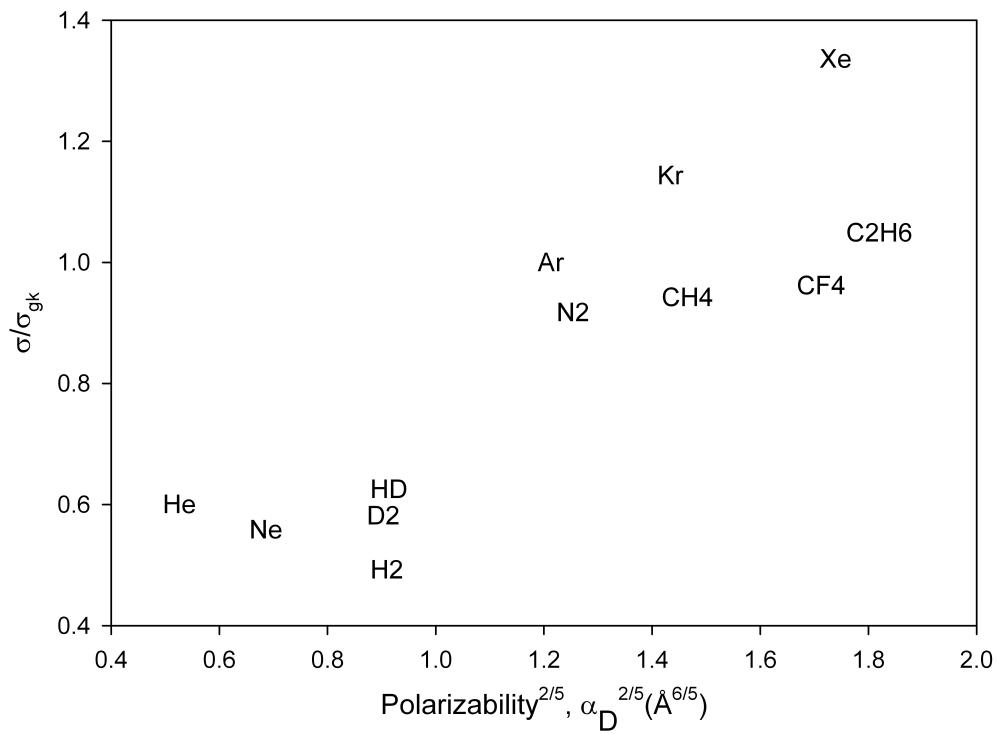
Figure 24. Correlation of the probability for phase changing collisions in the D_2 transition with dipole polarizability of the collision partner.

V. Spin-Orbit Energy Transfer

Introduction

Collision induced mixing between the ^2P_J states of alkali's have been studied thoroughly since the 1960s.[31, 20, 16, 36, 37, 17, 67, 68, 52] These mixing rates have again become of keen interest because of their role in Diode Pumped Alkali Lasers (DPAL). The DPAL system was first demonstrated by Krupke and Beach.[32, 8] This alkali laser can be consider an adaptation of the laser system proposed in 1958 by Schawlow and Townes.[55] The DPAL system is a three level laser system that is pumped by diode bars or stacks along the D_2 transition to its $^2P_{\frac{3}{2}}$ state then collisionally relaxed to the $^2P_{\frac{1}{2}}$ state where it lases down the D_1 transition. Recent demonstrations have employed ethane and methane as the collisional partner for spin-orbit relaxation. While ethane has an excellent rate for energy transfer, it also degrades laser performance with the production of laser snow and soot.[41, 69] Hydrocarbon free lasers have recently been demonstrated for both potassium and rubidium using rare gas collision partners.[74] For cesium, the larger spin-orbit splitting requires molecular collision partners.[69]

The most recent study of the mixing rate between the cesium $6^2P_{1/2} \leftrightarrow 6^2P_{3/2}$ states was performed in 1974 by Walentynowicz.[67, 68] In this investigation a cesium discharge lamp was used to excite the desired states in cesium and a pair of photomultiplier tubes to monitor the flourescence of the two mixing states. In addition, Walentynowicz assumed quenching was negligible and observed the resulting intensities at several different pressures of no more than 1.5 Torr.

In this present work, the spin-orbit mixing rate between the $6^2P_{\frac{3}{2}}$ and the $6^2P_{\frac{1}{2}}$ levels of cesium caused by collision with N_2, H_2, HD, D_2, CH_4, CF_4, C_2H_6, and C_2F_6 over a range of 0-100 Torr are observed. The role of the energy defect between cesium

61

and the ro-vibrational model of the collision partner is examined and compared with the prior results for rubidium.[53] In addition, the energy defect between cesium and the lowest lying vibrational states of the collisional partners is also compared.

Experiment

The apparatus used to measure the spin orbit energy transfer between the $6^2P_{\frac{3}{2}}$ and the $6^2P_{\frac{1}{2}}$ states is shown in Figure 25. A Coherent MBR-110 Ti:Sapphire ring laser was tuned to either 852 or 894 nm to prepare the $6^2P_{\frac{3}{2}}$ or the $6^2P_{\frac{1}{2}}$ states, respectively. The ring laser, which was pumped by a Coherent Verdi V-18 diode laser, has a linewidth less than 100 kHz with powers less than 3.5 W. The hyperfine splitting of the ground $^2S_{\frac{1}{2}}$ state is 9.1926317 GHz and the laser was tuned to excite the ($F'' = 4$) component, at frequencies of $\nu_1 = 335111$ GHz and $\nu_2 = 351722$ GHz. These frequencies were actively monitored with a Bristol 621 laser wavelength meter to minimize laser drifting.

This beam was greatly attenuated ($< 4\mu W$), expanded to a diameter of 9.7mm, and amplitude modulated before reaching the test cell. The resulting pump intensities were less than 5 $\frac{\mu W}{cm^2}$, significantly less than the saturation intensity. At low pressure the saturation intensity of the D_1 transition is approximately 2.5 $\frac{mW}{cm^2}$. Phase sensitives with amplitude modulation at 100 Hz detection was employed to improve the signal to noise ratio.

The cell was described in detail previously and could sufficiently maintain and vary the cell temperature and pressure.[46] The single end of a bifurcated fiber bundle was placed perpendicular to the beam to observe the side flourescence of the cell and was coupled into a pair of Hamamatsu photomultiplier tubes (R5509). Two ThorLabs band pass filters centered on the D_1 ($\lambda = 890$nm with a full width half max (FWHM) of 10 nm) and D_2 ($\lambda = 850$nm with a FWHM of 10 nm) transitions to
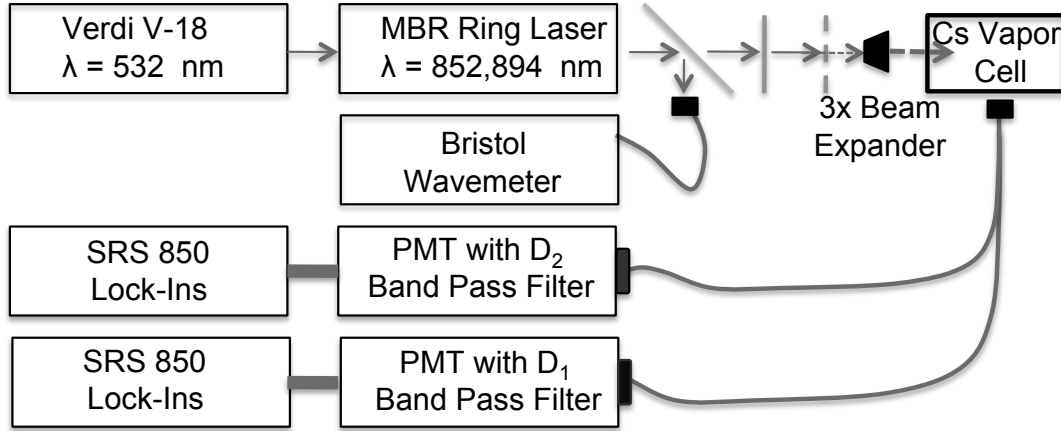
Figure 25. Experimental apparatus to observe side fluorescence of cesium.

limit the detection of light to the two desired states. This allows for the monitoring of the laser prepared state and the collisionally populated satellite state simultaneously while continuously varying the pressure of buffer gas. Cell pressure was monitored by MKS model 690A capacitance manometer with a range of 0-100 Torr. The cesium was 99.98% pure and all gases had a purity greater than 99.9% purity, with the one exception of HD which had a purity of 97.3%. The cell was maintained at room temperature, which resulted in a cesium vapor pressure of 1.51×10^{-6} Torr, to avoid optical trapping.

A small amount of scattered laser light which was coupled into the PMTs. The level of the scattered light was measured by tuning slightly off resonance from the pump line while the cell contained no buffer gas. The scattered laser light was recorded to be less than 2% of the emission of the prepared state and was subtracted from the total observed signal. Additionally, the band pass filter did not completely isolate the emission of the satellite state from the parent. The fraction of light passed by the satellite filter at the pump wavelength was measured at zero buffer gas pressure, where no collisional transfer exists, at less than 1%.

The relative spectral response of the D_1 and D_2 detectors is required to relate the

63

observed intensities to the corresponding concentrations of the emitting states:

$$I_{D_1} = \left[Cs\left(^2P_{1/2}\right)\right] d_1 = N_1 d_1, \tag{32}$$

$$I_{D_2} = \left[Cs\left(^2P_{3/2}\right)\right] d_2 = N_2 d_2, \tag{33}$$

The relative spectral response was initially determined by a blackbody calibration at $T = 900\ C$ as $d = \frac{d_1}{d_2} = 0.431 \pm 0.07$. The improved value for spectral response, $d = 0.979 \pm 0.186$, was achieved by assessing the resulting rates with respect to the principle of detailed balance, to be discussed below.

Results

The observed intensities from the D_1 and D_2 transitions converted to concentrations N_1 and N_2, as the ethane or methane gas pressure is continuously increased as shown in Figure 26. The ethane data in Figure 26a were obtained during a period of less than 20 minutes while the pressure increased at an average rate of 80 mT/s, yielding greater than 25,000 samples. The methane data is more highly sampled at 124,000 samples over the 100 Torr range.

The signal for the satellite state initially increases linearly due to direct energy transfer. At higher pressures, collisional transfer back to the parent state begins to limit the satellite concentration and the ratio approaches a nearly statistical distribution.

In order to determine the rate of energy transfer from the observed intensity ratio, the following kinetic analysis is developed. First, laser excitation is used to populated either the $^2P_{\frac{1}{2}}$ or the $^2P_{\frac{3}{2}}$ via:

$$Cs[^2S_{\frac{1}{2}}] + h\nu_1 \rightarrow Cs[^2P_{\frac{1}{2}}] \tag{34}$$

or

$$Cs[^2S_{\frac{1}{2}}] + h\nu_2 \rightarrow Cs[^2P_{\frac{3}{2}}], \tag{35}$$
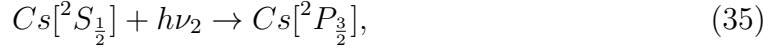
where the rates, S_1 and S_2, depend on the absorption cross-section and the laser intensity. Second, the energy of the excited states is then transferred by collisions with the buffer gas, M:

$$Cs[^2P_{\frac{1}{2}}] + M \rightleftharpoons Cs[^2P_{\frac{3}{2}}] + M, \tag{36}$$
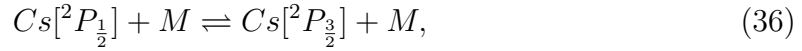
with rate coeffcients k_{12} and k_{21} to be determined in this work. Third, population of the excited state may return to the ground state via quenching or spontaneous emission:

$$Cs[^2P_{\frac{1}{2}}] + M \rightarrow Cs[^2S_{\frac{1}{2}}] + M \tag{37}$$

$$Cs[^2P_{\frac{3}{2}}] + M \rightarrow Cs[^2S_{\frac{1}{2}}] + M \tag{38}$$

$$Cs[^2P_{\frac{1}{2}}] \rightarrow Cs[^2S_{\frac{1}{2}}] + h\nu_1 \tag{39}$$

$$Cs[^2P_{\frac{3}{2}}] \rightarrow Cs[^2S_{\frac{1}{2}}] + h\nu_2 \tag{40}$$
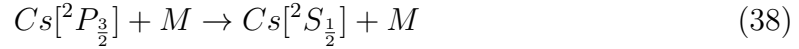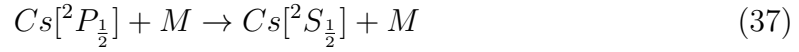
The quenching rates, k_{Q1} and k_{Q2}, depend slightly on the excited state. The radiative rates are $A_1 = 28.66\ MHz$ and $A_2 = 32.82\ MHz$.[61]

A steady-state analysis of the rate equations establishes the ratio of concentrations as:

$$\left[\frac{N_1}{N_2}\right]_{\text{Pump } D_2} = \left(\frac{I_{D_1}}{I_{D_2}}\right)\left(\frac{d_1}{d_2}\right) = \frac{k_{12}[M]}{A_1 + (k_{Q1} + k_{21})[M]} \tag{41}$$

$$\left[\frac{N_2}{N_1}\right]_{\text{Pump } D_1} = \left(\frac{I_{D_2}}{I_{D_1}}\right)\left(\frac{d_2}{d_1}\right) = \frac{k_{21}[M]}{A_2 + (k_{Q2} + k_{12})[M]}. \tag{42}$$

when pumping the D_2 and D_1 transitions, respectively.

Least squares fits of eqns. 41 and 42 to the observed population ratios are shown in

65
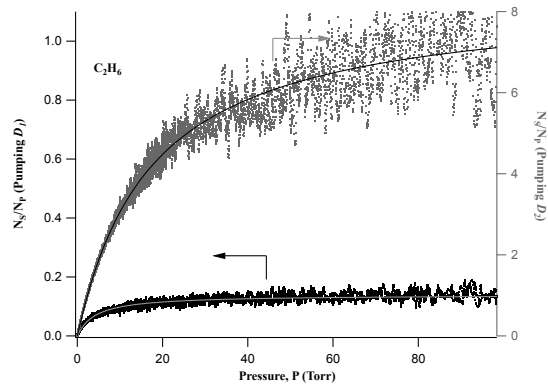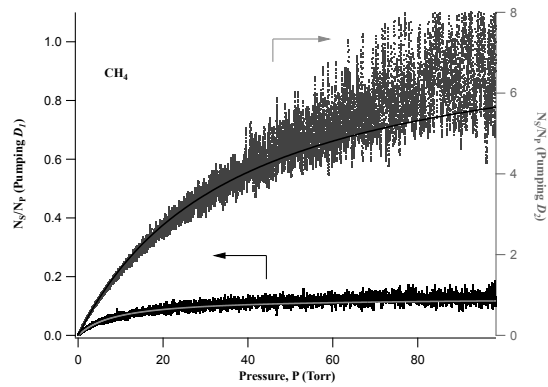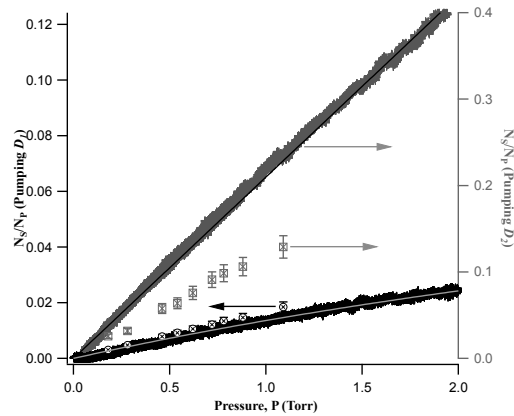
Figure 26. Population ratios while preparing both the $^2P_{3/2}$ and $^2P_{1/2}$ state with varying pressure of (a) ethane and (b) methane. An expanded view of the methane data at low pressures is compared with the prior work at 440K(c).[67]

66

Figure 26. The resulting fit parameters are reported as the spin-orbit and quenching cross-sections in Table 11. The average relative speed:

$$g = \frac{8k_bT}{\pi\mu} \tag{43}$$

where μ is the reduced mass of the collision pair is used to relate the rate to the cross-sections, $k = \sigma g$, at the cell temperature of $T = 298K$. The error bounds reported in Table 11 reflect only the statistical errors as determined by one standard deviation in the corresponding fit parameter.

The ratio of the forward and the reverse spin-orbit rates must obey the principle of detailed balance:

$$\frac{\sigma_{21}}{\sigma_{12}} = \frac{g_2}{g_1}e^{\frac{-\Delta E_{so}}{k_bT}} \tag{44}$$

where the degeneracies are $g_2 = 4$ and $g_1 = 2$ and the spin-orbit splitting is $\Delta E_{so} = 554cm^{-1}$. Constraining the average value for this ratio for all collision partners to $\frac{\sigma_{21}}{\sigma_{12}} = 0.132$ at T=298K. provides an improved measure of the relative detectivity, $\frac{d_1}{d_2} = 0.979 \pm 0.186$. The observed ratios $\frac{\sigma_{21}}{\sigma_{12}}$ range between 0.12-0.16, suggesting a systematic error of about 15%. Note that the prior determination of the spin-orbit relaxation rates exhibit significantly greater violations of detail balance.

The curvature observed in Figure 26 at higher pressures reflect the combined contributions of the reverse spin-orbit rate and quenching rate, as expressed in the denominator of eqns. 41 and 42. Any difference between the high pressure asymptotic limit and the ratio of eqns. 41 and 42 implies a significant quenching rate. These expected asymptotic values for the population ratios in this quantity are illustrated in Fig 26, and little quenching is observed for methane and ethane.

Table 11. Cross-sections for the energy transfer from the $^2P_{3/2}$ to the $^2P_{1/2}$ levels of cesium induced by collisions at 298 K.

Collisional Partner	Cross-section $\sigma_{12}(\text{Å}^2)$	Cross-section $\sigma_{21}(\text{Å}^2)$	Ratio σ_{21}/σ_{12}	Temp. (K)	Ref.
N_2	19.86±0.03	2.34±0.01	12.60±0.82%	298	This Work
	16.2±2	3.6±.5	22±4%	313	[36]
	25.0±2.5	4.7±.5	19±2.7%	315	[37]
H_2	31.10±0.04	4.43±0.01	13.87±0.91 %	298	This Work
	29.6±4.4	6.5±1	22±5%	313	[36]
	44±4.4	6.7±.5	15.2±1.9%	315	[37]
	25.8±2.58	3.6±.4	14.0±2.1%	300	[68]
HD	30.01±0.05	4.09±0.01	14.52±0.95 %	298	This Work
	32±3.2	4.8±.5	15.0±2.2%	315	[37]
	22.5±2.25	3.9±.4	17.3±2.5%	300	[68]
D_2	22.69±0.02	3.02±0.01	14.2±0.93 %	298	This Work
	28±2.8	4.2±.4	15.0±2.1%	315	[37]
	16.4±1.6	2.3±.2	14.0±1.6%	300	[68]
CH_4	21.36±0.01	2.95±0.01	14.74±0.96 %	298	This Work
	16.8±1.7	2.3±.2	13.7±1.83%	298	[67]
CF_4	60.34±0.06	9.93±0.01	15.97±1.04%	298	This Work
	52.0±5.2	7.9±.8	15.2±2.2%	310	[67]
C_2H_6	64.83±0.08	7.78±0.01	12.80±0.84%	298	This Work
	57.5±5.8	7.9±.8	13.7±2.0%	298	[68]
C_2F_6	130.66±0.08	16.47±0.01	12.6±0.84%	298	This Work

68

Discussion

The energy exchange rates are usually at their maximum when they have a resonant path for that exchange. Gallagher implied the possibility of electronic to translational energy exchange with cesium-rare gas collisions. It is important to note that a similar temperature dependence of the cesium-rare gas energy transfer is not observed in the complex molecule of Walentynowicz.[67, 68] This may imply that the complex molecules transfer the energy by other means.

Rotondaro suggested the possibility for accessing the rotational states of the buffer gas for the exchange of energy.[52] Rotondaro used rubidium which has an energy defect of 237.6 cm^{-1}. On the other hand, Cesium has a energy defect of 554 cm^{-1} which may be able to access some of the lower vibrational states of the more complex molecules. Rotondaro used the general reaction model:

$$A[^2P_{\frac{3}{2}}] + M(J'') \rightleftharpoons A[^2P_{\frac{1}{2}}] + M(J'), \tag{45}$$
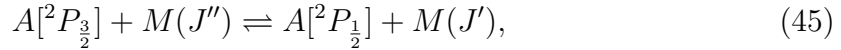
where $A[^2P_{\frac{x}{2}}]$ is the concentration of the alkali and $M(J)$ is the concentration of the buffer gas at rotational level J. He demonstrated a correlation was shown between Rb and the total energy defect of the rotating buffer gas[52]. Figure 27 a was recreated from his results with the addition of cesium. The correlation expressed by Rotondaro utilized the model:

$$k_{E-R} = \sum_J e^{-|\Delta E|/k_b T} \frac{hcB_\nu}{k_b T} (2J + 1) e^{-hcB_\nu J(J+1)/k_b T}, \tag{46}$$

where k_{E-R} is the electronic to rotational energy exchange rate, ΔE is the differece on the alkali energy defect from the rotational energy defect, B_ν is the rotational constant, and J is the rotational states.

As one can see, the rubidium correlation seems to fit nicely and the cesium

69
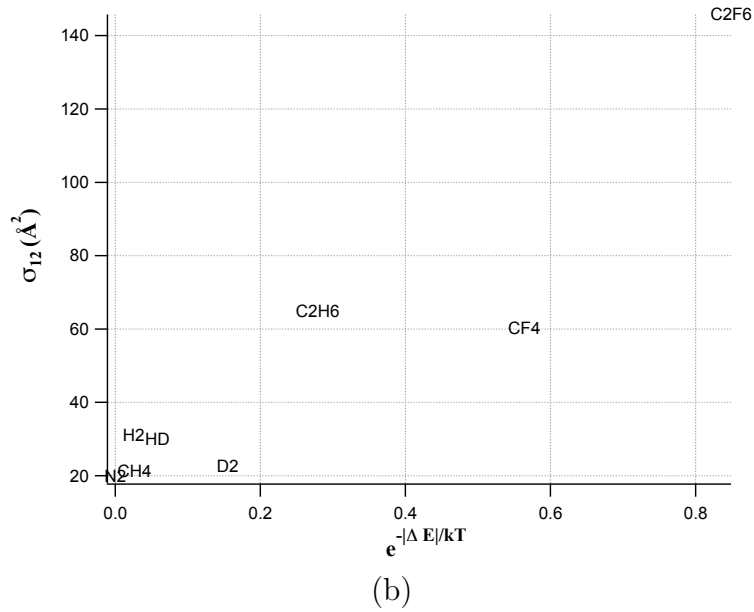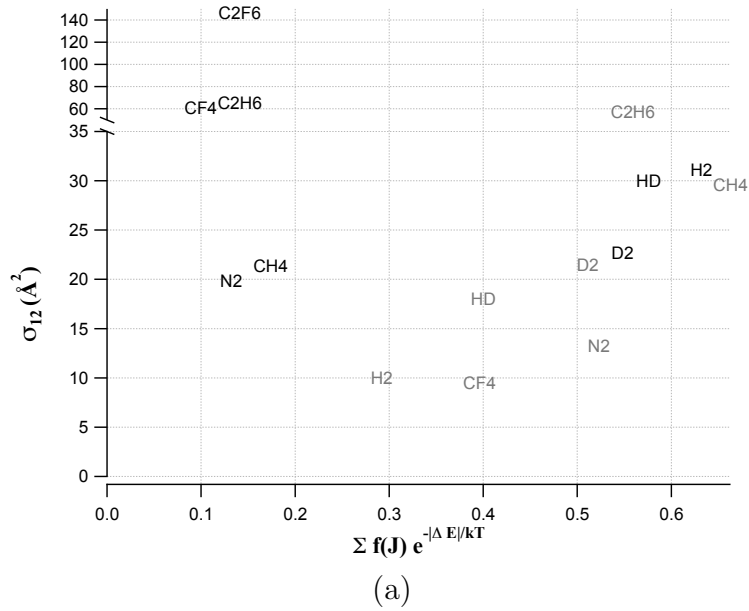
Figure 27. Demonstrations of the possible energy exchange between electronic to rotational (a) and electronic to vibrational (b) with inclusion of data from Rotondaro. [52]

cross-sections seem to follow a similar trend with the exception of ethane, carbon tetraflouride and hexafluoro-ethane. While these molecules have the smaller theoretical electronic energy exchange rate, they have the largest cross-sections.

Walentynowicz pointed out that carbon tetraflouride has a set of vibrational states (437 and 635 cm^{-1}) that are close to the energy defect cesium.[67] This leads one to believe that the energy is not being transfered to the rotational states like the others but instead into a vibrational state. Ethane has vibrational states (289 and 822 cm^{-1}) that have the same magnitude as the energy defect of Cesium and hexafluoro-ethane has a vibrational states at 520 cm^{-1} and 619 cm^{-1}. The relationship for electronic-vibrational energy transfer is shown in Figure 27 (b). It is important to note that the electronic-rotational transfer is possible, but it may not be as effective as electronic to vibrational energy transfer. For example, the the hydrides appear to achieved a maximum for the correlation to electronic-rotational transfer at 30 $\mathring{A}^2$, but on the other hand for the correlation to electronic to vibrational energy transfer CF_4 and C_2F_6 achieve a maximum ranging from 60-130 $\mathring{A}^2$. This leads one to believe that it is easier to access vibrational states over the rotational states of the collisional partner.

Conclusion

This study measured the rate of the spin-orbit energy exchange between cesium and various molecular collisional partners, improving the error for these measured cross-sections from 10% to 7% with the greatest variance produced in the measurements of ethane, 7.8 $\mathring{A}^2$. Based on the measured spin-orbit energy exchange cross-sections, it is this works recommendation for the DPAL community to attempt work with hexafluoro-ethane. Furthermore, the comparison between the energy defect of the alkali to the rotational and vibrational states of the collisional partner may reveal a carbon free partner.

71

VI. Producing infrared and blue beams with Alkalis

Introduction

The diode pumped alkali laser (DPAL) has been of great interest due to its potential for scaling for high power applications. This system will utilize diode bars or stacks to pump an alkali along its D_2 transition and lase along the D_1 transition. This concept was proposed by Krupke in 2003.[32] The DPAL system was initially demonstrated using rubidium, which resulted in a slope efficiency greater than 53%,[70] and cesium with a slope efficiency of 52%.[71] This laser system requires that the atomic transition be pressure broadened to match the broad diode pump, requiring broadening gas pressures of 1-20 atmospheres. In addition, a collisional partner must be introduced to relax the population from the pumped $^2P_{3/2}$ state to the $^2P_{1/2}$ state. This has been typically accomplished using ethane at pressures of several hundred Torr. An alkali is an attractive laser medium because of its large absorption cross-sections and its ability to rapidly cycle under high pump intensities.[40]

Other alkali lasers have been proposed in recent history that have produced both an infrared laser source as well as a blue one. One such approach utilized sequential pumping of cesium from its ground state, $6^2S_{1/2}$, to the $^2P_{3/2}$ state and then was pumped again by a second laser to the $6^2D_{5/2}$ state. The final excited state cascaded along the infrared transition to the $7^2P_{3/2}$ where it lased and produced a blue beam of 4 μW at 455nm.[9, 56] Lasing without inversion (LWI) has been demonstrated in rubidium via sequential double resonance processes.[72, 38, 73, 1] This produced a 40 μW blue beam by using two 20mW lasers to pump at 780 and 776 nm to coherently couple the 5S state with the 5P and 5D states. An amplified spontaneous emission in the infrared was observed when an alkali was pumped to its second excited P state in the blue.[58] This was proposed for rubidium and cesium and produced 16 different

72
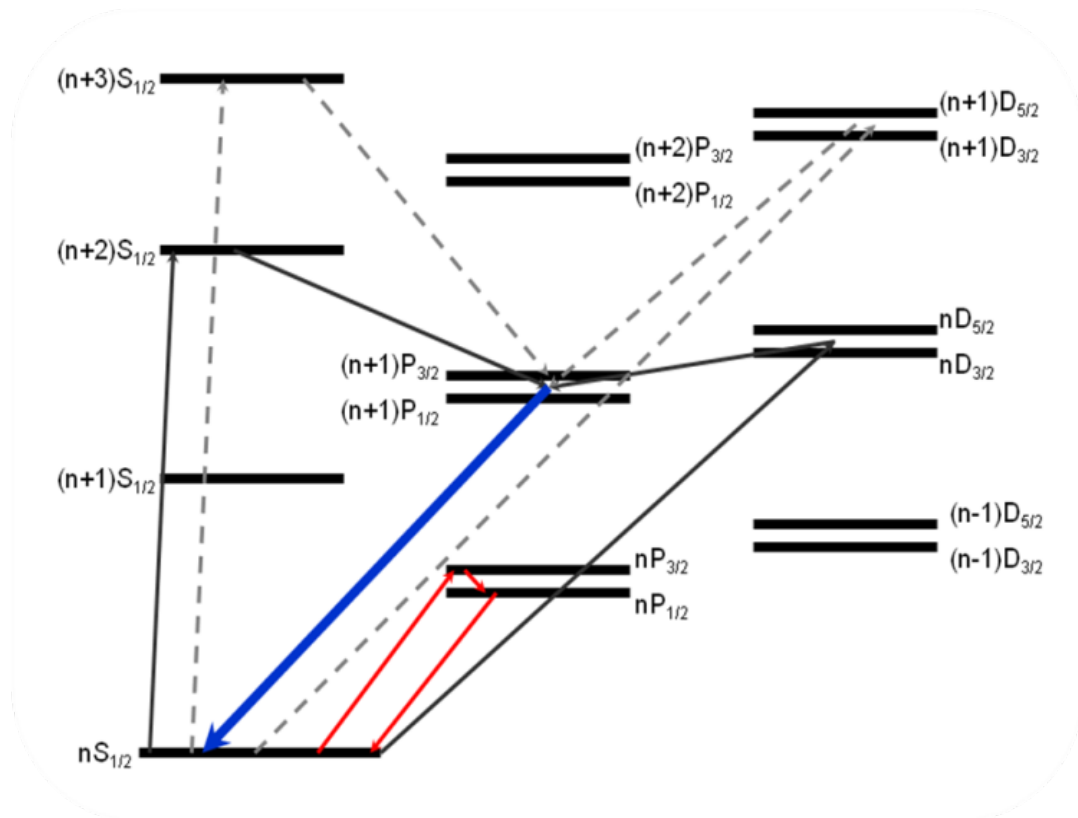
Figure 28. Energy Level Diagram for K ($\rightarrow$), Rb($\rightarrow$), and Cs($\rightarrow$), where n=4,5, and 6 respectively. Additionally, the typial red DPAL system is shown ($\rightarrow$)

IR lines. In addition, by utilizing two photons in the near IR and the IR photon, produced by optically pumped stimulated emission, a 7P-6S blue beam was observed in cesium. This was believed to be the result of four wave mixing.[22] This process arises from the third order optical nonlinearity, $\chi^{(3)}$, and is heavily dependent on phase matching between all optical waves involved.
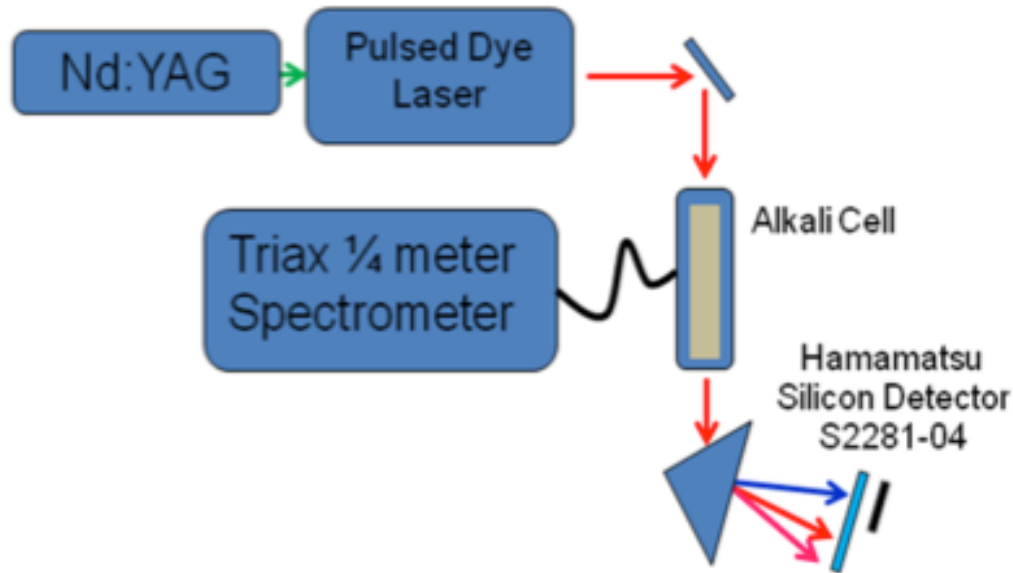
Figure 29. Experimental Apparatus for K blue beam

This group has recently produced a collimated blue beam and an IR beam utilizing a single intense pump source of rubidium and cesium.[64] The present work has produced similar results with potassium. These experiments used two photon absorption excitation of the $7^2D_{3/2,5/2}$ and the $9^2S_{1/2}$ states of cesium and the $n^2D_{3/2,5/2}$ and the $(n+2)^2S_{1/2}$ states of rubidium (n=6) and potassium (n=5). These processes are shown in Fig. 28. In contrast to a DPAL system, this two photon process operates at low pressure without collisional energy transfer, offering minimal heat loading. Also, in comparison to other blue systems, this requires a single near infrared pump source.

74

Experimental Apparatus

A diagram of the experimental apparatus is provided in Fig. 29 and is similar to previous work by Sulham et. al..[64] The pump source for the alkali was a Nd:YAG pumped Sirah dye laser with LDS-722 and LDS-765 dye. These dyes provided access to wavelengths from 685-760nm and 745-785nm, respectively. The output energy was up to 100 mJ in 8 ns pulses at 10 Hz and a spectral bandwidth of 16 GHz. The output of the dye laser was a beam with a radius of 3.5 mm and a divergence of less than 0.5 mrad.
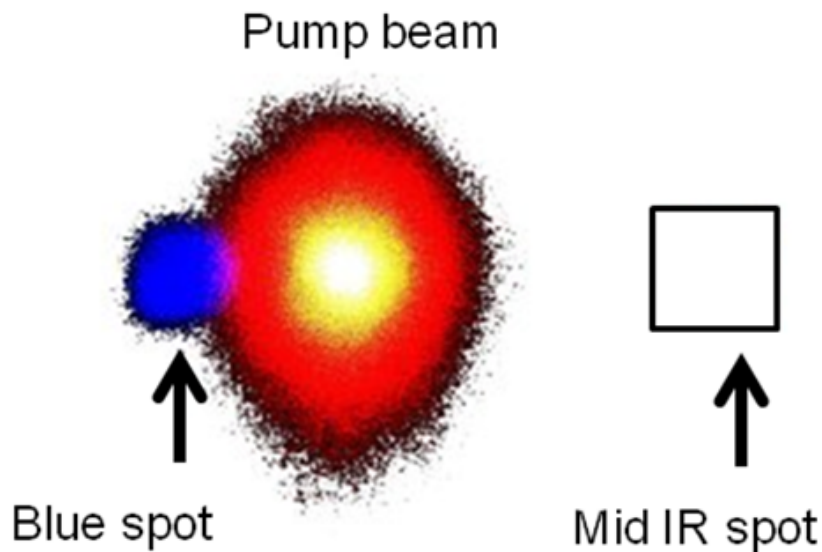
Figure 30. Dispersed beams for the Cs cell in the forward direction. The mid-IR Spot was not imaged, but is schematically located by spatially scanning with a point InSb detector with short pass filter.

The cesium and rubidium cells were produced by Triad technologies with a 2.5 cm diameter and 7.5 cm length and were heated to 448 - 524 K. When heated over 374

75

K, the potassium cell reacted with a contaminant that out gassed from the cell walls. Therefore, a heat pipe was utilized to keep the potassium off the windows. The heat pipe was operated at 528 and 556 K and initially was filled with 4 Torr of He. The heat pipe was attached to a gas handling system which was employed to vary the buffer gas.

After the beam passed through the cell/heat pipe, it was then sent into a BK7 prism to disperse the different wavelengths of light. Additionally, a short pass filter with a cut off at 460 nm was used to remove any scatter from the Nd:YAG and dye laser. A Hamamatsu S2281-04 large area silicon detector was employed with boxcar detection to record laser excitation spectra. The side fluorescence was recorded using a 0.25m Triax spectrometer and to verify the blue transition of the alkali. Average power was measured with a Coherent LM-3 HTD or a Newport 818-SL power meter for cesium and rubidium. The output of the potassium was too low to be accurately measured with available power meters and was instead qualitatively recorded with a new focus nanosecond silicon detector.

Results

A blue spot has been observed when pumping cesium, rubidium, and potassium on the two photon transition from the ground $^2S_{1/2}$ state to the highly excited $^2S_{1/2}$ and $^2D_{3/2,5/2}$ states. The beam that was produced, when pumping cesium, had a measured beam divergence of $\theta_{1/2} = 6$ mrad. This beam divergence is larger than the pump beam, < 0.5 mrad, but is much smaller than the fluorescence solid angle of 47 mrad. Additionally, a mid-infrared beam was also observed for cesium by spatially scanning an InSb detector with a 2.5 μm short pass filter. No IR beams were recorded for rubidium or potassium due to the transmissive properties of the cell windows. The resultant blue spot, pump beam, and relative mid-IR location are shown in Fig. 30.

76
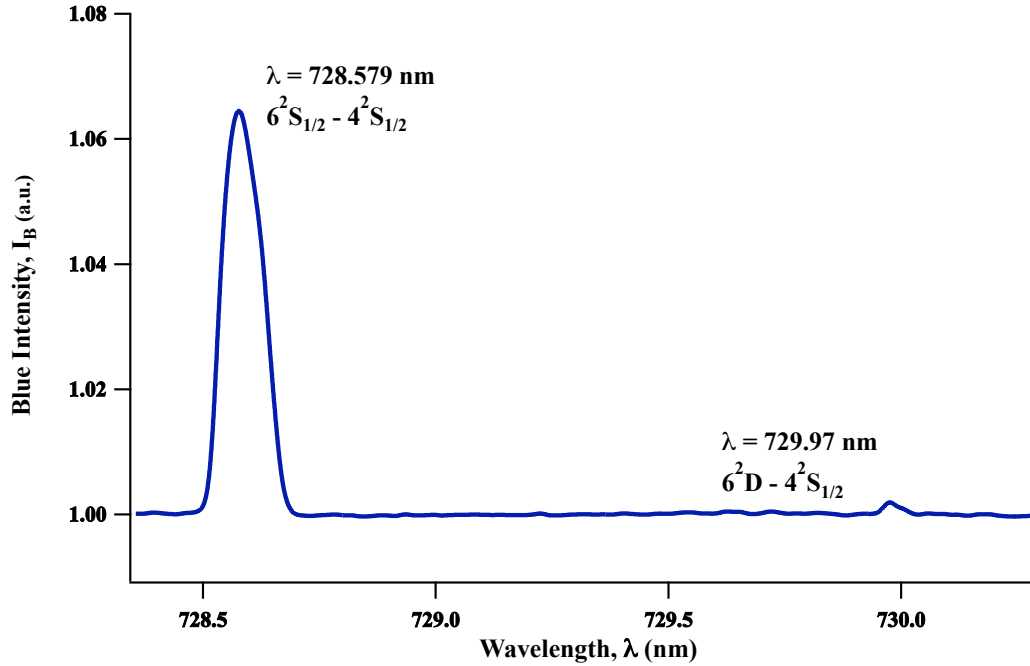
Figure 31. Excitation spectrum from potassium for a heat pipe at 553 K with 5.4 Torr of He.

Two-photon absorption.

A validation of the two-photon absorption process was the measurement of the excitation spectrum of the blue emission which was initially shown by Sulham.[64] An excitation spectrum for potassium is shown in Fig. 31 by monitoring the blue beam as the wavelength of the dye laser was scanned. The blue spot in potassium occur as expected at 728.6 nm and 729.9 nm. The fine splitting of the ^2D state was not observed due to the low signal of the blue intensity. (This effect may be due to helium buffer gas that is essential for heat pipe operation.) Similar experiments with a rubidium heat pipe demonstrated that while pumping the ^2D state as helium pressure was increased, the blue intensity diminished quickly. This may be due to the spin orbit mixing of the ^2D state, but further investigation is required. On the other

77

hand, while pumping the ^2S state, the blue emission for the heat pipe was observed up to 240 Torr of He.
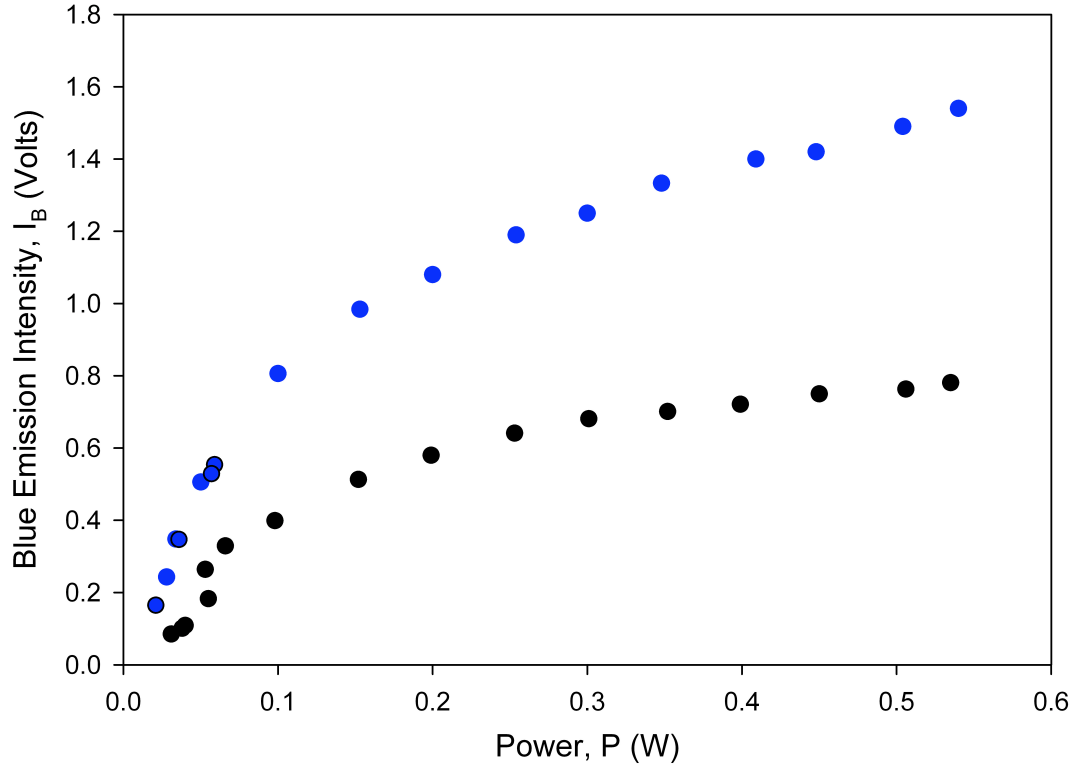
Figure 32. Blue intensity as pump power was varied for 528K (●) and 556K (●) while pumping along the $4^2S_{1/2} \rightarrow 6^2S_{1/2}$ two photon transition.

The blue emission from potassium as a function of the pump power is show in Fig. 32. The threshold for the blue beam for the $4^2S_{1/2} - 6^2S_{1/2}$ transition is approximately 260 kW/cm^2 ($\approx 1mJ/pulse$)and appears to decrease as the number density of potassium is increased. This trend, which is counter intuitive to a standard DPAL, is also shown by Sulham for cesium.[64] The relative slope efficiency for the potassium blue beam increases by approximately a factor of 4 as the number density is increased by a factor of 2.5.

78

Table 12. Possible ASE IR Transitions from excited alkali states.

Alkali	Transition	Wavelength (μm)
Potassium	$4^2D \rightarrow 5^2P$	3.7
	$6^2S \rightarrow 5^2P$	3.6
	$5^2D \rightarrow 5^2P$	1.8
	$5^2S \rightarrow 5^2P$	1.8
Rubdium	$5^2D \rightarrow 6^2P$	5.04,5.23
	$7^2S \rightarrow 6^2P$	3.85,3.97
	$6^2D \rightarrow 6^2P$	2.01,2.04
	$8^2S \rightarrow 6^2P$	1.876,1.90
Cesium	$6^2D \rightarrow 7^2P$	12.14,14.59
	$8^2S \rightarrow 7^2P$	3.92,4.22
	$7^2D \rightarrow 7^2P^\dagger$	2.33,2.43
	$9^2S \rightarrow 7^2P$	1.94,2.01

† Observed by Sulham.[64]

Mid-IR Beam.

All experiments were performed with little to no buffer gas and therefore the transfer of the population from the pumped state to the upper blue $^2P_{1/2,3/2}$ state must occur optically. The optical transition between the pumped state and P state produces an IR beam that was observed when pumping cesium to the $7^2D_{3/2}$, $7^2D_{5/2}$, and $9^2S_{1/2}$ states. Using an InSb point detector and a 2.5 μm short pass filter, the 2.34 μm and 2.43 μm spots from the $7^2D_{3/2} \rightarrow 6^2P_{1/2}$ and $7^2D_{5/2} \rightarrow 6^2P_{3/2}$ transitions were observed. The IR spot was mapped out by scanning the InSb point detector spatially. It is assumed that the other alkalis produce similar IR ASE but were not observed due to the transmission properties of the cell in the far IR. The IR wavelengths of the other alkalis are shown in Table 1. More IR transitions are accessible by pumping higher ^2D and ^2S states. The IR transitions from the blue ^2P to the first exited ^2D and ^2S states were observed by Sharma.[58] Also, Hamadani observed the IR beam transition which was used to explain the four-wave mixing.[22]

79

Emission from Highly Excited States.

Significant side fluorescence from many highly excited states are observed both by two-photon pumping and by pumping along the D_2 transition. An example of these emissions are shown in Fig. 33. The D_2 transition in rubidium was pumped and the side fluorescence was monitored using a 0.25m Triax spectrometer. The temperature of the cell was maintained at 503K with no buffer gas present. While pumping with 28 mJ in an 8 ns pulse, more than 20 highly excited states were observed.

These highly excited states imply that energy pooling may be a negative effect on red DPAL systems as they are scaled. However, there are no observed Rb ion transitions which would have a catastrophic effect on the DPAL system.
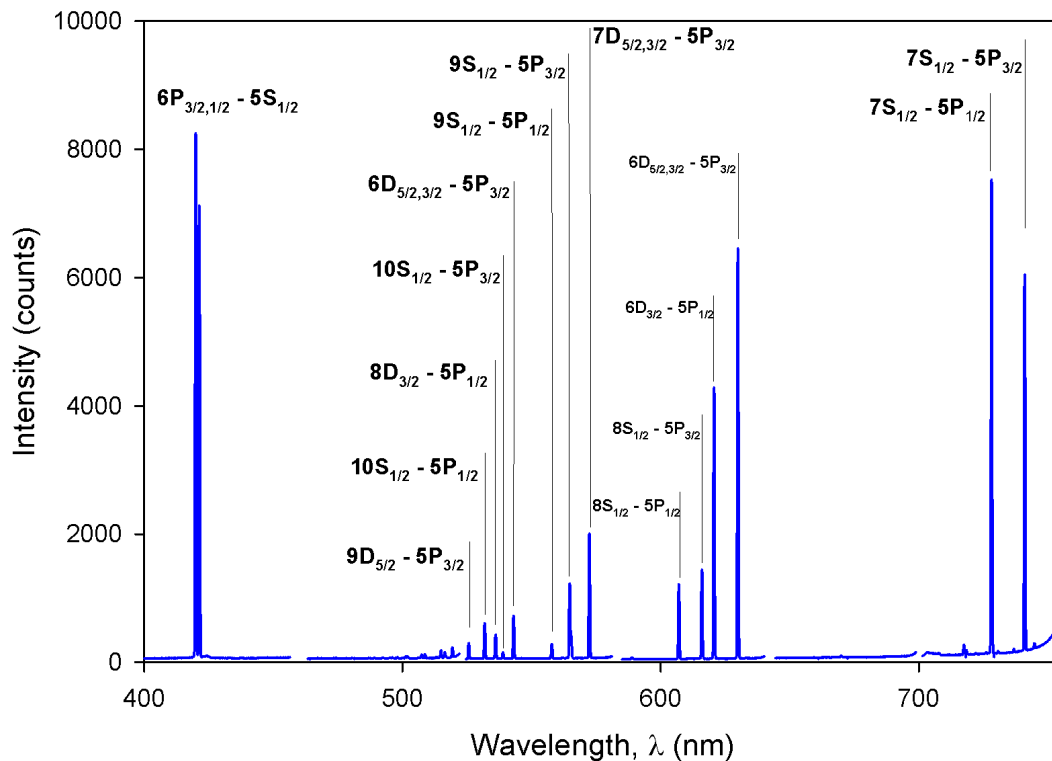
Figure 33. A side fluorescence spectrum from rubidium while pumping along the D_2 transition.

Discussion.

A collimated blue beam of the wavelength that corresponds to the $(n+1)^2P \rightarrow (n)^2S$ transition has been observed for K, Rb, and Cs by pumping at a single wavelength via two-photon absorption. There are two possible mechanisms for the blue beam. One, as suggested by Sulham[64], is amplified stimulated emission. The other is 4 wave mixing as suggested by Hamadani.[22] It has been suggested by Malcuit,[35] that by counterpropagating the pump waves four wave mixing can be suppressed. In both the case of this study and that of Sulham et. al[64] a mirror that reflected the red pump beam back into the cell and passed the blue was used. Both mechanisms are plausible and may be in competition with one another. Further study is required to understand the decreasing threshold with increasing number density, the non linear nature of the blue beam intensity compared to the linear IR beam intensities, and the differences in the pressure effects on the blue beam when pumping the ^2D versus the ^2S states.

The addition of even small amounts of buffer gas has a negative effect on the D state. This is believed to be due to spin orbit mixing between the $^2D_{5/2}$ and $^2D_{3/2}$ states, but further work is needed. While pumping the ^2S state, the blue emission was observed to pressures over 200 Torr of He within a heat pipe at 280C. The $(n+1)^2P$ state was populated by lasing from the pumped state. This offers no quantum defect and the potential for low heat loads. In addition to providing a source for blue light, this system gives access to multiple IR laser lines. Each alkali provides numerous transitions that can provide IR light by pumping higher and higher states. Over 20 highly excited states have been observed when pumping with high pump intensities and high number densities. It is likely that as DPAL is scaled with pump intensity, energy pooling will play a more significant role in laser performance.

81

VII. Conclusions

Prior to this work, the broadening and shift rates for cesium were in disagreement, as shown by the discrepancies between measured broadening values for nitrogen as compared to its average, 28%, and for helium, 14%.[4, 15, 12] The differences in the shift rate were also quite significant. In the case of the shift rate of the D_2 transition caused by collisions with helium it was previously measured to be blue shifted by one source and red shifted by others.[4, 15] The accuracy of these rates are essential for application in models of DPAL systems, especially as they are driven up to higher pressure conditions to match diode pump width and achieve the desired spin-orbit relaxation rates.

These rates for energy exchange between the $^2P_{3/2}$ and $^2P_{1/2}$ states have not been updated since 1974.[67, 68] The measurements of these rates, when induced by collisions with complex molecules, did not account for quenching, and only evaluated conditions under 1.5 Torr, conditions that are not being utilized by current DPAL systems. Also, the prior work was measured with a potential error of 10% leaving room for improvement.

Furthermore, while attempting to demonstrate a DPAL system here at AFIT, a blue beam was produced while pumping along the two photon transition, $(n)^2S_{1/2} \rightarrow (n, n+1)^2D_{3/2,5/2}, (n+2, n+3)^2S_{1/2}$ of rubidium and cesium. In addition, while producing this blue beam, an infrared beam of amplified spontaneous emissions occurred simultaneously.[64] This demonstration did not utilize the lighter alkali, potassium, which would extend the light further into ultra-violet spectrum.

Broadening and Shifts

This work has provided an expanded and updated list of broadening and shift rates needed by the community for the development of complex alkali laser models to predict the scalability of the DPAL system. The cross-sections derived from these rates are summarized in Tables 13 and 14. The broadening and shift rates were measured with an error less than one percent. Due to the high quality of spectrums acquired, as shown in Appendix B, the effect of velocity changing collisions was observed in the line shape. In addition to these values, the interatomic difference potentials were calculated. This provides the theoretical community with a window into the understanding of the interatomic forces at play when neutral molecules interact with cesium. In addition, a comparison between the D_1 and D_2 cross-section were made in Fig. 19. This provided an update on the observations made by Hindmarsh and Farr and expanded it to include values for the most recently measure rates for sodium, potassium, and rubidium.[23, 45] For the broadening rates of the alkalis, Hindmarsh and Farr observed that the D_1 broadening tended to be slightly greater than that of the D_2 transition. This is in disagreement with the results shown below in Tables 13 and 14. On the other hand, Hindmarsh and Farr made several observations concerning the shift rates of the alkalis. First, the difference in the shift is dependent on the perturber and not on the nature of the alkali. Second, where there is a blue shift of the transition, the $^2P_{\frac{1}{2}}$ rate is greater than the $^2P_{\frac{3}{2}}$. Third, the red shifts are typically small and there is no way to predict which transition will have the greater shift. These three observations were validated by this work.

Spin-Orbit Relaxation

This work has provided an updated list for the spin-orbit energy exchange rates needed by the community for the accurate modeling of the DPAL system. The cross-

Table 13. Measured cross-sections ($\mathring{A}^2$) for the D_1 transition obtained from the pressure broadening, shift, and spin-orbit experiments.

Collision Partner	Pressure Broadening	Pressure Shift[†]	Spin-Orbit σ_{21}
He	60.84	10.69	——
^{3}He	57.11	13.20	——
Ne	57.18	-8.43	——
Ar	127.77	-45.15	——
Kr	160.85	-49.29	——
Xe	202.00	-65.80	——
H_2	37.80	2.02	4.43
HD	43.76	1.02	4.09
D_2	45.27	0.002	3.02
N_2	96.58	-46.95	2.34
CH_4	142.50	-45.60	2.95
C_2H_6	171.20	-54.76	9.93
CF_4	173.98	-55.96	7.78

[†] Sign used to indicate direction.

sections derived from these rates are also summarized in Tables 13 and 14. The spin-orbit rates were measured utilizing buffer gas pressure up to 100 Torr and quenching was included in the model that was employed to extract these rates (which was not included before).[67, 68] The error on these cross-sections were decreased by 3%. In addition, the cross-sections were then correlated to a simple model for energy exchange between the excited state of cesium and the rotational states of the collisional partner, shown in Fig. 27. This revealed a slight correlation between the simpler/less massive molecules and the cross-section for spin-orbit coupling. Furthermore, the outliers of this correlation revealed the possibility of electronic to vibrational energy transfer. Ethane and carbon tetraflouride have *nearly* resonant vibrational states with the energy defect of cesium. For example, CF_4 has the strong similarity between its vibrational energy and the Cs energy defect with two vibrational states at 437 and

Table 14. Measured cross-sections ($\mathring{A}^2$) for the D_2 transition obtained from the pressure broadening, shift, and spin-orbit experiments.

Collision Partner	Pressure Broadening	Pressure Shift[†]	Spin-Orbit σ_{12}
He	51.12	1.71	——
^{3}He	48.33	1.30	——
Ne	51.71	-13.6	——
Ar	114.96	-43.14	——
Kr	140.31	-54.99	——
Xe	188.43	-69.09	——
H_2	48.15	-8.57	31.10
HD	51.14	-9.72	30.01
D_2	56.88	-11.31	22.69
N_2	116.19	-37.56	19.86
CH_4	123.13	-42.22	21.36
C_2H_6	163.02	-58.50	64.83
CF_4	163.21	-59.29	60.34

[†] Sign used to indicate direction.

635 cm^{-1}. Ethane, on the other hand, has a vibrational states at 289 and 822 cm^{-1}). This would imply that C_2F_6, if it does not react with Cs, would be an excellent collisional partner for spin-orbit energy exchange because of it's vibrational state at 619 and 520 cm^{-1}, only a total energy defect of 65 and 34 cm^{-1}.

Potassium Blue and IR Beams

This work has demonstrated the production of a blue beam by pumping potassium with two red photons. A dim beam was produced by pumping along the $4^2S_{1/2} \rightarrow 6^2S_{1/2}$ transition. A beam was produced by the $4^2S_{1/2} \rightarrow 4^2D_{3/2,5/2}$, but was not observable to the naked eye. In addition, the helium pressure was increased to 240 Torr, while pumping the $4^2S_{1/2} \rightarrow 6^2S_{1/2}$ transition, before the blue beam was lost. On the other hand, while pumping to the D state in rubidium the blue beam was

lost at only a few Torr. This is believed to be due to the spin orbit mixing of the D state. The blue beam has two potential sources; (1) four-wave mixing and (2) amplified spontaneous emission. Malcuit suggested that by back-reflecting the beam, the four wave mixing process can be disrupted.[35] This was a part of this work experimentation and thus the belief that a blue amplified spontaneous emission was observed.

Future Work

As the diode pumped alkali laser system is developed, more opportunities for research will arise, one on which is concerning the current problem with carbon based spin-orbit coupling gases producing soot and laser snow. Due to this problem, the DPAL community is looking to potassium with helium as a potential scaleable source. Potassium is the least studied in terms of broadening rates and only a miniscule amount of study has been accomplished in terms of spin-orbit mixing rates.[34] If potassium is the direction the community must head in, then this work must be accomplished. In addition, the potassium laser wavelength is near the $O_2(b)$ rotational lines and thus it must be determined if there is significant atmospheric absorption by oxygen at this laser wavelength. Furthermore, the *trade-offs* of moving between alkalis must be investigated. A series of experiments and models must be produced to weigh all the positive and negatives of the alkali frequencies in terms of atmospheric conditions.

Outside of the DPAL community the blue beam can be further developed with the intent of creating a full blue laser. In addition, the IR side of the alkalis can be further developed. If all the possible wavelengths of all the alkalis were studied as suggested by this work, this would effectively turn the alkalis into the swiss army knife of the laser community. Then potassium, rubidium, and cesium would be able to

86

provide a medium that could provide 20 different IR sources, 4 different NIR sources, and 4 blue sources all by pumping in the red. This does not include sodium and its possibility of producing an ultra violet source. Once a sodium is proven to be a laser medium, it could go from firing projectiles across battlefields to producing coherent light.

Appendix A. Frequency Calibration

Time to Frequency Calibration

The conversion of the time of scan to the frequency is essential to the measurement of the characteristic effects of the line profile of cesium. This conversion was accomplished after the experiment using the known transitions in frequency of the hyperfine profile of cesium as well as an etalon cavity with a calibrated free spectral range. The reference cell provided a low pressure hyperfine spectrum that provided the spectral spacing for the time to frequency conversion as well as a means for calibration of the free spectral range of the etalon for each buffer gas and pressure. A typical scan is shown in 34.
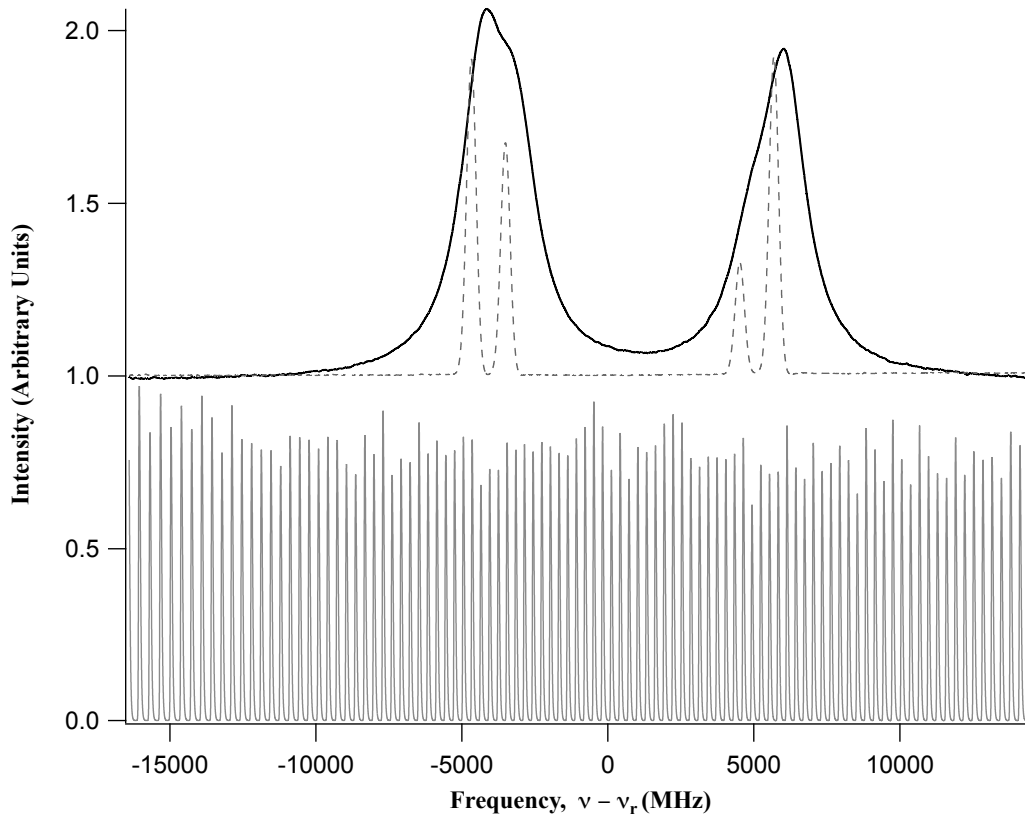
Figure 34. An example of a typical scan recording during the experimental process.

88

The spectral spacing of the hyperfine structure of Cesium is extremely well known due to its use in atomic clocks. The relative spacing for the D_1 and D_2 lines are shown Table 15. The spacing for the D_1 hyperfine spectrum is large enough to be completely resolvable at room temperature, but on the other hand the spacing up the $^2P_{3/2}$ is less than 300 MHz which is less than the Doppler widths observed during experimentation.

Table 15. The cesium hyperfine line shifts from line center for the D_1 and D_2 transitions.

Transition	$F'' \rightarrow F'$	Frequency Shift (GHz)
D_1 $^2S_{1/2} \leftarrow$ $^2P_{1/2}$	$4 \rightarrow 4$	-3.5109164
	$3 \rightarrow 4$	-4.6785964
	$4 \rightarrow 3$	5.68171537
	$3 \rightarrow 3$	4.51403537
D_2 $^2S_{1/2} \leftarrow$ $^2P_{3/2}$	$5 \rightarrow 4$	-3.7578858
	$4 \rightarrow 4$	-4.0089779
	$3 \rightarrow 4$	-4.2102649
	$4 \rightarrow 3$	5.18365388
	$3 \rightarrow 3$	4.98236687
	$2 \rightarrow 3$	4.83114257

Converting the Time Scan into a Frequency Scan

The nature of the spacing of the D lines provides a frequency reference in time space. It is first essential to make the assumption that the scan rate over the range of the hyperfine structure is constant. Applying this assumption in time space, the temporal free spectral range or the average time between etalon peaks is constant. The temporal free spectral range (FSR) is then employed to determine the number of temporal-FSR's between the hyperfine lines. This value is then used with the frequency spacing of the hyperfine transition, this is the frequency free spectral range.

89

This method is applied across the major spacing of the hyperfine structure and the average frequency-FSR is calculated.

Once the frequency-FSR is determined, the location of the etalon peaks in time is plotted against thier place in frequency space. Additionally the four reference lines of the D_1 line are plotted, this is shown in Fig. 35. A quadratic is then fit to this line with more weight being applied to the reference line data. The resulting coefficients of the fit function produces the means to convert time to frequency for the D lines.
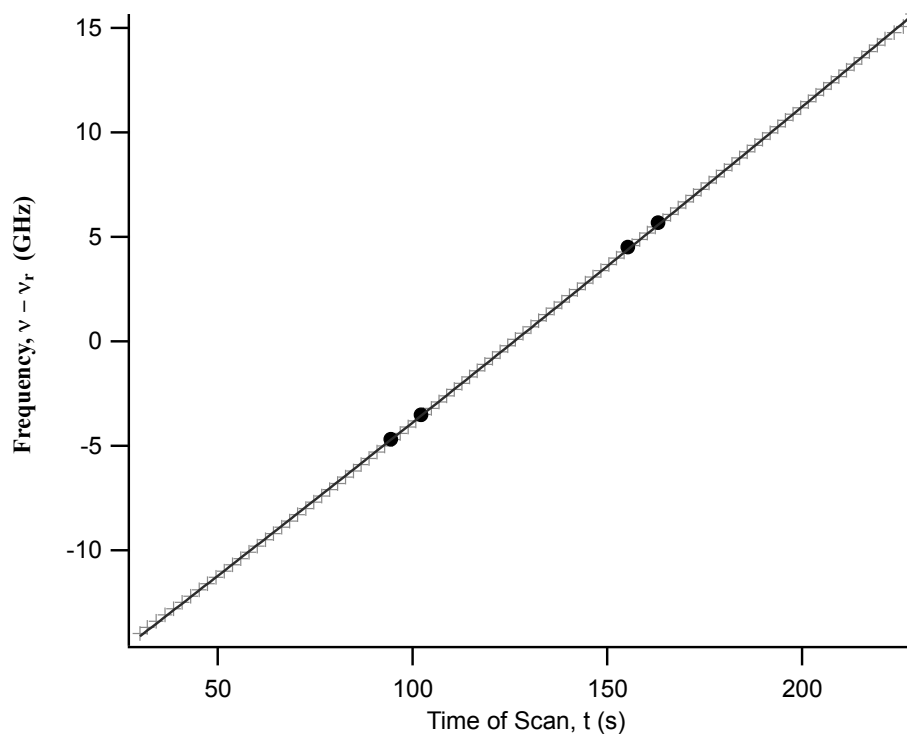
Figure 35. A typical plot of the location of the reference spectrum ($\bullet$) and etalon peak ($+$) in frequency as a function of time.

Dissimilarities between Time to Frequency Conversion of the D_1 & D_2 Lines

One problem that arises when converting the D_2 line to frequency space that does not arise in the conversion D_1 is the locations of the reference peaks. For the D_1 line

at low pressures all the hyperfine lines are resolved, but for the D_2 line they are not. The hyperfine spacing for the D_2 transition, as shown in Table 15, are not resolveable with simple absorption spectroscopy. Therefore, an additional step was needed.

For the D_2 line, instead of measuring a temporal FSR, a guess at the frequency FSR was made. The first guess was the average FSR from the D_1 broadening experiments. This resulted in the first stab at the conversion of the time to Frequency conversion. For simplicity sake, this frequency space will be called the transitional space and symbolized, ν_T. With the transitional space established the reference spectrum with it's known hyperfine transitions can be utilized. So, the reference spectrum was fit to the following equation:

$$A = -ln\left(\frac{I}{I_0}\right) = c_0 + c_1\nu + c_2\sum_{i=1}^{6} a_i V\left((\nu_T - \nu_i)\xi, \Delta\nu_L; \gamma_D\right), \qquad (47)$$

where

ν_i = line center frequency at zero pressure for the ith hyperfine component,

$\Delta\nu_D$ = 386 MHz = Doppler width (FWHM) contrained at T = 313K,

ξ = frequency stretch factor,

$\Delta\nu_L$ = Lorentzian width (FWHM).

The Lorentzian width was set to the natural width due to the absence of any buffer gas. The ξ term produced a stretching factor to account for an nonlinearity that was produced by a faulty initial guess. If ξ was not equal to one, the FSR was adjusted accordingly and the process was repeated until it did.

91

Appendix B. Pressure Broadening Data

This appendix contains the rest of the data acquired for this work. A scientist is forced in the process of publication to pick their favorite set of data, but that is like picking your favorite child. This appendix is the opportunity of my other children to share what they have to offer with the world.
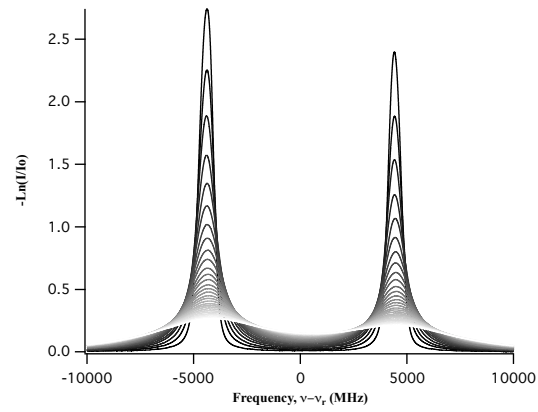
D_1 Broadening & Shift Data

(a)

(b)

(c)
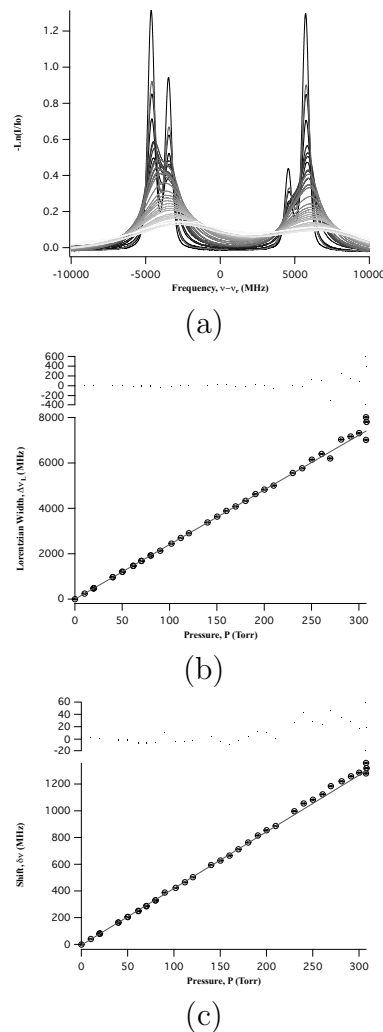
Figure 36. Cesium D_1 transition with increase pressures of helium (a) and the resulting widths (b) and shifts (c).
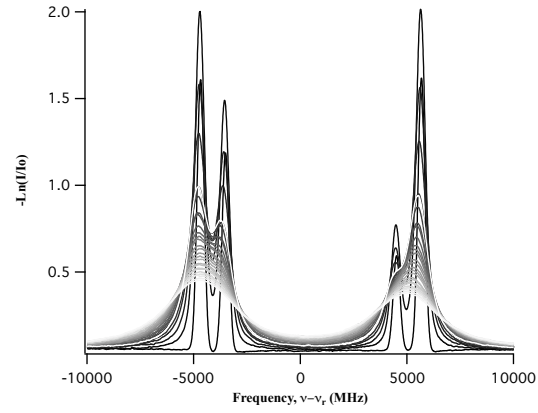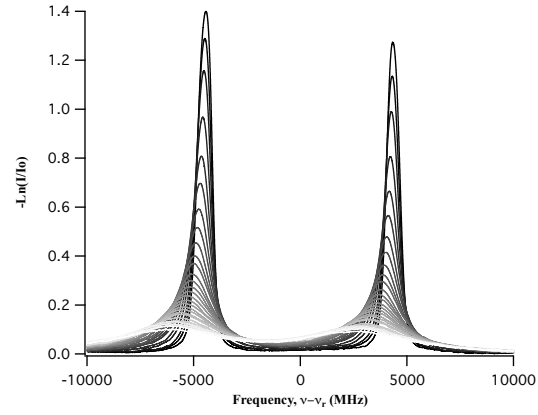
(a)
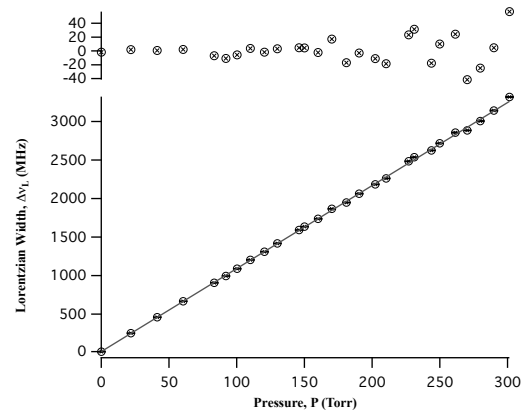
(b)
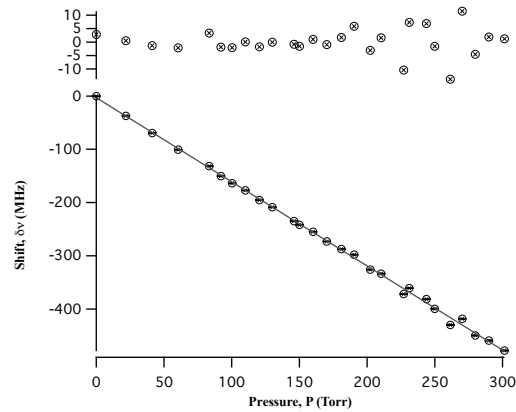
(c)

Figure 37. Cesium D_1 transition with increase pressures of neon (a) and the resulting widths (b) and shifts (c).

93
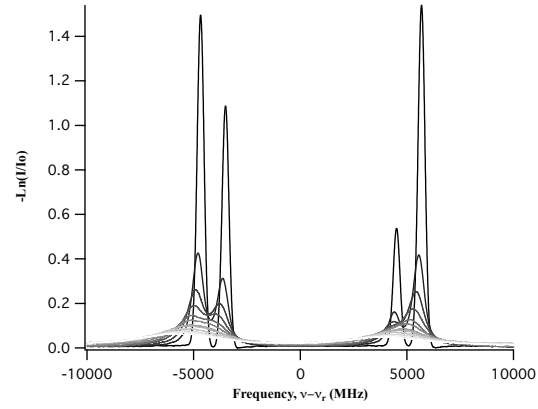
(a)
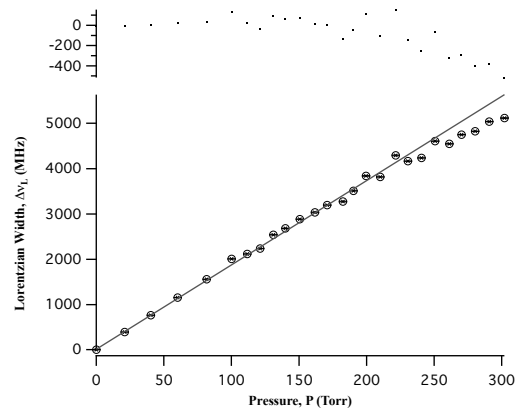
(b)
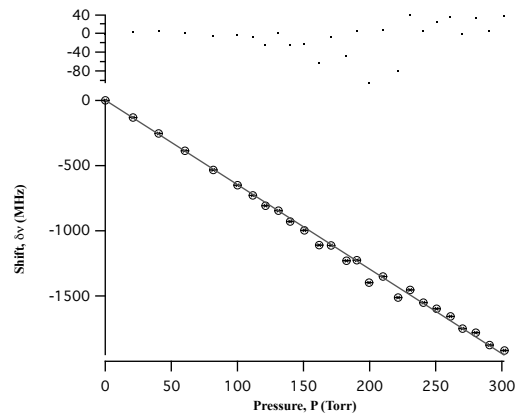
(c)

Figure 38. Cesium D_1 transition with increase pressures of argon (a) and the resulting widths (b) and shifts (c).
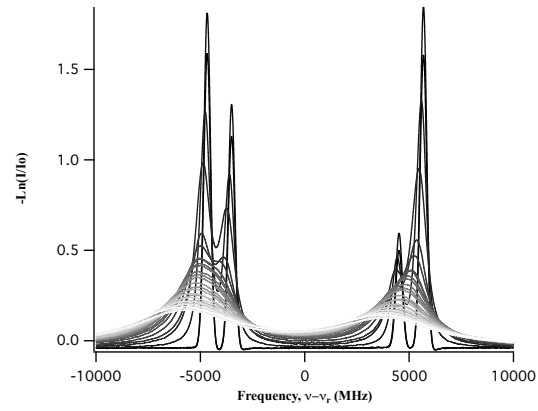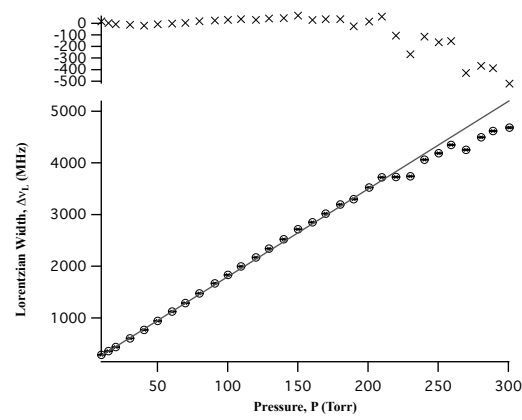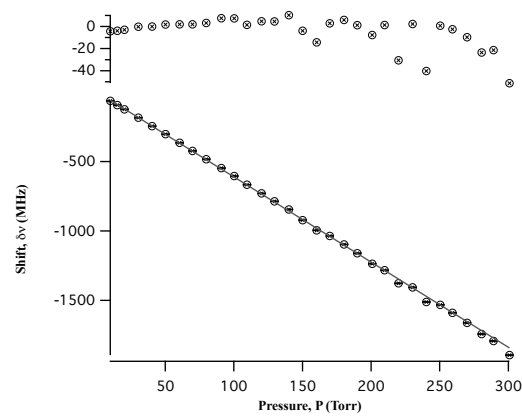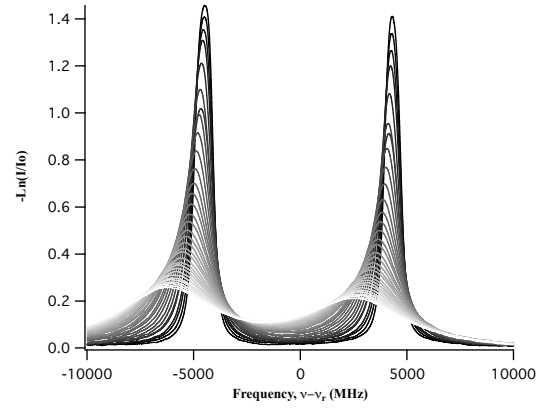
(a)
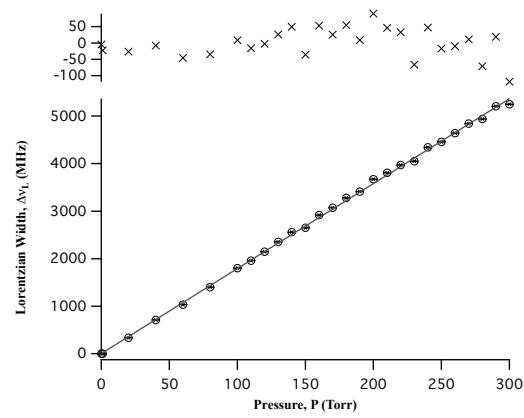
(b)
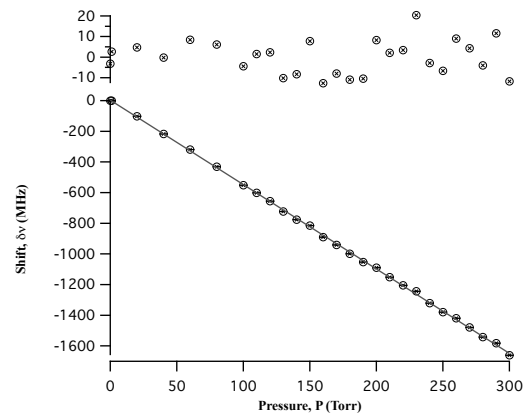
(c)

Figure 39. Cesium D_1 transition with increase pressures of krypton (a) and the resulting widths (b) and shifts (c).
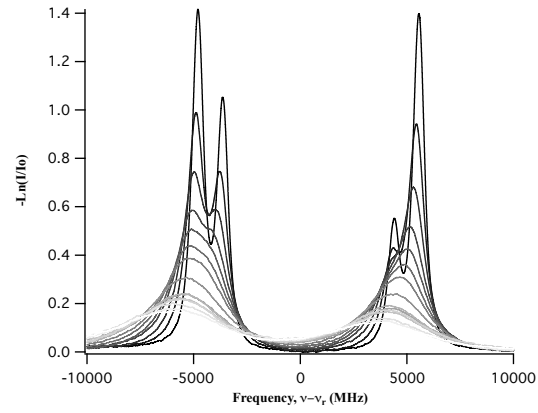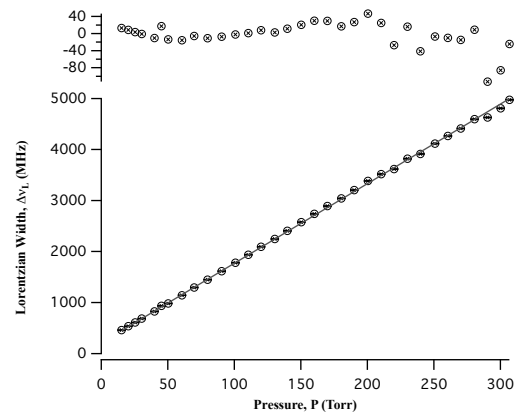
(a)
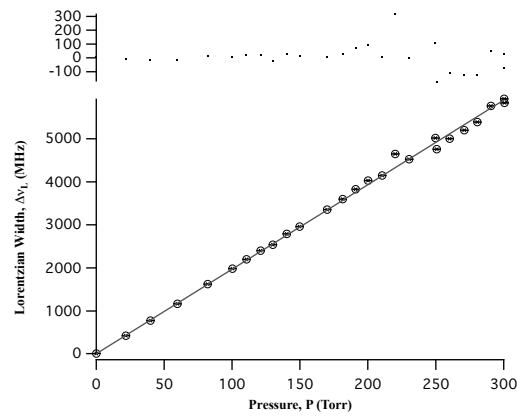
(b)
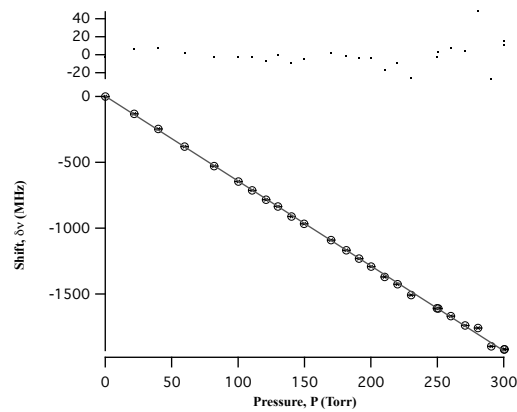
(c)

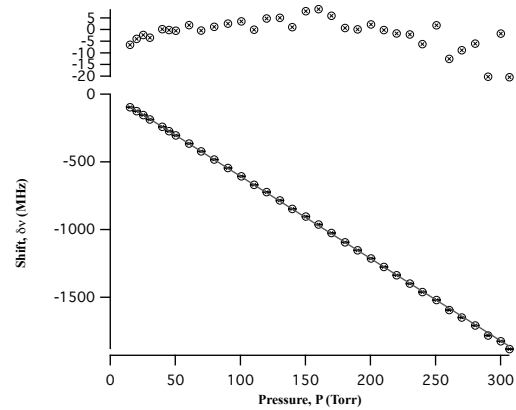**Figure 40.** Cesium D_1 transition with increase pressures of xenon (a) and the resulting widths (b) and shifts (c).

96
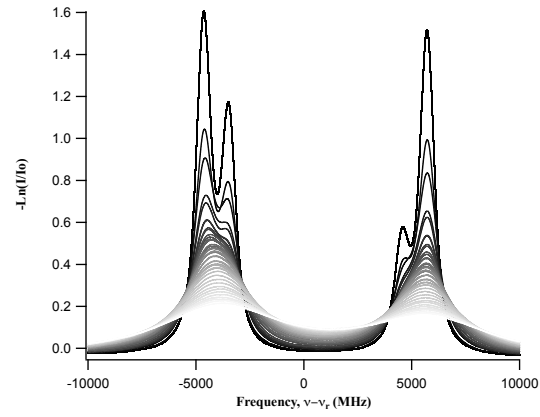
(a)
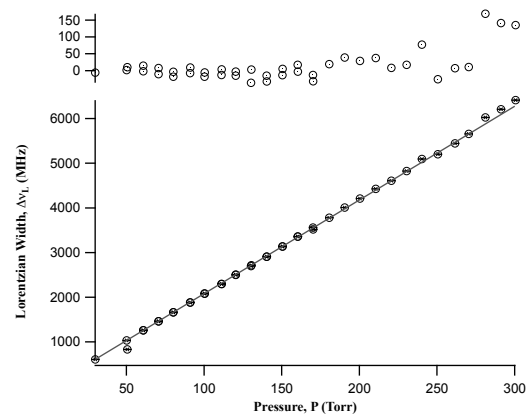
(b)
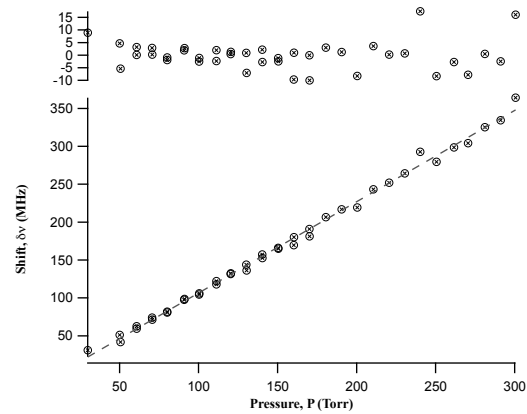
(c)

Figure 41. Cesium D_1 transition with increase pressures of H_2 (a) and
the resulting widths (b) and shifts (c).

97
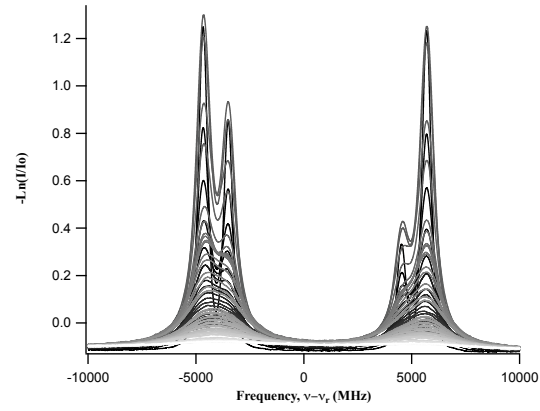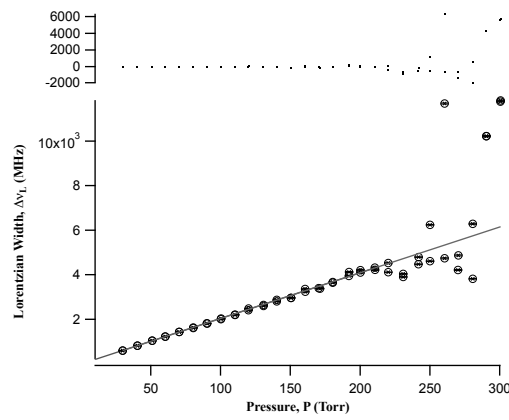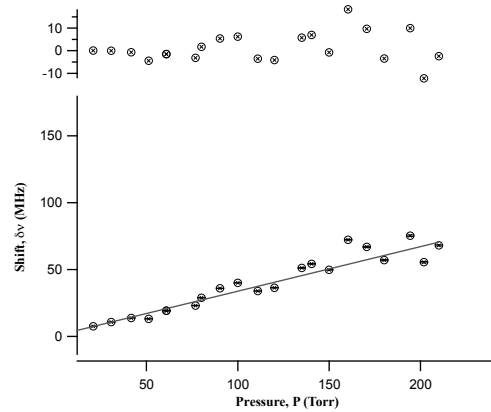
Figure 42. Cesium D_1 transition with increase pressures of HD (a) and the resulting widths (b) and shifts (c).
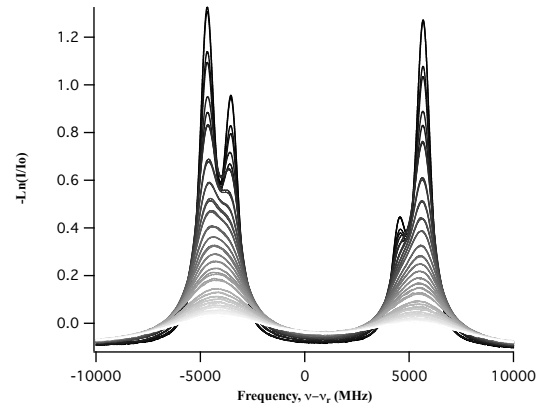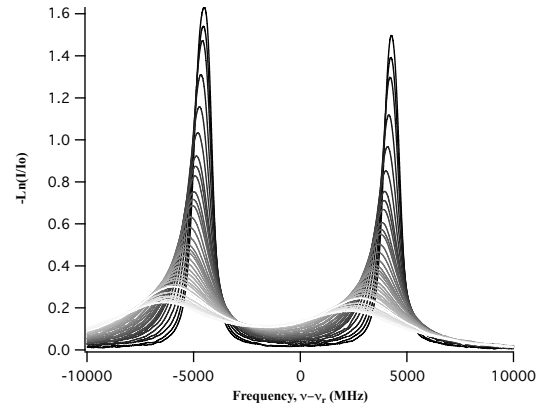
(a)
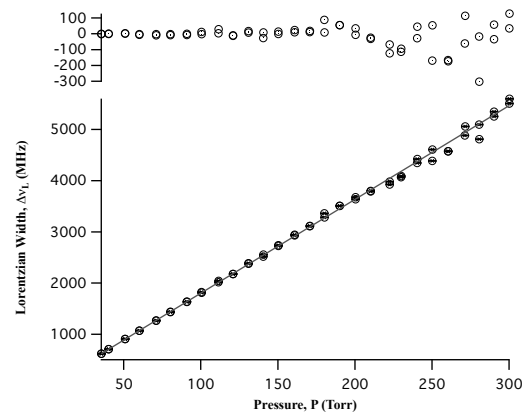
(b)
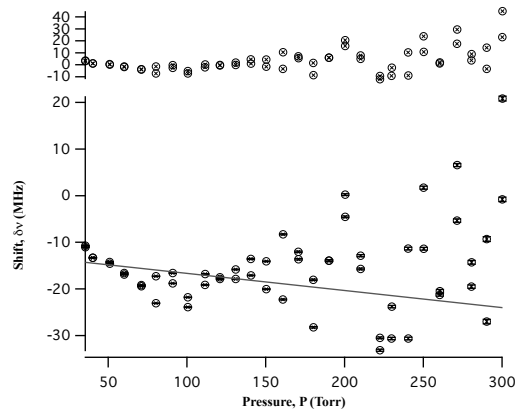
(c)

Figure 43. Cesium D_1 transition with increase pressures of D_2 (a) and the resulting widths (b) and shifts (c).

99
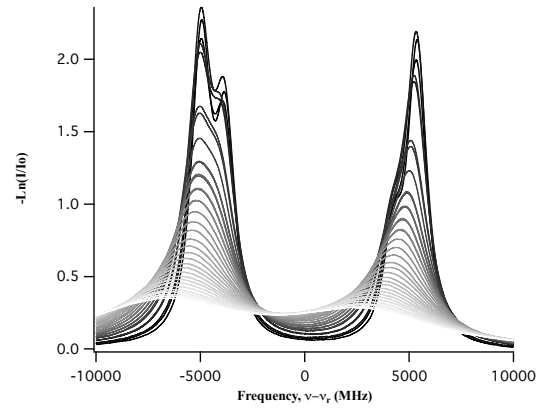
(a)
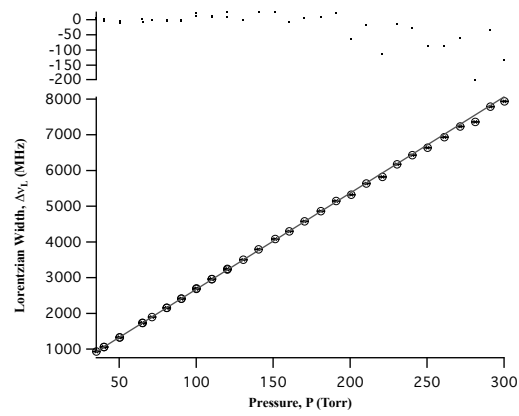
(b)
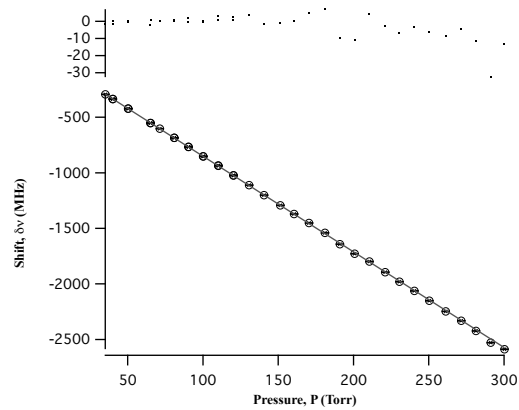
(c)

Figure 44. Cesium D_1 transition with increase pressures of CH_4 (a) and the resulting widths (b) and shifts (c).
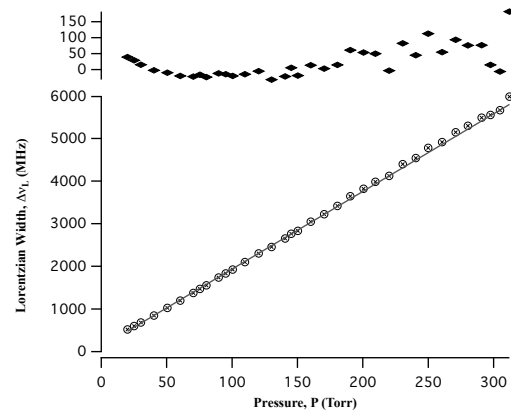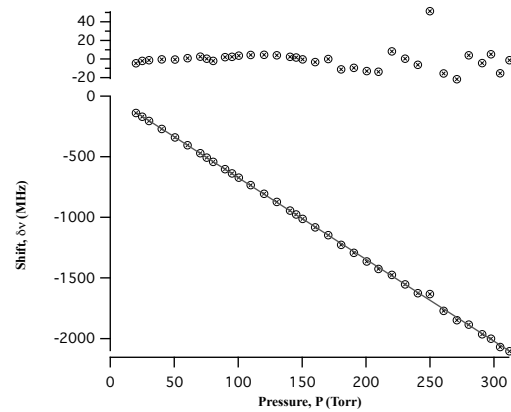
100
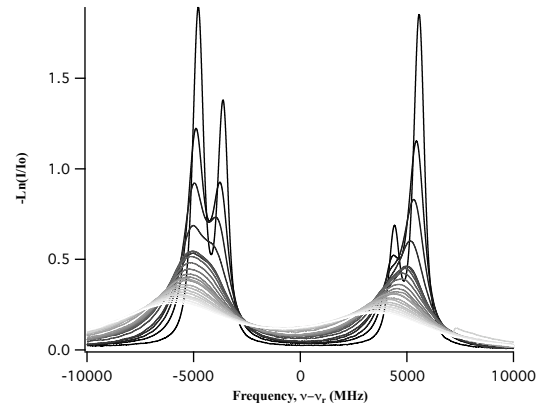
(a)
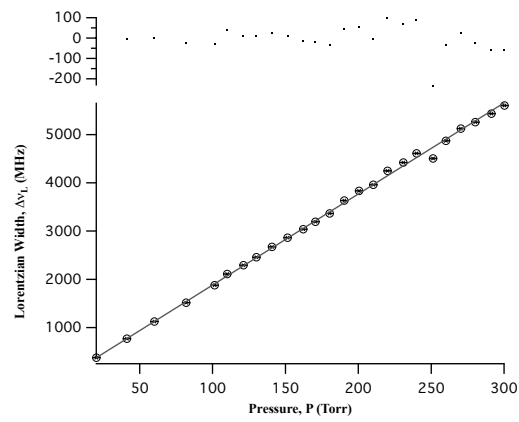
(b)
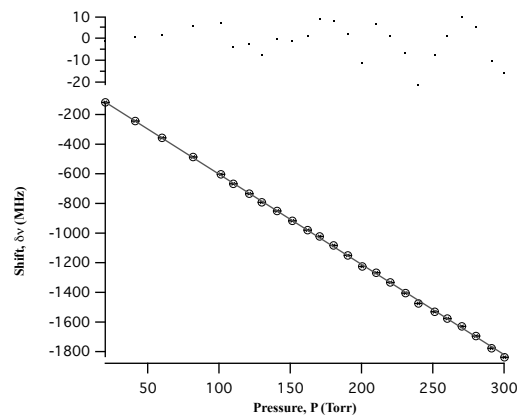
(c)

Figure 45. Cesium D_1 transition with increase pressures of CF_4 (a) and the resulting widths (b) and shifts (c).

101
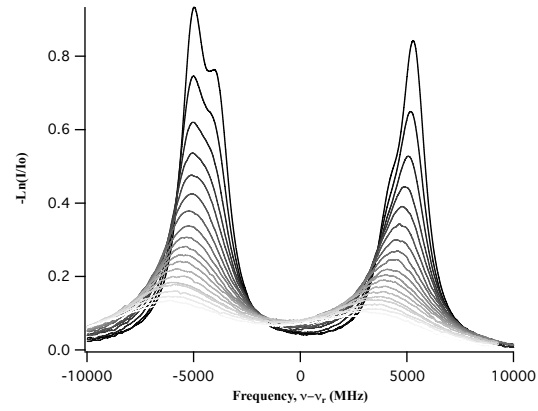
(a)
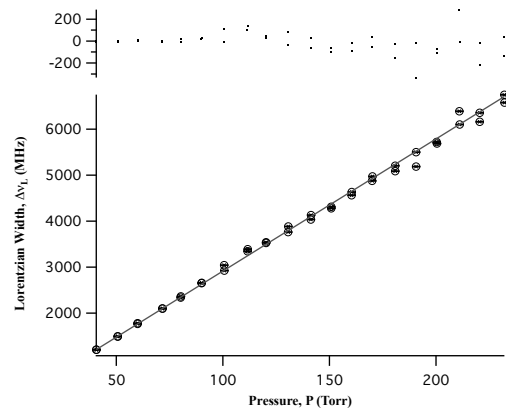
(b)
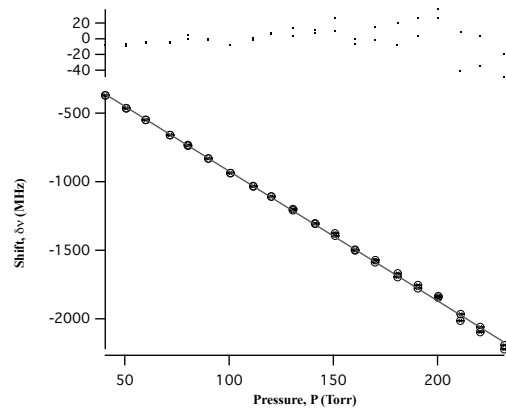
(c)

Figure 46. Cesium D_1 transition with increase pressures of C_2H_6 (a) and the resulting widths (b) and shifts (c).

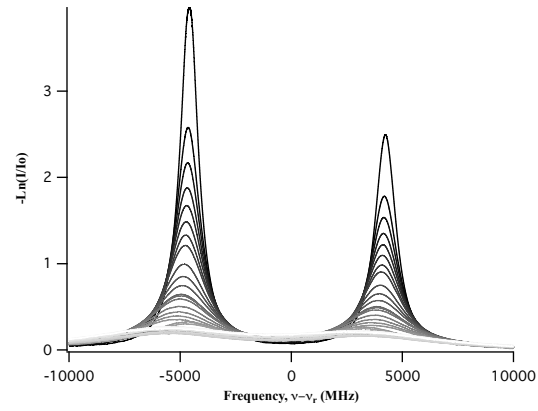102
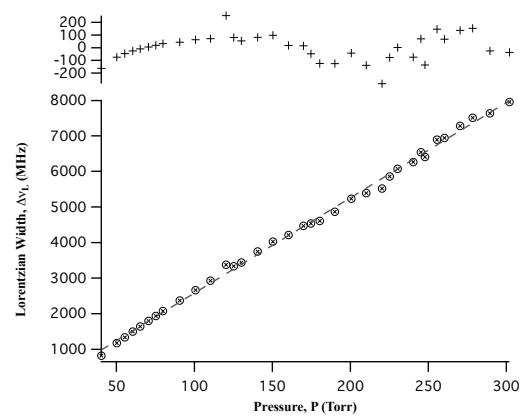
D_2 **Broadening & Shift Data**

(a)

(b)

(c)
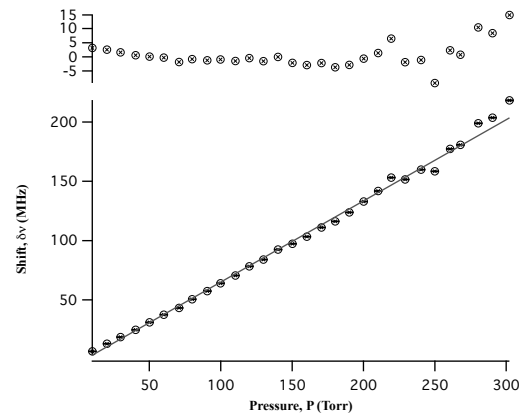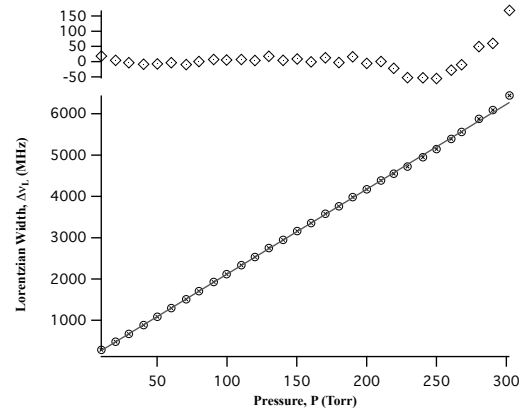
Figure 47. Cesium D_2 transition with increase pressures of He (a) and the resulting widths (b) and shifts (c).
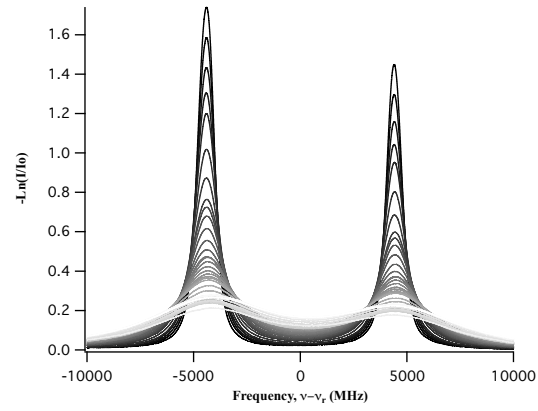
(a)
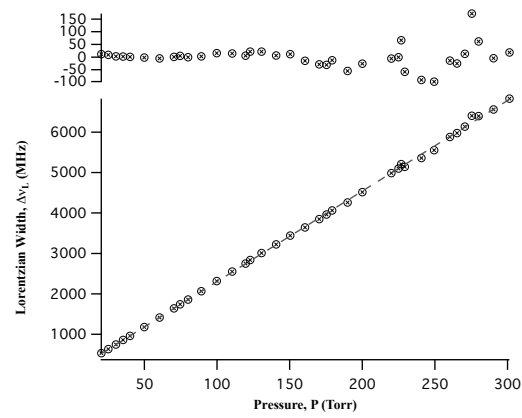
(b)
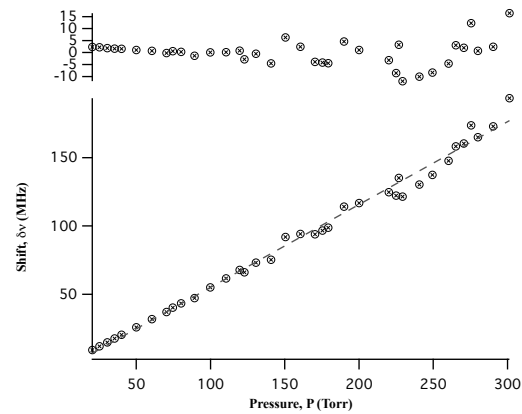
(c)

Figure 48. Cesium D_2 transition with increase pressures of ^{3}He (a) and the resulting widths (b) and shifts (c).
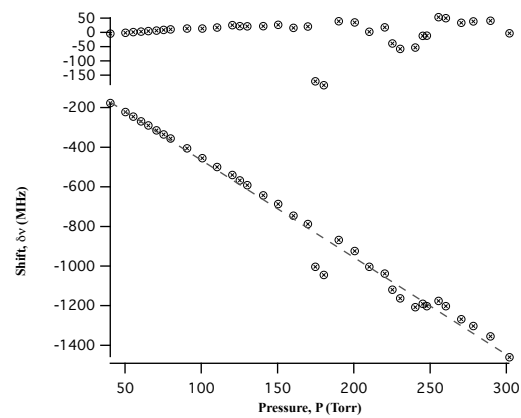
104
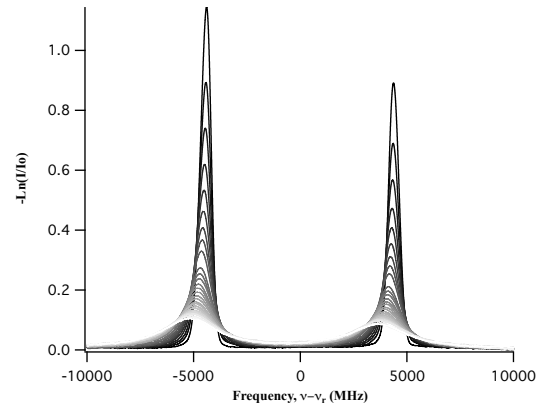
(a)
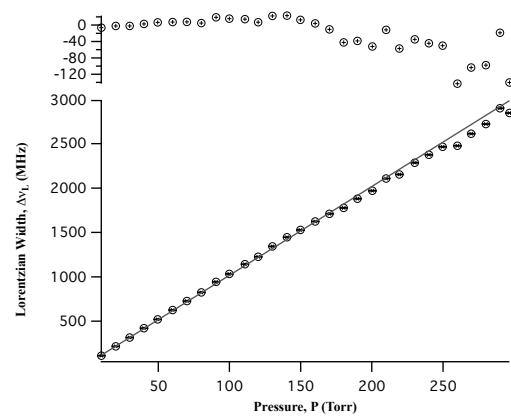
(b)
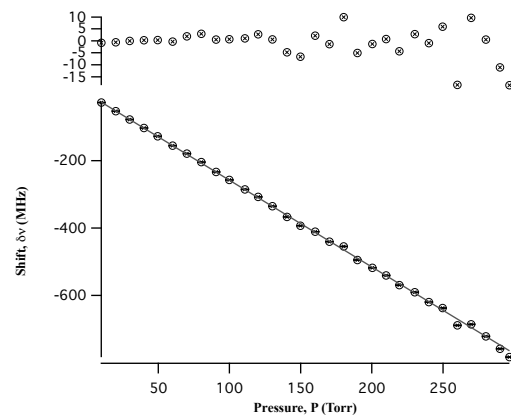
(c)

Figure 49. Cesium D_2 transition with increase pressures of Ne (a) and the resulting widths (b) and shifts (c).
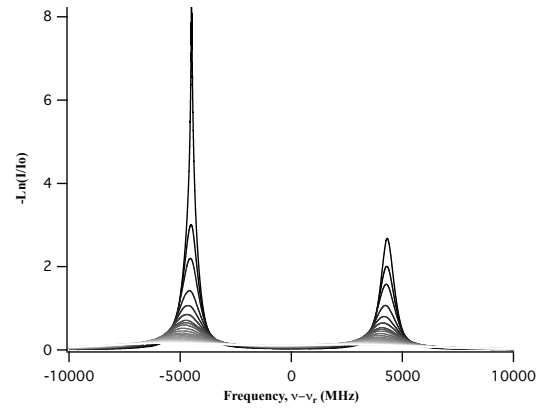
(a)

(b)

(c)

Figure 50. Cesium D_2 transition with increase pressures of Ar (a) and the resulting widths (b) and shifts (c).
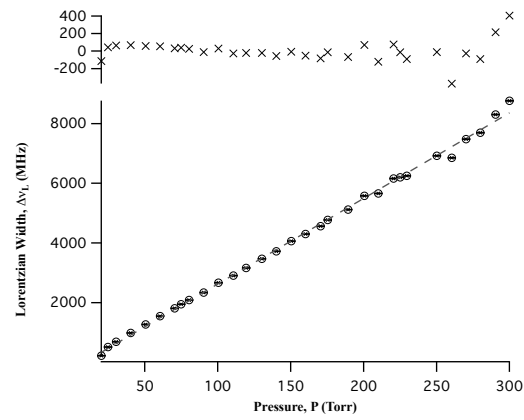
106

(a)

(b)

(c)

Figure 51. Cesium D_2 transition with increase pressures of Kr (a) and the resulting widths (b) and shifts (c).

107

(a)

(b)

(c)

Figure 52. Cesium D_2 transition with increase pressures of Xe (a) and the resulting widths (b) and shifts (c).
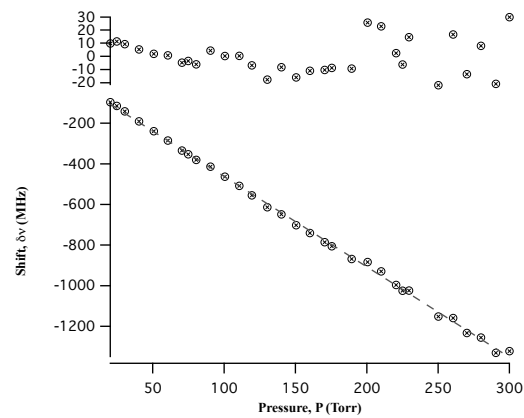
108

(a)

(b)

(c)

Figure 53. Cesium D_2 transition with increase pressures of H_2 (a) and the resulting widths (b) and shifts (c).
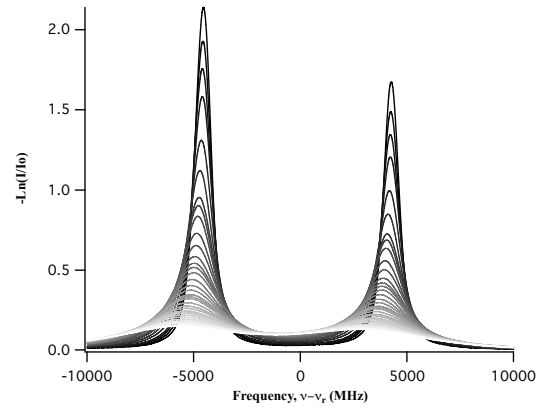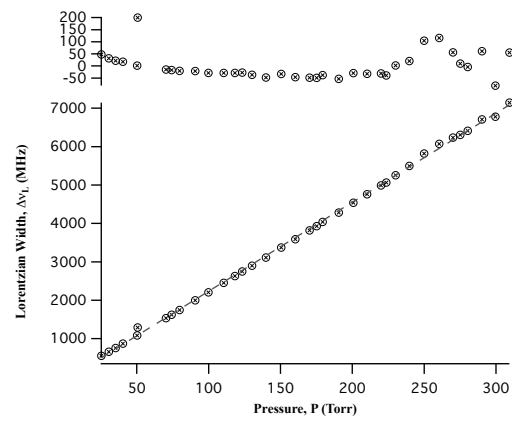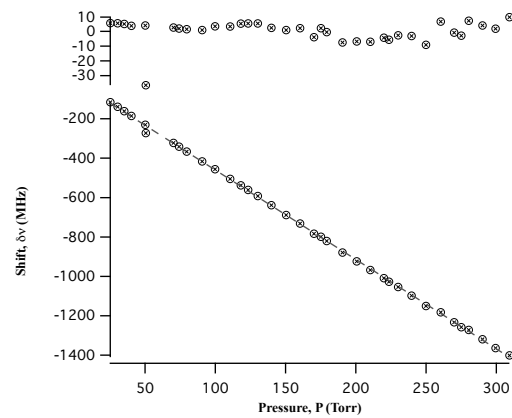
109

(a)

(b)

(c)

Figure 54. Cesium D_2 transition with increase pressures of HD (a) and the resulting widths (b) and shifts (c).

110

(a)

(b)

(c)

Figure 55. Cesium D_2 transition with increase pressures of D_2 (a) and the resulting widths (b) and shifts (c).

111

(a)

(b)

(c)

Figure 56. Cesium D_2 transition with increase pressures of CH_4 (a) and the resulting widths (b) and shifts (c).

112

(a)
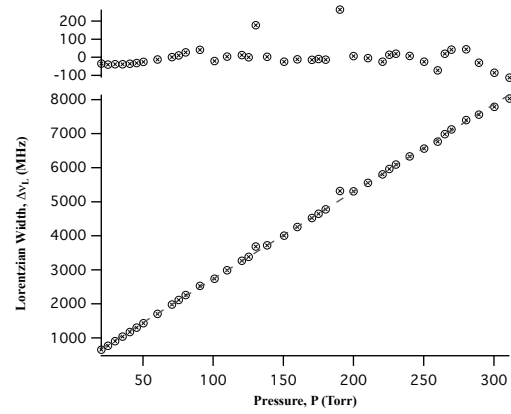
(b)
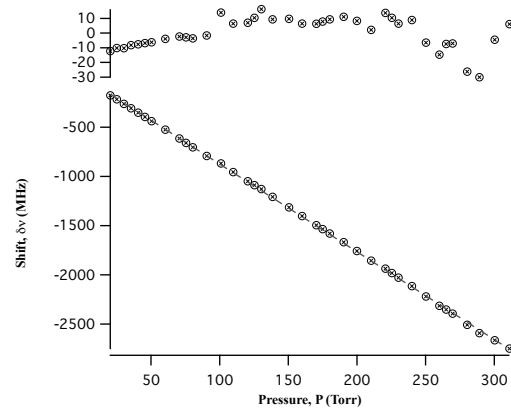
(c)

Figure 57. Cesium D_2 transition with increase pressures of CF_4 (a) and the resulting widths (b) and shifts (c).
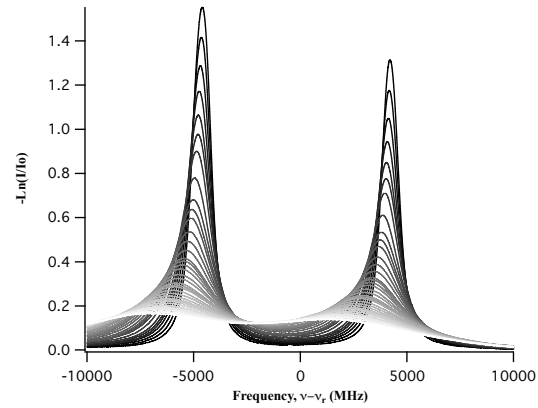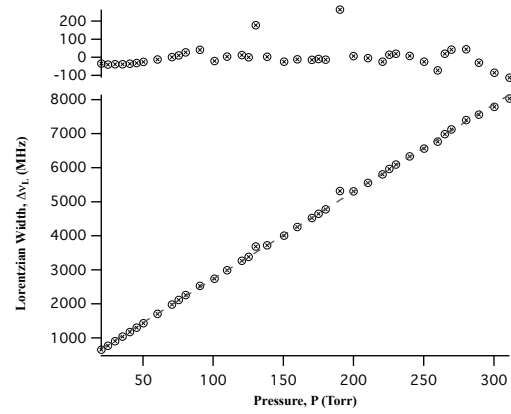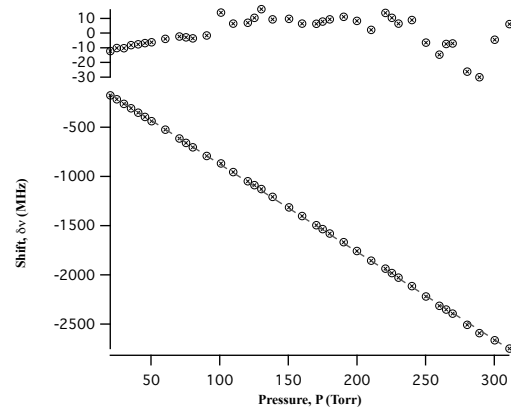
113
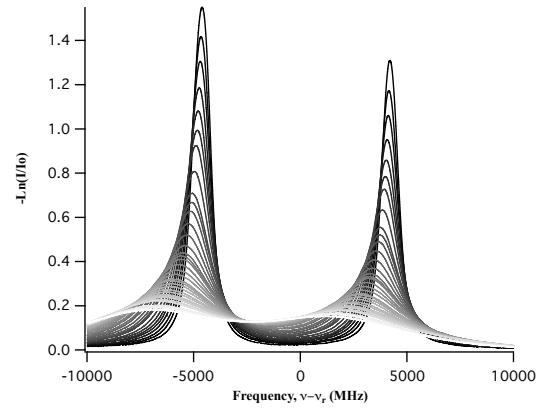
(a)

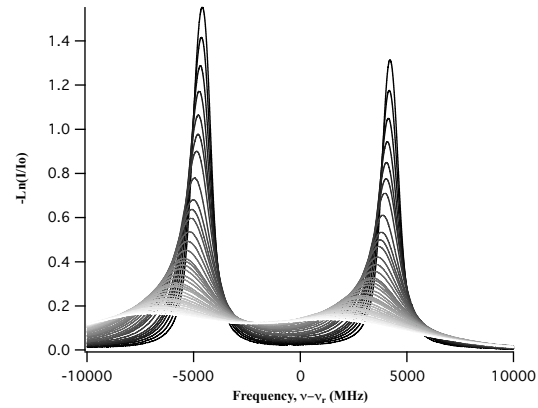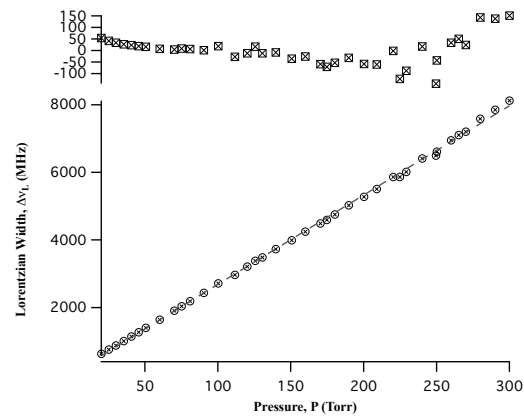
(b)
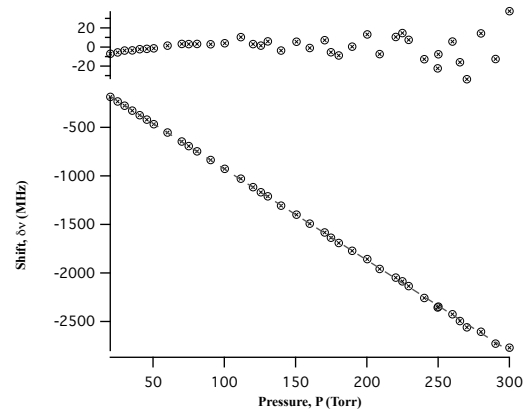
(c)

Figure 58. Cesium D_2 transition with increase pressures of C_2H_6 (a) and the resulting widths (b) and shifts (c).

114

Appendix C. Spin Orbit Data

This appendix contains the rest of the data acquired for the measurement of the spin-orbit rates.
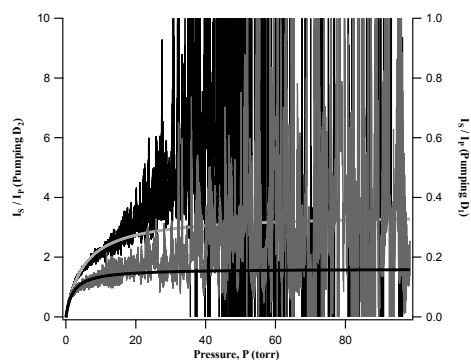
(a)
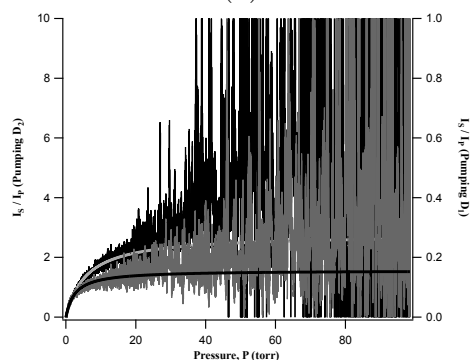
(b)
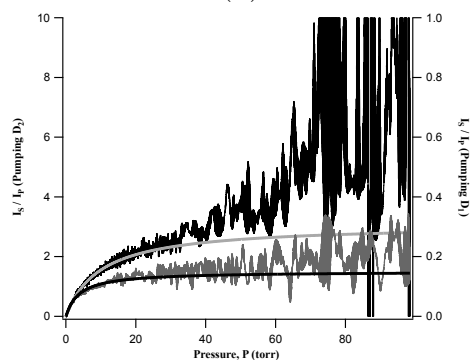
(c)

Figure 59. The ratio of the intensities for satellite to parent states of H$_2$ (a) HD (b) and D$_2$ (c).

Figure 60. The ratio of the intensities for satellite to parent states of CH_4 (a) CF_4 (b) and C_2H_6 (c).
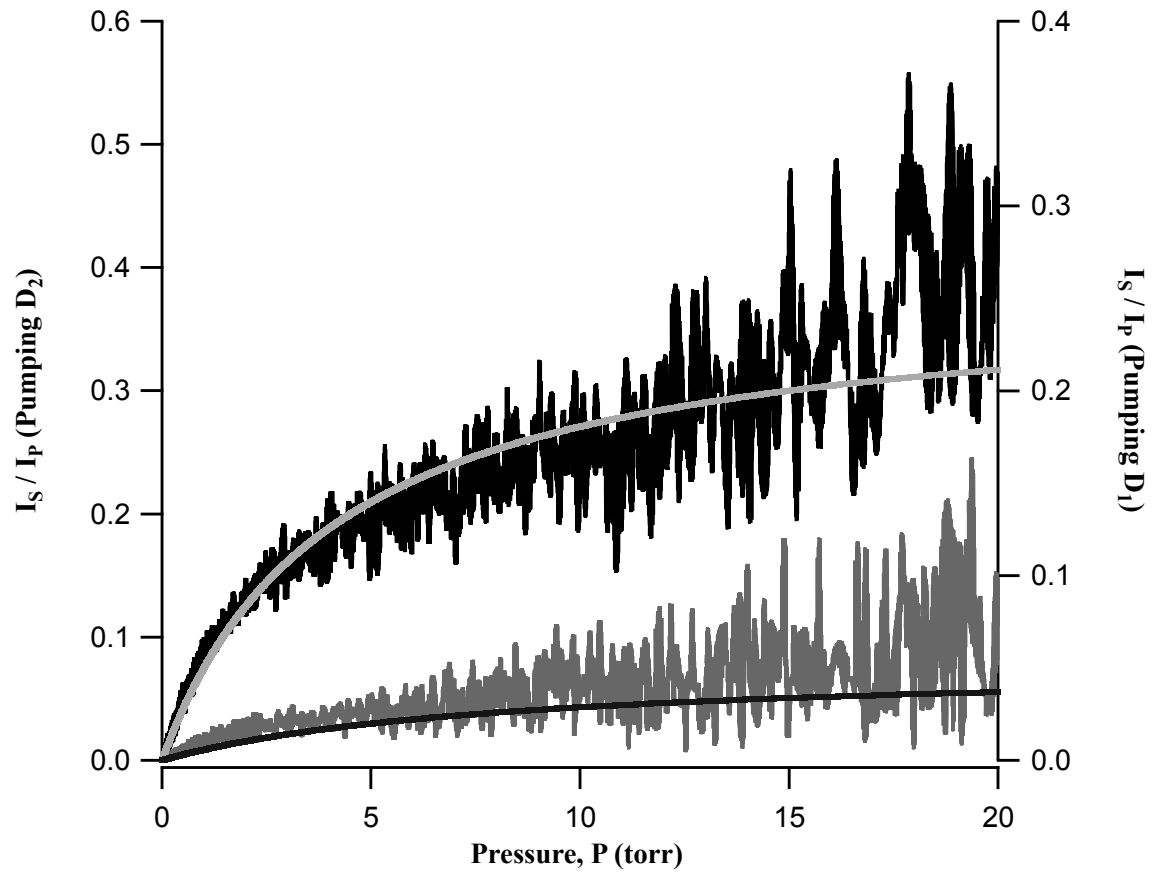
Figure 61. The ratio of the intensities for satellite to parent states of N_2

Bibliography

[1] Akulshin, A.M., R.J. McLean, A.I. Sidorov, and P. Hannaford. "Coherent and Collimated Blue Light Generated by Four-Wave Mixing in Rb Vapour". *Optics Express*, 17(25):22861–22870, November 2009.

[2] Allard, N. and J. Kielkopf. "The Effect of Neutral Nonresonat Collisions on Atomic Spectral Lines". *Rev. Mod. Phys.*, 54:1103, 1982.

[3] Andalkar, Amar. *Spontaneous Spin Polarization and Hysteresis in Cesium Vapor Pumped by Linearly Polarized Light: An Experimental, Theoretical, and Computaitonal Study.* Ph.D. thesis, University of Washington, Box 351560 Seattle, WA 98185-1560, 2001.

[4] Andalkar, Andrew. "High-Resolution Measurement of the Pressure Broadening and Shift of the Cs D1 and D2 Lines by N2 and He Buffer Gases". *Phyiscal Review A*, 65(3), 2002.

[5] Anderson, H. L. *A Physicist's Desk Reference.* American Institute of Physics, New York, NY, 1989.

[6] Arimond, E., M. Inguscio, and P. Violino. *Review of Modern Physics*, 49(31), 1977.

[7] Arimondo, E. and M. Krainska-Miszczak. "Hyperfine constants in the $5^2P_{3/2}$ state of ^{85}Rb". *J. Phys. B*, 8(10):1613, 1975.

[8] Beach, R. J. "End-Pumped Continuous-Wave Alkali Lasers: Experiment, Model, and Power Scaling". *J. Opt. Soc. Am. B*, 21(12):2151–2163, December 2004.
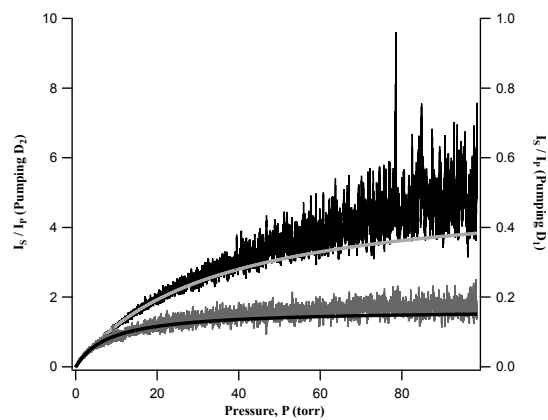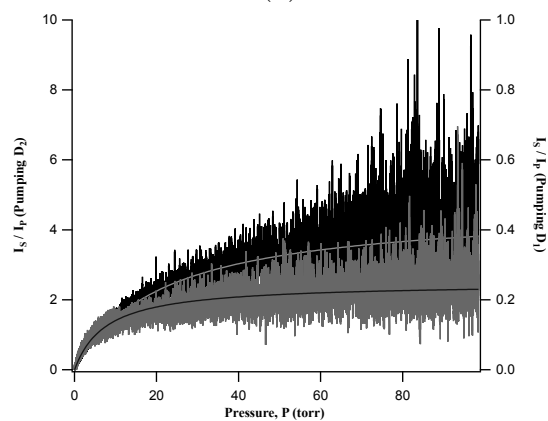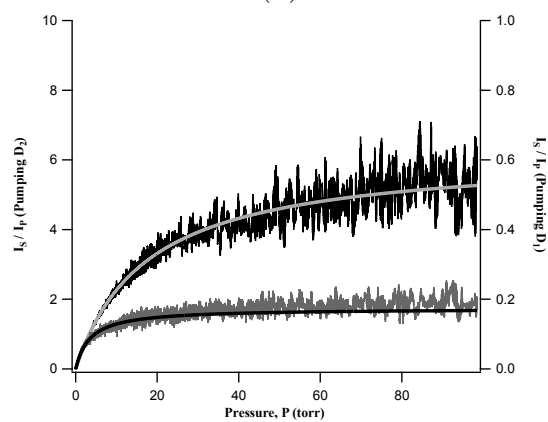
[9] Beach, R.J., W.F. Krupke, V.K. Kanz, and S.A. Payne. "Diode-pumped Alkali Atom Lasers". *UCRL-TR-210223*, 2005.

[10] Beacham, J.R. and K.L. Andrew. *JOSA*, 61:231, 1971.

[11] Bernabeu, E. "Pressure Effects of Helium, Neon, and Argon on the Hyperfine Structure of the First Doublet of Cesium". *J. Opt. Soc. Am.*, 67(1):24, January 1977.

[12] Bernabeu, E. "Shift and Broadening of Hyperfine Components of the First Doublet of Cesium Perturbed by Foreign Gases". *Phyiscal Review A*, 22(6):2690, December 1980.

[13] Blank, L., G. Kedziora, and D. Weeks. "Potential Energy Surfaces for Alkali Plus Noble Gas Pairs: A Systematic Comparison". *Proc SPIE Int Soc Opt Eng*, volume 7581. The International Society for Optical Engineering, February 2010.

[14] Bucka, H., H. Kopfermann, M. Rsaiwall, and H. Schussler. *Z Phys*, 176(45), 1963.

[15] Couture, A. H., T.B. Clegg, and B. Drieguys. "Pressure Shifts and Broadening of the Cs D_1 and D_2 Lines by He, N_1, and Xe at Densities Used for Optical Pumping and Spin Exhange Polarization". *J. Appl. Phys.*, 104, 2008.

[16] Czajkowski, M. "Sensitized Fluorescence in Vapors of Alkali Metals II. Energy Transfer in Cesium-Cesium Collisions". *Canadian Journal of Physics*, 43, July 1965.

[17] Czajkowski, M. "Sensitized Fluorescence in Vapors of Alkali Metals". *Canadian Journal of Physics*, 44, 1966.

[18] Dicke, R. H. "The Effect of Collisions Upon the Doppler Width of Spectral Lines". *Physical Review*, 89(2):472–3, January 1953.

[19] Galatry, Louis. "Simultaneous Effect of Doppler and Foreign Gas Broadening on Spectral Lines". *Physical Review*, 122(4):1218–1223, May 1961.

[20] Gallagher, Alan. "Rubidium and Cesium Excitation Transfer in Nearly Adiabatic Collisions with Inert Gases". *Physical Review*, 172, January 1968.

[21] Garrett, Robert O. "Pressure Effects of Foreign Gases on the Absorption Lines of Cesium. II. The Effects of Helium on the First Two Members of the Principal Series". *Physical Review A*, 144(1), April 1966.

[22] Hamadani, S.M., J. Stockdale, R. Compton, and M. Pindzola. "Two-Photon Resonant Four-Wave Mixing and Multiphoton Ionization of Cesium in a Heat-Pipe Oven". *Physical Review A*, 34(3), 1986.

[23] Hindmarsh, W. R. and J. M. Farr. "Collision Broadening of Spectral Lines by Neutral Atoms". *Prog. Quantum Electron*, 2:141, 1972.

[24] Hirschfelder, J. O., C. F. Curtiss, and R. B. Bird. *Molecular Theory of Gases and Liquids*. Wiley, New York, NY, 1954.

[25] Inoue. "Collision Broadening and Shift of Cesium D2 Resonance Line Perturbed by Every Rare Gas". *J. Phys. Soc. Jpn.*, 59:516–521, 1990.

[26] Izotova, S. L., N. I. Kaliteevskii, and M. S. Frish. *Opt. Spectrosc.*, 59:293, 1985.

[27] Jacobson, H. "Moment Analysis of Atomic Spectral Lines". *Physical Review A*, 4(4):1363, October 1971.

[28] Kielkopf, J. F. "Predicted Alkali Collision Broadening by Noble Gases Based on Semiempirical Potentials". *J. Phys. B*, 9(17):L547–L550, 1976.

119

[29] Kielkopf, J. F. "Measurement of the Width, Shift and Asymmetry of the Sodium D Lines Broadened by Noble Gases". *J. Phys. B - At. Mol. Opt.*, 13:3813–3821, 1980.

[30] Kirchhoff, Gustav and Robert Bunsen. "Chemical Analysis by Observation of Spectra". *Annalen der Physick und der Chemie*, 110:161–189, 1860.

[31] Krause, L. "Collisional Excitation Transfer Between the $^2P_{1/2}$ and the $^2P_{3/2}$ Levels in Alkali Atoms". *Applied Optics*, 5(9):1375–1382, September 1966.

[32] Krupke, W.F., R.J. Beach, V. Kanz, and S.A. Payne. "Resonance Transition 795-nm Rubidium Laser". *Optics Letters*, 28(23):2336–2338, 2003.

[33] Lee, S., S.K. Kim, M. Yun, H.S. Kim, B.H. Cha, and H.J. Moon. "Design and Fabrication of a Diode-Side-Pumped Nd:YAG Laser with a Diffusive Optical Cavity for 500-W Output Power". *Applied Optics*, 41(6):1089, 2002.

[34] Lwin, Nyunt and D G McCartan. "Collision Broadening of the Potassium Resonance Lines by Noble Gases". *Journal of Physics B*, 11(22), 1978.

[35] Malcuit, M.S., D.H. Gauthier, and R.W. Boyd. "Competition Between Four-Wave Mixing and Amplified Spontaneous Emission". *Hyperfine Interactions*, 37:125–140, 1987.

[36] McGillis, D. A. and L. Krause. "Inelastic Collisions Between Excited Alkali Atoms and Molecules I. Sensitized Fluorescence and Quenching Mixtures of Cesium with N_2, H_2, HD, and D_2". *Phys. Rev.*, 153:44, 1967.

[37] McGillis, D. A. and L. Krause. "Inelastic Collisions Between Excited Alkali Atoms and Molecules IV. Sensitized Fluorescence and Quenching Mixtures of Cesium with N_2, H_2, HD, and D_2". *Canadian Journal of Physics*, 46:1051, 1968.

[38] Meijer, T., J.D. White, B. Smeets, M. Jeppesen, and R.E. Scholten. "Blue Five-Level Frequency-Upconversion System in Rubidium". *Optics Letters*, 31(7):1002–1004, April 2006.

[39] Merritt, Jeremy M., Jiande Han, Terry Chang, and Michael C. Heaven. "Theoretical Investigations of Alkali Metal: Rare Gas Interaction Potentials". volume 7196, 71960H. SPIE, 2009.

[40] Miller, W.S., C.V. Sulham, J.C. Holtgrave, and G.P. Perram. "Limitations of an optically pumped rubidium laser imposed by atom recycle rate". *Submitted to Applied Physics B*, May 2010.

[41] Page, R. H., R. J. Beach, V. Keith Kanz, and W. F. Krupke. "Multimode-Diode-Pumped Gas (Alkali-Vapor) Laser". *Optics letters*, 31(3):353–355, February 2006.

[42] Penselin, S., T. Moran, V.W. Cohen, and G. Winkler. *Phyiscal Review*, 127:524, 1962.

[43] Pitz, G. and G. Perram. "Pressure broadening of the D_1 and D_2 Lines in Diode Pumped Alkali Lasers". Claude R. Phipps (editor), *SPIE Proceedings of the 10th International Symposium on Gas Flow and Chemical Lasers*, volume 7005. SPIE, SPIE, May 2008.

[44] Pitz, G.A., C.V. Sulham, E. Acosta, and G.P. Perram. "Two Red photon absorption in alakis producing infrared and blue beams". *41st Plasmadynamics and Lasers Conference*. AIAA, June 2010.

[45] Pitz, Greg A., Charles Fox, and Glen Perram. "Pressure Broadening and Shift of the Cesium D_2 Transition by the Noble Gases and N_2, H_2, HD, D_2, CH_4, C_2H_6, CF_4, and ^{3}He". *Accepted by Physical Review A*, July 2010.

[46] Pitz, Greg A., Doug Wertepny, and Glen Perram. "Pressure Broadening and Shift of the Cesium D_1 Transition by the Noble Gases and N_2, H_2, HD, D_2, CH_4, C_2H_6, CF_4, and ^{3}He". *Physical Review A*, 80(6):062718, December 2009.

[47] Rabinowitz, P. "Continuous Optically Pumped Cs Laser". *Applied Optics*, 1(4):513–516, 1962.

[48] Readle, J.D., C.J. Wagner, J.T. Verdeyen, D.L. Carroll, and J.G. Eden. "Lasing in Alkali atoms pumped by dissociation of alkali-rare gas exciplexes". *High Energy/Average Power Lasers and Intense Beam Applications III*, volume 7196. The International Society for Optical Engineering, 2009.

[49] Ritter, K. J. and T.D. Wilkerson. "High-Resolution of the Oxygen A Band". *J. Mol. Spectrosc.*, 121:1, 1987.

[50] Rotondaro, Matthew D. *Collisional Dynamics of the Rubidium 5^2P Levels*. Ph.D. thesis, AFIT, WPAFB, Ohio, August 1995.

[51] Rotondaro, Matthew D. "Collisional Broadening and Shift of Rubidium D_1 and D_2 Lines by Rare Gases, H_2, D_2, N_2, CH_4 and CF_4". *J. Quant. Spectrosc. Radiat. Transfer*, 57(4):297–507, August 1997.

[52] Rotondaro, Matthew D. "Role of Rotational-Energy Defect in Collisional Tranfser between the $5^2P_{1/2,3/2}$ Levels in Rubidium". *Phyiscal Review A*, 57(5):4045–4048, May 1998.

[53] Rotondaro, Matthew D. "Role of Rotational-Energy Defect in Collisional Tranfser between the $5^2P_{1/2,3/2}$ Levels in Rubidium". *Phyiscal Review A*, 57(5):4045–4048, May 1998.

[54] Sanders, J. H. *Progress in Quantum Electronics*. Pergamon Press, New York, 1973.

[55] Schawlow, A. L. and C. H. Townes. "Infrared and Optical Masers". *Physical Review*, 112(6):1940–1948, December 1958.

[56] Schultz, J.T., S. Abend, D. Doring, J.E. Debs, P.A. Altin, J.D. White, N.P. Robins, and J.D. Close. "Coherent 455nm Beam Production in a Cesium Vapor". *Optics Letters*, 34(15):2321–2323, August 2009.

[57] Schussler, H. A. *Z. Phys*, 182:289, 1965.

[58] Sharma, A., N.D. Bhaskar, Y.Q. Lu, and W. Happer. "Continuous-Wave Mirrorless Lasing in Optically Pumped Atomic Cs and Rb Vapors". *Applied Physics letters*, 39(3):209–211, August 1981.

[59] Siegling, Z. *Z. Naturiorsch Tiel*, 39A:447, 1984.

[60] of Standards & Technology, National Institute. "http://webbook.nist.gov".

[61] Steck, Daniel A. "http://steck.us/alkalidata".

[62] Steinfeld, Jeffrey I., Joseph S. Francisco, and William L. Hase. *Chemical Kinetics and Dynamics*. Prentice Hall, 2nd edition, 1998.

[63] Sulham, C.V. and G.P. Perram. "A Pulsed, Optically-Pumped Rubidium Laser at High Intensity". *Accepted by Optics Communications*, May 2010.

[64] Sulham, C.V., G.A. Pitz, and G.P. Perram. "Blue and Infrared Stimulated Emission from Alkali Vapors through Two-Photon Absorption". *Accepted by Applied Physics B*, December 2009.

[65] Venus, G., A. Gourevitch, V. Smirnov, and L. Glebov. "High Power Volume Bragg Laser Bar with 10 GHz Spectral Bandwidth". *Proc SPIE Int Soc Opt Eng*, volume 6952. The International Society for Optical Engineering, March 2008.

[66] Volz, U. and H. Schmoranzer. "Precision Lifetime Measurements on Alkali Atoms and on Helium by Beam-Gas-Laser Spectroscopy". *Physica Scripta*, T65(48), 1996.

[67] Walentynowicz, E. "Inelastic Collisions between Excited Alkali Atoms and Molecules IX." *Canadian Journal of Physics*, 52:584–588, October 1974.

[68] Walentynowicz, E. "Inelastic Collisions between Excited Alkali Atoms and Molecules X." *Canadian Journal of Physics*, 52:589–591, 1974.

[69] Zhdanov, B.V. "Highly Efficient Optically Pumped Cesium Vapor Laser". *Optics Communications*, 260, November 2006.

[70] Zhdanov, B.V., J. Sell, and R.J. Knize. "Multiple Laser Diode Array Pumped Cs Laser with 48 W Output Power". *Electronic Letters*, 44(9), 2009.

[71] Zhdanov, B.V., A. Stooke, G. Boyadijian, A. Voci, and R.J. Knize. "Rubidium Vapor Laser Pumped by Two Laser Diode Arrays". *Optics Letters*, 33(5):414–415, 2008.

[72] Zibrov, A.S., M.D. Lukin, D.E. Nikonov, L. Holberg, M.O. Scully, V.L. Velichansky, and H.G. Robinson. "Experimental Demonstration of Laser Oscillation without Population Inversion via Quantum Interference in Rb". *Physical Review Letters*, 75(8):1499–1502, August 1995.

[73] Zibrov, A.S., M.D. Lukin, D.E. Nikonov, L. Holberg, M.O. Scully, V.L. Velichansky, and H.G. Robinson. "Efficient Frequency Up-Conversion in Resonant Coherent Media". *Physical Review A*, 65(021801), 2002.

[74] Zweiback, J., G. Hager, and W.F. Krupke. "High Efficiency Hydrocarbon-Free Resonance Transition Potassium Laser". *Optics Communications*, 282:1871–1873, January 2009.

REPORT DOCUMENTATION PAGE

The public reporting burden for this collection of information is estimated to average 1 hour per response, including the time for reviewing instructions, searching existing data sources, gathering and maintaining the data needed, and completing and reviewing the collection of information. Send comments regarding this burden estimate or any other aspect of this collection of information, including suggestions for reducing the burden, to the Department of Defense, Executive Service Directorate (0704-0188). Respondents should be aware that notwithstanding any other provision of law, no person shall be subject to any penalty for failing to comply with a collection of information if it does not display a currently valid OMB control number.
PLEASE DO NOT RETURN YOUR FORM TO THE ABOVE ORGANIZATION.

1. REPORT DATE (DD-MM-YYYY)	2. REPORT TYPE	3. DATES COVERED (From - To)
16-09-2010	Doctoral Dissertation	June 2004-July-2010

4. TITLE AND SUBTITLE
Collisional Dynamics of the Cesium D1 and D2 Transitions

5a. CONTRACT NUMBER

5b. GRANT NUMBER

5c. PROGRAM ELEMENT NUMBER

6. AUTHOR(S)
Pitz, Greg A. AD-21

5d. PROJECT NUMBER

5e. TASK NUMBER

5f. WORK UNIT NUMBER

7. PERFORMING ORGANIZATION NAME(S) AND ADDRESS(ES)
Air Force Institute of Technology, Graduate School of Engineering and management (AFIT/EN), 2950 Hobson Way, WPAFB OH 45433-7765

8. PERFORMING ORGANIZATION REPORT NUMBER

AFIT/DS/ENP/10-S05

9. SPONSORING/MONITORING AGENCY NAME(S) AND ADDRESS(ES)
High Energy Laser Joint Technology Office,
901 University BLVD SE, Suite 100
Albuquerque, New Mexico 87106

10. SPONSOR/MONITOR'S ACRONYM(S)

AFSOR HELJTO

11. SPONSOR/MONITOR'S REPORT NUMBER(S)

12. DISTRIBUTION/AVAILABILITY STATEMENT
Public Release; Distribution Unlimited

13. SUPPLEMENTARY NOTES

14. ABSTRACT

The collisional dynamics of the 62P levels in cesium have been studied utilizing steady state laser absorption and laser induced florescence techniques. In addition the production of a blue beam produced by two photon absorption has been observed in potassium. The collisional broadening rate for cesium, gL, for He, Ne, Ar, Kr, Xe, N2, H2, HD, D2, CH4, C2H6, CF4, and 3He are 24.13, 10.85, 18.31, 17.82, 19.74, 16.64, 20.81, 20.06, 18.04, 29.00, 26.70, 18.84, and 26.00 MHz/torr, respectively for the 62P•1/2 - 62S•1/2 transition and 20.59, 9.81, 16.47, 15.54, 18.41, 19.18, 27.13, 28.24, 22.84, 25.84, 26.14, 17.81, and 22.35 MHz/torr for the 62P•3/2 - 62S•1/2 transition. The corresponding pressure-induced shift rates, d, are 4.24, −1.60, −6.47, −5.46, −6.43, −7.76, 1.11, 0.47, 0.00, −9.28, −8.54, −6.06, and 6.01 MHz/torr for the 62P•1/2 - 62S•1/2 transition and 0.69, -2.58, -6.18, -6.09, -6.75, -6.20, -4.83, -4.49, -4.54, -8.86, -9.38, -6.47, and 0.60 MHz/Torr for the 62P•3/2 - 62S•1/2 transition. These values have been compared with the values of other alkalis and the interatomic difference potentials have been determined using the impact approximation.

15. SUBJECT TERMS

16. SECURITY CLASSIFICATION OF:			17. LIMITATION OF ABSTRACT	18. NUMBER OF PAGES	19a. NAME OF RESPONSIBLE PERSON
a. REPORT	b. ABSTRACT	c. THIS PAGE			Dr. Glen P. Perram
U	U	U	UU	137	19b. TELEPHONE NUMBER (Include area code) 937 255 3636 x4504